The heavy quark mass limit of QCD at non-zero baryon number density

Dissertation

zur Erlangung des Doktorgrades
der Fakultät für Physik
der Universität Bielefeld

vorgelegt von
Olaf Kaczmarek

September 2000

Contents

Introduction **9**

1 Lattice QCD at finite Density **11**

1.1 The QCD phase diagram at vanishing density 11

1.2 The QCD phase diagram at finite density 12

1.3 Chemical potential in lattice QCD 16

1.4 Problems in simulating QCD at finite density 19

1.5 The naive quenched limit 20

1.6 Alternative approaches to finite density 21

1.7 The propagator matrix 23

1.8 The canonical partition function 25

1.9 The grand canonical partition function 28

2 Observables at finite temperature and density **31**

2.1 Thermodynamic observables 31

2.2 The Polyakov loop 32

2.3 Heavy quark potentials 34

2.3.1 Heavy quark potentials in quenched QCD 35

2.3.2 Heavy quark potentials in full QCD 38

2.4 Chiral Condensate 38

3 The quenched limit at non-zero baryon number 43

3.1 Details of the simulation 43

3.2 The sign problem 45

3.3 The deconfinement phase transition 48

3.4 Thermodynamics 53

3.5 Heavy quark potentials at vanishing density 57

3.5.1 Results below T_c 57

3.5.2 Results above T_c 59

3.6 Heavy quark potentials in full QCD 61

3.7 Heavy quark potentials at non-zero density 64

3.7.1 Results below T_c 64

3.7.2 Results above T_c 67

3.8 The chiral condensate 70

4 The quenched limit in the grand canonical approach 73

4.1 Details of the simulation 73

4.2 The sign problem 74

4.3 The confinement-deconfinement phase transition 76

4.4 The critical endpoint 79

4.5 The baryon number density 83

Conclusions 87

A Tables of the results 89

List of Figures

1.1 The phase diagram of QCD for 2+1 quark flavours at vanishing density. . . 12

1.2 Experimental signals for a liquid-gas transition 13

1.3 A simplified phase diagram of QCD in the density-temperature plane. . . . 14

1.4 Conjectured phase diagram for two and three massless flavours 15

1.5 Phase diagram of hadronic and partonic matter. 16

1.6 Comparison of the phase diagram and behaviour of observables in the canonical and grand canonical approaches. 22

3.1 Expectation value of the sign for $N_\tau = 2$ 45

3.2 Expectation value of the sign for $N_\tau = 4$ 46

3.3 Polyakov loop distributions in the canonical approach 47

3.4 Schematic plot of the QCD phase diagram and expected behaviour of the Polyakov loop expectation value along these paths of non-zero B as well as for $B = 0$. 48

3.5 Expectation value of the Polyakov loop for $N_\tau = 2$ 49

3.6 Expectation value of the Polyakov loop for $N_\tau = 4$ 49

3.7 Expectation value of the Polyakov loop susceptibility for $N_\tau = 2$ 51

3.8 Expectation value of the Polyakov loop susceptibility for $N_\tau = 4$ 51

3.9 Expectation value of the susceptibility χ_β for $N_\tau = 2$ 52

3.10 Expectation value of the susceptibility χ_β for $N_\tau = 4$ 52

3.11 Plaquette expectation value P for $N_\tau = 2$ 53

3.12 Plaquette expectation value P for $N_\tau = 4$ 54

3.13 The difference between the zero and finite temperature plaquette expectation values for $N_\tau = 2$. 55

3.14 The free energy density for $N_\tau = 2$. 55

3.15 The difference between the zero and finite temperature plaquette expectation values for $N_\tau = 4$. 56

3.16 The free energy density for $N_\tau = 4$. 56

3.17 The heavy quark potentials for $T < T_c$. 57

3.18 The string tension 58

3.19 The heavy quark potentials for $T > T_c$. 59

3.20 Fit results for the exponent d of the Coulomb-like part of the heavy quark potential above T_c 60

3.21 Screening masses $\mu(T)/T$ for vanishing density. 60

3.22 Heavy quark potentials in lattice unites for staggered fermions and $N_\tau = 4$. 62

3.23 Heavy quark potentials in lattice unites for staggered fermions and $N_\tau = 6$. 63

3.24 Heavy quark potentials in physical units at various temperatures. Compared are quenched and full QCD potentials at the same temperature. . . . 64

3.25 Heavy quark potentials below T_c for vanishing density on $16^3 \times 4$ lattices. . 65

3.26 Heavy quark potentials below T_c for $B = 6$ and different β-values on $16^3 \times 4$ lattices. 65

3.27 Heavy quark potentials below T_c for $\beta = 5.620$ and different densities on $16^3 \times 4$ lattices. 66

3.28 Heavy quark potentials above T_c for vanishing density on $16^3 \times 4$ lattices. . 67

3.29 Heavy quark potentials above T_c for $\beta = 5.720$ and different densities on $16^3 \times 4$ lattices. 68

3.30 Logarithmic plot of the heavy quark potentials above T_c for $\beta = 5.720$ and different densities on $16^3 \times 4$ lattices. 68

3.31 Screening masses $\mu(T)/T$ for different densities. 69

3.32 The chiral condensate for different β-values and various quark masses m_q. . 70

3.33 The $m_q = 0$ extrapolation of the chiral condensate averaged over all three Z(3) sectors. 71

3.34 The $m_q = 0$ extrapolation of the chiral condensate in the real Z(3) sector. . 71

4.1 Polyakov loop distributions in the grand canonical approach. 75

4.2 Expectation value of the sign of $\mathrm{Re}(det(M))$. 76

4.3 Expectation value of the Polyakov loop in the grand canonical approach . . 77

4.6 The pseudo-critical couplings in the grand canonical approach. 77

4.4 Expectation value of the Polyakov loop susceptibility in the grand canonical approach 78

4.5 Expectation value of the plaquette in the grand canonical approach 78

4.7 The fourth Binder cumulant $B_{4,M}$ plotted against the parameter C. 79

4.8 The distribution of E- and M-like observables for different spin models at the critical point. 80

4.9 The joint distributions for E- and M-like observables for different values of C. 81

4.10 The distribution of the M-like observable for different values of C. 82

4.11 The baryon number density in units of the temperature cubed for different values of C. 85

4.12 The baryon number density in units of the temperature cubed for small values of C. 85

Introduction

While the QCD phase diagram for vanishing baryon density is well known from lattice calculations, for the region of non-vanishing density only qualitative features can be understood in terms of models and approximations. The reason for this is the breakdown of the probabilistic interpretation of the path integral representation of the QCD partition function as the fermion determinant becomes complex for non-zero chemical potential. A quantitative analysis of QCD at non-zero density is important for our understanding of the behaviour of dense matter as it is created in heavy ion collisions and exists in the cosmological context. Therefore, analyzing the sign problem and reducing or even solving this problem is an important aim in lattice QCD.
A simple picture of the QCD phase diagram in the temperature-density plane consists of two phases. In the region of small temperatures and small densities quarks und gluons are confined within hadrons forming a hadron gas and chiral symmetry is broken. Increasing the temperature or the density QCD undergoes a phase transition to a phase where quarks and gluons are deconfined forming a quark gluon plasma (QGP) where chiral symmetry is restored. The phase transition between these two phases is well understood for vanishing baryon density from lattice calculations. The order of this transition depends on the number of flavours and the quark masses. For physical quark mass values it is expected to be a cross-over. Additional phases occur at high densities which are relevant for some aspects in cosmology. It is expected that a quark gluon plasma might exist in the cores of neutron stars at high densities and small temperatures. Discussions of the existence of color superconducting phases play a role in this context.
The equations of state, critical parameters of the phase transitions, like critical temperatures and energy densities, and modifications of basic hadronic properties, like masses and decay widths, at non-zero densities are important quantities for the understanding and analysis of experimental signatures of heavy ion collisions. First signatures for the existence of a quark gluon plasma were found at the CERN SPS. In future experiments at RHIC in Brookhaven and LHC at CERN the collision energy of the nuclei will be sufficiently high for the production of such a plasma.
The aim of this work is to get more insight into the physics of QCD at non-zero baryon number density. Because of the sign problem of the fermion determinant and the resulting problems in simulating lattice QCD at finite density, we will have to restrict our analysis to the limit of infinite heavy quarks. Expressions for the heavy quark mass limit for two alternative approaches, namely the canonical and the grand canonical approach, will be derived and the results of simulations in these approaches discussed and compared. We

will see that in this static limit the sign problem is controllable in both approaches for the lattice volumes, temperatures and densities we have analyzed. Thermodynamic observables will be calculated in both approaches and the properties of the deconfinement transition will be analyzed.

Major parts of this work are published in [1, 2, 3] and were presented on various conferences and workshops [4, 5, 6, 7]. It includes the derivation and analysis of the quenched limit at non-zero baryon number density [1], heavy quark potentials in quenched QCD [3] and string breaking in full QCD [2]. These results are put into a more closer context in this work. We will, moreover give a more straightforward derivation of the canonical partition functions discussed in [3] and compare the results obtained in this approach to the grand canonical approach.
A general introduction to lattice gauge theories can, for instance be found in books by Rothe [8] or Montvay and Münster [9]. A rather comprehensive discussion of phase transitions in QCD can be found in an review article by Meyer-Ortmanns [10].

This work is organized as follows:

In chapter 1 our current knowledge of the phase diagram at zero and non-zero densities will be discussed. We will then describe how the chemical potential can be introduced in lattice QCD and discuss the problems arising at non-zero chemical potential. The two alternative approaches to finite density, the canonical and the grand canonical one, will be compared and the connection between both descriptions will be explained in terms of the propagator matrix. We will then derive the partition functions within the canonical and the grand canonical approach in the limit of infinitely heavy, i.e. static, quarks.
In chapter 2 we will discuss the observables at finite temperature and density, which will be used to describe the properties and differences of lattice QCD at zero and non-zero density. The Polyakov loop, although it is no longer an order parameter at non-zero density, will be used to determine the properties of the phase transition. Further important observables that will be discussed are the heavy quark potential and the chiral condensate.
The numerical results obtained within these two approaches will be discussed in chapter 3 and 4. After a description of the simulation details and the sign problem in both approaches, the properties of the phase transition at non-zero densities will be discussed. The heavy quark potentials will be compared for the quenched theory at zero and non-zero density, as well as for the case of full QCD with dynamical quarks.

Chapter 1

Lattice QCD at finite Density

In the first two sections of this chapter we discuss some aspects of our present knowledge of the QCD phase diagram at vanishing density known from lattice QCD and at non-zero density known from phenomenological arguments, approximations and models. We will then introduce the chemical potential in the lattice description and discuss the problems that occur in simulations at non-zero chemical potential, i.e. non-zero baryon number density. After a discussion of the failure of the naive quenched limit, we describe two alternative approaches to finite density, the canonical and the grand canonical one and show the connection between them. As an example we will expand the grand canonical partition function of the staggered fermion formulation in terms of canonical partition functions with the help of the propagator matrix formulation. The quenched, i.e. heavy quark mass limit of lattice QCD will be explained and used to derive the canonical as well as the grand canonical partition functions for Wilson fermions in the limit of static quarks.

1.1 The QCD phase diagram at vanishing density

For zero chemical potential or vanishing baryon density, the structure of the phase diagram is well understood from lattice calculations. The system undergoes a phase transition from a confined phase at low temperatures, where quarks and gluons are bound in hadrons forming a hadronic gas, to a phase of deconfined quarks and gluons in a quark gluon plasma at high temperatures.
In the quenched theory with zero flavours of quarks (the limit of QCD for infinite quark mass), this deconfinement phase transition is of first order [11]. An order parameter for this transition is the Polyakov loop, which is zero (in the infinite volume limit) in the low temperature phase and non-zero in the high temperature phase. The Polyakov loop is connected to the $Z(3)$ center symmetry of the $SU(3)$ gluonic action. This symmetry is related to confinement and thus broken at high temperatures.

In full QCD with dynamical quarks the action is no longer $Z(3)$ symmetric and therefore the Polyakov loop is no longer an order parameter, but serves as an indicator for the deconfinement transition. For decreasing quark masses the deconfinement transition smoothly turns into a chiral phase transition [12]. As long as the explicit breaking of the chiral symmetry by the mass term in the Lagrangian is not too strong, there is a phase transition from a phase of spontaneously broken chiral symmetry to a phase of restored chiral symmetry at high temperatures. The chiral condensate serves as an order parameter for this transition. The order of the transition depends on the number of flavours and on the quark masses. For two flavours of massless quarks, linear σ-models [13] suggest that the transition is of second order, characterized by the critical exponents of the O(4)-model. In the case of three massless flavours, the transition is expected to be of first order, while for physical values of the quark masses, the phase transition might turn into a crossover. This dependence of the order of the phase transitions on the up (u), down (d) and strange (s) quark masses is illustrated in figure 1.1. For QCD with fundamental fermions, the deconfinement and the chiral phase transition coincide, while for QCD with fermions in the adjoint representation the transitions are separated [14].

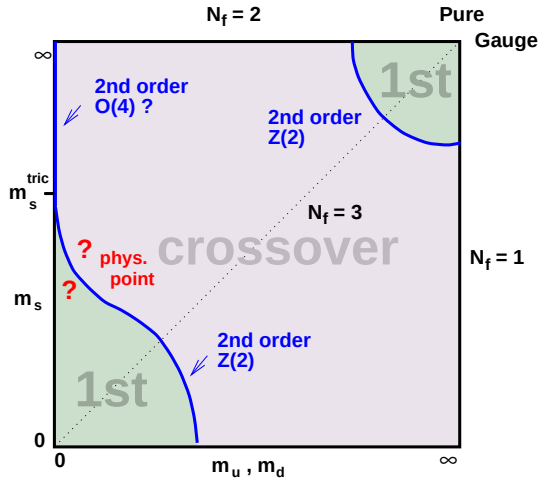

Figure 1.1: *The phase diagram of QCD for 2+1 quark flavours at vanishing density [12].*

1.2 The QCD phase diagram at finite density

A simplified phase diagram of QCD in the density-temperature plane is shown in figure 1.3. In the past years there was some progress in understanding the rich phase structure of QCD at non-zero density in terms of models and approximations. The line of zero temperature and non-zero density can be described by analyzing the ground state of the system. The partition function can be written as a Gibbs sum over all states α of the system,

$$Z = \sum_{\alpha} \exp\left\{-\frac{E_\alpha - \mu N_\alpha}{T}\right\}. \tag{1.1}$$

In the limit of small temperatures, $T \to 0$, the ground state of the system is determined by the minimum of $E_\alpha - \mu N_\alpha$. For $\mu < \mu_0 = \min_\alpha (E_\alpha/N_\alpha)$ the ground state is the vacuum with $N = 0$ and $E = 0$. Therefore the baryon density $n(\mu)$ at zero temperature is zero for $\mu < \mu_0$. The transition to $n(\mu) \neq 0$ is of first order. In [15] the value for μ_0 was estimated to be $m_N - 16$ MeV, the mass of the lightest baryon minus its binding energy, and the density jumps from zero to $n_0 \approx 0.16 fm^{-3}$ at μ_0. At nonzero temperature, the density is

not strictly zero. For small T and μ one finds a dilute gas of light mesons and nucleons with

$$n(T,\mu) \approx \frac{\mu}{T}\left(\frac{2m_N T}{\pi}\right)^{3/2} \mathrm{e}^{-m_N/T}. \tag{1.2}$$

Although the density is no longer zero below the transition for non-zero temperature, it is expected that the transition remains a first order phase transition for sufficiently small T. This nuclear gas-liquid transition line ends at a critical point at $T \sim 10$ MeV. Multi-fragmentation experiments at moderate energies show signals for this transition line [16]. Measurements of the yields of nuclear fragments show that the critical exponents are in agreement with those of the three-dimensional Ising model [17]. In figure 1.2 experimental signals for the gas-liquid transition produced in Au + Au collisions at energies of 600 MeV per nucleon are shown. The plateau in this plot is related to almost constant emission temperatures over a broad range of incident energies. This behaviour suggests a first-order phase transition with a substantial latent heat.

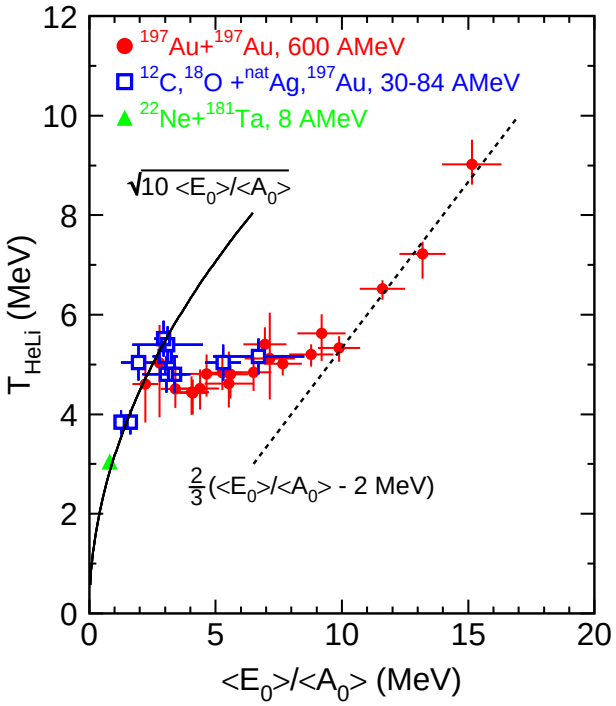

Figure 1.2: *Caloric curve of nuclei determined by the dependence of the isotope temperature T_{HeLi} on the excitation energy per nucleon [16].*

For very high temperatures ($T \gg \Lambda_{QCD}$), quarks and gluons form a plasma. The effective coupling constant $g(T)$ is logarithmically small and therefore one can expect that the chiral condensate is zero and therefore chiral symmetry is restored at high temperatures due to asymptotic freedom. In the opposite region of the phase diagram, for small temperatures and large chemical potential, it is expected that chiral symmetry is also restored. For very large chemical potential ($\mu \gg \Lambda_{QCD}$) the quarks occupy ever higher momentum states and due to asymptotic freedom, the interaction near the Fermi surface is weak. Non perturbative phenomena like chiral symmetry breaking should be absent at sufficiently large μ, therefore one can expect a phase transition where chiral symmetry is restored. This transition is predicted to be of first order from the MIT bag model and random matrix model. The chiral condensate acts as a order parameter for this transition.

At low temperatures, it is expected that additional interesting phases occur above the chiral-symmetry-restoring chemical potential [20]. It was suggested by Bailin and Love [21] that QCD at high density might behave analogous to a superconductor. Through the BCS mechanism [22], Cooper pairs of quarks condense in an attractive channel, breaking the color gauge symmetry, and opening a gap at the Fermi surface. The coherent state, consisting of a quark pair condensate, has lower free energy than the perturbative vacuum,

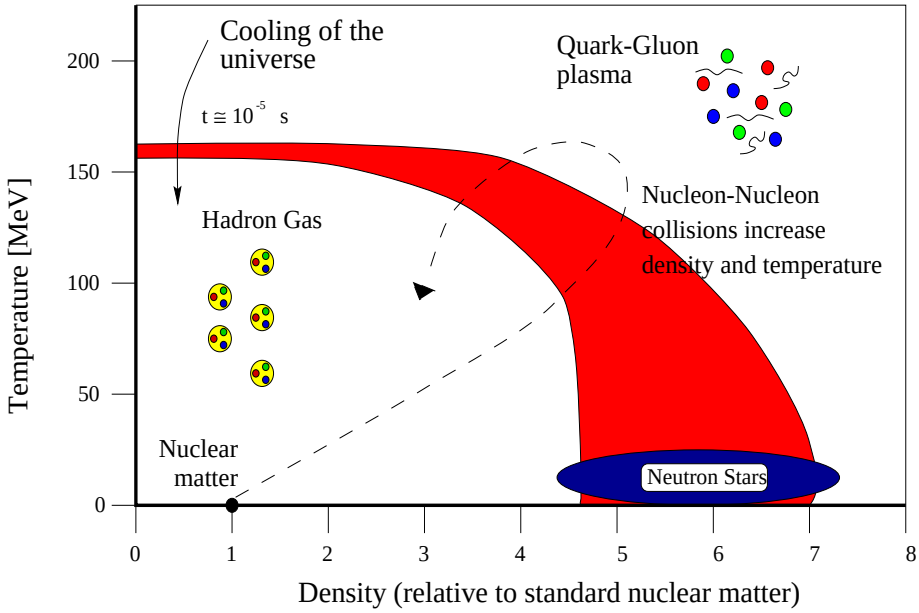

Figure 1.3: A simplified phase diagram of QCD in the density-temperature plane.

indicating that in the true vacuum two quark colors condensate, leaving the third color quarks forming a Fermi surface. Chiral symmetry is caused by a condensate of particle-antiparticle pairs with zero net momentum. In the presence of a Fermi surface with Fermi momentum p_F, one can only create particles with $p > p_F$, so as the density grows, more and more states are excluded from pairing, and chiral symmetry breaking is suppressed. In contrast, color symmetry breaking involves pairs of particles or pairs of anti-particles. Near the Fermi surface these pairs can be created at negligible cost in free energy, and so any attractive particle-particle interaction enables the pairs to lower the free energy. This is the BCS instability of the perturbative vacuum. If there is any channel in which the interaction between quarks is attractive, then quark pair condensation in that channel will occur. As the density increases, the phase space available near the Fermi surface grows, and more quark pairing occurs.

For two massless flavours, mean-field analyses of Nambu-Jona-Lasinio (NJL) models using a 4-leg instanton vertex as the effective interaction [23, 24] indicate that BCS-style quark pair condensation does indeed occur at densities of a few times nuclear matter density. The gaps are of the order of 100 MeV. At even lower temperatures the quarks, left out of the superconducting condensate, may form spin-1 pairs and condensate. There is no local order parameter to distinguish the superconducting phase from the deconfined phase, however, the phase transition is expected to be of first order.

For three massless flavours, an effective interaction with single-gluon exchange [25], shows a similar behaviour as for the two flavour case. The condensate is invariant under correlated color/flavour rotations (*color-flavour locking*). The color symmetry is broken by the quark pair condensate, but unlike in the two flavour case, chiral symmetry is also broken. An illustration of the phase diagram of QCD with two and three massless quark flavours is shown in figure 1.4.

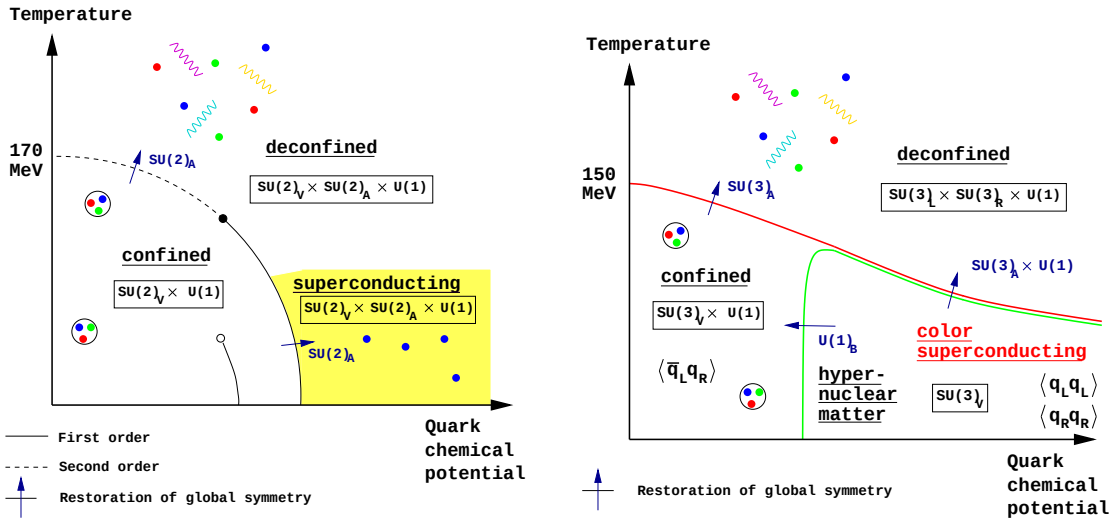

Figure 1.4: *Conjectured phase diagram for two and three massless flavours [18].*

At intermediate temperatures and densities it has been argued that a critical or even tricritical point might exist at the endpoint of the first order transition at large densities [26]. The NJL-model [27] in which the interaction is induced by instantons and the random matrix model [15] have shown almost the same results for the position of the critical point of a temperature of $T_{tc} \sim 100$ MeV and a chemical potential of $\mu_{tc} \sim 600 - 700$ MeV. These are only crude estimates, since they are based on modeling the dynamics of chiral symmetry breaking only. Similar results were obtained in a QCD-like theory by analyzing an effective potential model [28]. A discussion of possible experimental signatures and predictions on the existence of such a (tri)critical point can be found in [29].
The experimental study of the QCD phase diagram is mainly restricted to high temperatures and relatively low densities (see figure 1.5). At low beam energy the target and projectile nuclei will be destroyed and only partially stopped leading to a non-vanishing baryon number density in the collision region. This stopping scenario can be described by the energy loss of a quark propagating through a heavy nucleon, which is of the order of 10 GeV and energy independent. At high beam energies, as will be realized at RHIC and LHC, a transparent scenario leads to a smaller baryon density in the collision region. The target and projectile nucleons interpenetrate and finally leave each other partly undisturbed. The targets deposit a high amount of energy density in form of gluons and quark, anti-quark pairs in the collision region behind. If the energy density is high enough, a quark gluon plasma might be realized in this region. With increasing initial energy density and temperature, the lifetime and the volume of the plasma increase, improving the chances of observing signals directly from the quark gluon plasma. Some recent reviews about possible signals for a transition to a quark gluon plasma are discussed in [30, 31, 32]. An overview of the QCD phase diagram in the region of large densities and the implification of recent developments in our understanding of cold dense quark matter for the physics of compact stars is reviewed in [26, 33, 18] and references in there. The possibility of a critical point in the phase diagram and how heavy ion collision experiments can

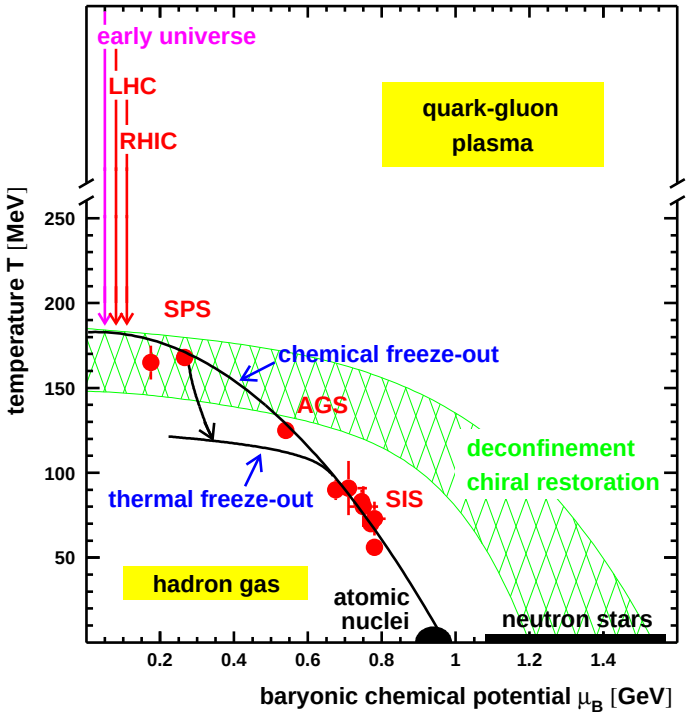

Figure 1.5: *Phase diagram of hadronic and partonic matter. The hadronical freeze out points are determined from thermal model analyses of heavy ion collision data at SIS, AGS and SPS energy. The hatched region indicates the current expectation for the phase boundary. The arrow from chemical to thermal freeze out for the SPS corresponds to isentropic expansion [19].*

discover this point is also discussed there.

1.3 Chemical potential in lattice QCD

The naive way to introduce a chemical potential in lattice QCD is to proceed in analogy with the continuum expression, where the partition function can be written as

$$Z = \mathrm{Tr}\left(e^{-\frac{1}{T}(H-\mu Q)}\right), \tag{1.3}$$

where H is the Hamiltonian and the charge operator Q is given by

$$Q = \int d^3x \bar{\psi}_x \gamma_4 \psi_x. \tag{1.4}$$

The partition function of QCD in the Euclidean path-integral formulation is given by

$$Z = \int \mathcal{D}A_\mu \mathcal{D}\bar{\psi}\mathcal{D}\psi \exp(-S^E_{QCD}). \tag{1.5}$$

The Euclidean action reads

$$S^E_{QCD} = \int_0^{1/T} dt \int_V d^3x \mathcal{L}^E_{QCD}(x) \tag{1.6}$$

with the Euclidean Lagrangian

$$\begin{aligned} \mathcal{L}^E_{QCD} &= \overline{\psi}^f_a \left(\gamma_\mu D_\mu + m_f + \mu\gamma_4\right)^{ab} \psi^f_b + \frac{1}{4} F^a_{\mu\nu} F^{\mu\nu}_a \\ &= \mathcal{L}_F + \mathcal{L}_G. \end{aligned} \tag{1.7}$$

The Euclidean covariant derivative is defined as $D_\mu = \partial_\mu - igA_\mu$.

In the following we will only discuss the fermionic action for free fermions to illustrate how the chemical potenial has to be introduced in the lattice formulation. The partition function then reads

$$Z = \int \prod_x d\psi_x d\bar{\psi}_x e^{-S_F}, \tag{1.8}$$

and the naive discretization of the fermionic action for free fermions with a chemical potential μ is given by

$$S_F = a^3 \sum_x \left(ma\bar{\psi}_x\psi_x + \mu a\bar{\psi}_x\gamma_4\psi_x + \frac{1}{2}\sum_{\mu=1}^{4} \left(\bar{\psi}_x\gamma_\mu\psi_{x+\hat{\mu}} - \bar{\psi}_{x+\hat{\mu}}\gamma_\mu\psi_x\right) \right). \tag{1.9}$$

This approach leads to a quadratic divergence of the energy density for the free theory in the continuum limit. The energy density is defined as

$$\epsilon = -V^{-1} \frac{\partial}{\partial(1/T)} \ln Z \mid_{\mu/T=\text{fixed}} \tag{1.10}$$

where the partition function Z is given by equation (1.8).
In momentum space the integration over the fermion fields in (1.8) can be performed explicitly. In the zero temperature limit the energy density then takes the form

$$\begin{aligned} \epsilon &= a^{-4} \left\{ -\frac{1}{4\pi^4} \int_{-\pi}^{\pi} d^4q \frac{\sum_{j=1}^{3} \sin^2 q_j + (ma)^2}{(\sin q_4 - i\mu a)^2 + \sum_{j=1}^{3} \sin^2 q_j + (ma)^2} \right\} \\ &- a^{-4}\Big\{\mu \equiv 0\Big\}, \end{aligned} \tag{1.11}$$

where the vacuum contributions are subtracted. This expression is quadratically divergent in the continuum limit

$$\epsilon \sim \left(\frac{\mu}{a}\right)^2. \tag{1.12}$$

A similar divergence occurs for the particle number density. This problem is not connected to the occurrence of fermion doublers due to additional zero modes in the free propagator. It also appears in the Wilson formulation for the fermionic action where the 16-fold degeneracy of eq. (1.11) is removed. The divergence is not a lattice artifact, but is also present in the continuum theory itself, where one uses some prescription, like the contour method, to get rid of it. A class of actions that get rid of this divergence in lattice QCD were proposed by Gavai [34]. The most common prescription was introduced by Karsch and Hasenfratz [35]:

$$S_F = a^3 \sum_x \Bigg(ma\bar{\psi}_x\psi_x + \frac{1}{2}\sum_{\mu=1}^{3}\left(\bar{\psi}_x\gamma_\mu\psi_{x+\hat{\mu}} - \bar{\psi}_{x+\hat{\mu}}\gamma_\mu\psi_x\right) + \frac{1}{2}\left(\mathrm{e}^{\mu a}\bar{\psi}_x\gamma_4\psi_{x+\hat{4}} - \mathrm{e}^{-\mu a}\bar{\psi}_{x+\hat{4}}\gamma_4\psi_x\right)\Bigg). \tag{1.13}$$

This expression now leads to the following expression for the energy density in momentum space in the zero temperature limit

$$\epsilon = a^{-4}\left\{-\frac{1}{4\pi^4}\int_{-\pi}^{\pi} d^4q \frac{\sum_{j=1}^{3}\sin^2 q_j + (ma)^2}{\sin^2(q_4 - i\mu a) + \sum_{j=1}^{3}\sin^2 q_j + (ma)^2}\right\} - a^{-4}\Big\{\mu \equiv 0\Big\}. \tag{1.14}$$

$$\tag{1.15}$$

After performing the q_4 integration one gets

$$\epsilon = a^{-4}\frac{1}{2\pi^3}\int_{-\pi}^{\pi} d^3q\,\theta(e^{\mu a} - b - \sqrt{b^2+1})\frac{b}{b^2+1} \tag{1.16}$$

with

$$b^2 = \sum_{j=1}^{3}\sin^2 q_j + (ma)^2. \tag{1.17}$$

In the continuum limit, $a \to 0$, this expression leads to the correct result for the momentum cut-off $\sim \theta(\mu - \sqrt{\vec{q}^2 + m^2})$ in every corner of the Brillouin zone and reproduces 16 times the usual energy density of free fermions at zero temperature,

$$\epsilon = 16\ \epsilon_0 \tag{1.18}$$

$$\epsilon_0 = \frac{\mu^4}{4\pi^2}. \tag{1.19}$$

The particle number density n_q can be derived in the same way and one reproduces 16 times the continuum value,

$$n_q = 16\ n_0 \tag{1.20}$$

$$n_0 = \frac{\mu^3}{3\pi^2}. \tag{1.21}$$

For the Wilson formulation of the fermionic action, the chemical potential can be included analogous to (1.13),

$$\begin{aligned} S_F(\mu a) = \quad & \sum_x (\bar{\psi}_x \psi_x - \kappa \sum_{j=1}^{3} [\bar{\psi}_x (1-\gamma_j) U_{x,j} \psi_{x+\hat{j}} + \bar{\psi}_{x+\hat{j}} (1+\gamma_j) U^\dagger_{x,j} \psi_x] \\ & -\kappa [\mathrm{e}^{\mu a} \bar{\psi}_x (1-\gamma_4) U_{x,4} \psi_{x+\hat{4}} + \mathrm{e}^{-\mu a} \bar{\psi}_{x+\hat{4}} (1+\gamma_4) U^\dagger_{x,4} \psi_x]). \end{aligned} \tag{1.22}$$

The degeneracy is removed for Wilson fermions and the factor 16 in (1.18) and (1.20) disappears.

Together with the gluonic action the grand canonical partition function reads

$$Z_{gc}(T,V,\mu) = \int \mathcal{D}\bar{\psi}\mathcal{D}\psi\mathcal{D}U e^{-S_G(U) - S_F(\bar{\psi},\psi,U)}. \tag{1.23}$$

The standard Wilson discretization of the gluonic action can be written as

$$S_G = \beta \sum_{n,\mu<\nu\leq 4} \left[1 - \frac{1}{2N_c} \mathrm{Tr}\{U_{\mu\nu}(n) + U^\dagger_{\mu\nu}(n)\} \right] \tag{1.24}$$

with the usual definition $\beta = \frac{2N_c}{g^2}$ and the Plaquette terms defined by

$$U_{\mu,\nu} \quad = \quad U_\mu(n) U_\nu(n+a\hat{\mu}) U^\dagger_\mu(n+a\hat{\nu}) U^\dagger_\nu(n). \tag{1.25}$$

For the staggered formulation of the fermionic action, the chemical potential can be introduced in analogy to (1.13) and (1.22).
Considering the way of introducing a chemical potential discussed above at finite temperature, forward quark propagation, in terms of quark loops wrapping around the lattice in the imaginary time direction, is enhanced by a factor $e^{\mu a}$ while forward propagation of anti-quarks is damped by a factor $e^{-\mu a}$. For ordinary closed paths in spatial direction the μ dependence cancels, as these loops describe virtual pair creation and annihilation and the chemical potential for quarks and anti-quarks is of opposite sign. We will see later that this way of including the chemical potential in lattice QCD will lead to a quite natural extension of the calculation scheme for thermodynamic quantities in terms of a hopping parameter expansion for the Wilson formulation of the fermion action at non-zero density.

1.4 Problems in simulating QCD at finite density

The usual approach to include dynamical fermions in lattice QCD is to integrate them out. Due to the Grassmann properties of fermion fields this leads to a determinant of the fermion matrix,

$$\begin{aligned} Z \quad &= \quad \int \mathcal{D}U\mathcal{D}\bar{\psi}\mathcal{D}\psi e^{-S_G(U) - \bar{\psi} M(U) \psi} \\ &= \quad \int \mathcal{D}U \mathrm{det} M(U) e^{-S_G(U)} \end{aligned} \tag{1.26}$$

and an effective action depending only on the gauge fields. Monte Carlo simulations require a positive integrand in the partition function, because of the probabilistic interpretation of the path integral. One way to guarantee this is if M is similar to its adjoint, so the eigenvalues are real or in complex-conjugate pairs,

$$M^\dagger = PMP^{-1} \quad \text{for some } P. \tag{1.27}$$

For the Wilson formulation of the fermion matrix,

$$\begin{aligned} M_{x,y} &= \delta_{x,y} - \kappa \sum_{j=1}^{3} [(r-\gamma_j) U_{x,j} \delta_{x,y-\hat{j}} + (r+\gamma_j) U^\dagger_{x,j} \delta_{x,y+\hat{j}}] \\ &\quad -\kappa [\mathrm{e}^{\mu a}(r-\gamma_4) U_{x,4} \delta_{x,y-\hat{4}} + \mathrm{e}^{-\mu a}(r+\gamma_4) U^\dagger_{x,4} \delta_{x,y+\hat{4}}]) \qquad (1.28) \\ M^\dagger_{x,y} &= \delta_{x,y} - \kappa \sum_{j=1}^{3} [(r+\gamma_j) U^\dagger_{x,j} \delta_{x,y+\hat{j}} + (r-\gamma_j) U_{x,j} \delta_{x,y-\hat{j}}] \\ &\quad -\kappa [\mathrm{e}^{\mu a}(r+\gamma_4) U^\dagger_{x,4} \delta_{x,y+\hat{4}} + \mathrm{e}^{-\mu a}(r-\gamma_4) U_{x,4} \delta_{x,y-\hat{4}}]), \qquad (1.29) \end{aligned}$$

the relation (1.27) is fulfilled for $P = \gamma_5$ and zero chemical potential or purely imaginary chemical potential,

$$M^\dagger = \gamma_5 M \gamma_5 \quad , \quad \text{for } \mu = i\hat{\mu} \text{ with } \hat{\mu} \in \mathcal{R}. \tag{1.30}$$

Introducing a real chemical potential, (1.30) is no longer valid and the fermion determinant is then complex. This is the *sign problem* which is really a phase problem for QCD. For QCD with only two colors, the relation (1.27) is true for $P = \sigma_2$ and any chemical potential and the fermion determinant is real and positive. For any number of colors and fermions in the adjoint representation the fermion determinant is real. All above cases can be classified by a Dyson index, i.e. the number of independent degrees of freedom per matrix element [36].

1.5 The naive quenched limit

Because of the complex fermion determinant, Monte Carlo simulations in QCD with non-zero chemical potential were mainly restricted to the quenched approximation. Problems in this approach were first reported in [37]. In contrast to the expected behaviour, that the onset transition, i.e. the transition from zero to non-zero density, at zero temperature occurs at a critical chemical potential related to the lightest baryon in the theory, $\mu_0 = m_N/3$, where m_N is the nucleon mass, in quenched simulations the onset was found at an unphysical value of half the pion mass, i.e. $\mu_0 = m_\pi/2$. In the chiral limit this would extrapolate to zero and chiral symmetry would be restored for all non-zero μ. This behaviour was also verified in simulations on large lattices [38, 39]. A review of the problems in simulating QCD at non-zero density can be found in [40].

The failure of the quenched approximation at non-zero chemical potential was first understood analytically in terms of chiral random matrix theory [41]. The quenched limit can be interpreted as the limit $N_f \to 0$ of a partition function with the absolute value of the fermion determinant,

$$|\det(\mathcal{D}(\mu)+m)|^{N_f}, \tag{1.31}$$

rather than

$$(\det(\mathcal{D}(\mu)+m))^{N_f}. \tag{1.32}$$

The absolute value of the fermion determinant can be written as

$$\det(\mathcal{D}(\mu)+m)\det(\mathcal{D}^\dagger(\mu)+m). \tag{1.33}$$

Writing the fermion determinant as a Grassmann integral, one observes that the quenched partition function can be interpreted as a partition function of quarks and conjugate anti-quarks. Therefore in addition to the usual Goldstone-modes, the quenched theory contains Goldstone modes consisting of a quark and a conjugate anti-quark [41, 42]. Such modes with the same mass as the usual Goldstone modes, i.e. the pions, have a non-zero baryon number. The critical chemical potential given by the mass of the lightest particle with non-zero baryon number is thus $m_\pi/2$. This explains why the naive quenched limit describes the wrong physics. In the following sections we will derive the correct quenched or in other words static limit in two alternative approaches.

1.6 Alternative approaches to finite density

The baryon number conservation law tells us that the difference between the number of particles and the number of anti-particles, i.e. the baryon number $B = N - \bar{N}$, is conserved. This means that a particle can be created or annihilated only in conjunction with an anti-particle. At low temperatures the thermal energy is not sufficient to create pairs, therefore the number of particles is effectively conserved. At high temperatures the possibility of pair creation has to be taken into account. There will be an average number of particles and anti-particles present in equilibrium and there will also be fluctuations about the average value, while the difference between particle and anti-particle numbers remains strictly constant and is determined by the initial conditions.
In relativistic statistical mechanics, we have the choice between the grand canonical and the canonical treatments of conservation laws. While in the canonical approach the baryon number is conserved exactly, it is the average value of the baryon number which is conserved in the grand canonical description. If the baryon number and the volume take on very large values with $B/V \to const$, the grand canonical approach is adequate, for example in cosmology and astrophysics. In many other realistic physical situations the application of the grand canonical ensemble with respect to the conservation laws can be questionable, especially when dealing with a small amount of matter enclosed in a tiny volume with a small absolute value of the quantum numbers. This situation is found in the

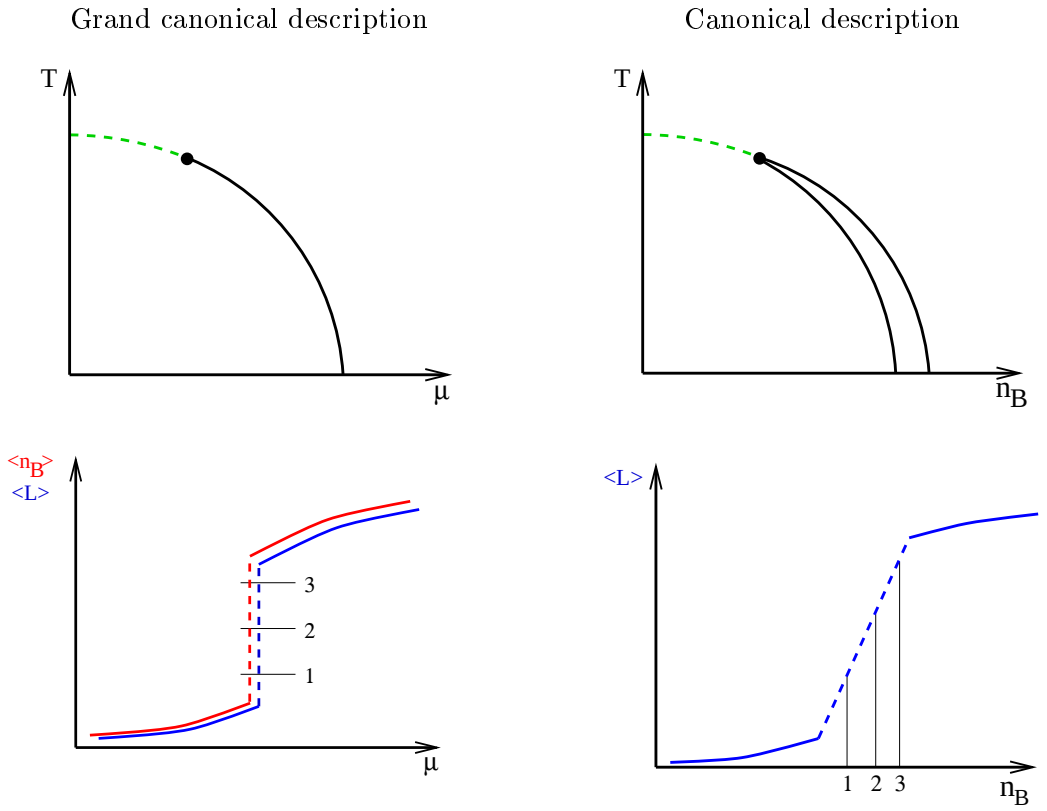

Figure 1.6: *Comparison of the phase diagram and behaviour of observables in the grand canonical (left) and canonical (right) approaches.*

central region of hadron-hadron or heavy-ion collisions, where the baryon number density is of the order of nuclear matter density.
The canonical and the grand canonical ensembles are equivalent in the thermodynamic limit, except at a first order phase transition. The density fluctuations in the grand canonical description are related to an appropriate susceptibility, the isothermal compressibility, in analogy to the specific heat for energy fluctuations. Density fluctuations in the grand canonical description are vanishing small, except in the region of a first order phase transition where the fluctuations become large. This is also expected physically as in such a region the system is composed of two or more phases with different densities. Depending on the amounts of each phase, the number of particles in any given volume can have a whole range of values. In order to get predictions that are in agreement with those obtained by the canonical ensemble, a Maxwell construction is used to continue the grand canonical ensemble. At the critical value of the chemical potential the density can take different values in an interval and the average density shows a discontinuous behavior at the critical chemical potential for a first order phase transition. Due to this behavior at the critical point, the canonical approach seems to be a more appropriate tool to analyze the QCD phase transition at large temperatures and relatively small baryon number densities. The connection between the two alternative approaches to finite density was discussed in detail by Miller and Redlich [43]. The most common one used in lattice QCD is the grand canonical formulation, where density is induced by a chemical potential μ. The grand

canonical partition function $Z_{gc}(T, V, \mu)$ depends on the temperature T, the Volume V and μ. In this formulation, the physical baryon density is an observable, depending on the chemical potential μ, and is conserved in terms of the average value of the baryon number. Monte Carlo simulations in this formulation suffer from the fact that the fermion determinant gets complex for non-zero μ. This *sign problem* was discussed in detail by Barbour et al. [44]. In the static limit, $m_q, \mu \to \infty$, keeping e^{μ}/m_q fixed, as proposed by Bender et al. [45] ,this can be handled for moderate lattice sizes. Simulations in this limit for staggered fermions were performed by Blum et al. [46] and for Wilson fermions in this work (see Chapter 4).
Instead of working with a chemical potential, one can directly fix the quark number density B, i.e. the baryon number density $B/3$, by introducing a complex chemical potential in the grand canonical partition function and performing a Fourier transformation [43]. This transformation projects onto canonical partition functions at fixed quark number B,

$$Z_c(B, T, V) = \frac{1}{2\pi} \int_0^{2\pi} d\phi e^{-iB\phi} Z_{gc}(i\phi, T, V). \tag{1.34}$$

Instead of a complex fermion determinant, the problem of this approach is the heavily oscillating integrand in (1.34). We will see later that this can be handled in the quenched limit, i.e. for infinite quark mass, as the Fourier integral can be performed explicitly after an expansion of the action in terms of the hopping parameter. What remains is a sign problem which can be handled for lattice sizes up to $16^3 \times 4$, small densities and temperatures down to $0.8T_c$.
A qualitative difference of these approaches is described in figure 1.6. In the phase diagram in the T-μ plane, the phase transition occurs at a specific value of the chemical potential, μ_c. For a first order transition, observables like the Polyakov loop L or the baryon number density n_B show a discontinuous behaviour at μ_c. In the canonical approach, n_B is no longer an observable, but a parameter of the theory. It can be written in units of the temperature T cubed as

$$\frac{n_B}{T^3} = \frac{B}{3} \left(\frac{N_\tau}{N_\sigma} \right)^3, \tag{1.35}$$

where B is the number of quarks, i.e. $B/3$ is the baryon number and N_τ and N_σ are the lattice extensions in temporal and spatial direction. By varying the baryon number density one can traverse the region of coexisting phases (the discontinuity in the grand canonical approach at μ_c) continously. Therefore observables are continuous in the density even for a first order phase transition and the transition occurs in a density interval. In the phase diagram in the T-n_B plane an additional region of coexisting phases occurs.

1.7 The propagator matrix

The two alternative approaches to lattice QCD at non-vanishing density, discussed in the previous section, can be compared in a nice way in the following example. For the staggered formulation of the fermionic action, the connection between the canonical and grand

canonical partition functions can be analyzed in terms of a propagator matrix description proposed by Gibbs [47]. The grand canonical partition function can be expanded in terms of canonical partition functions, each for a fixed number of fermions on the lattice. This expansion can be obtained as a characteristic polynomial of a propagator matrix P. Each of the canonical partition functions can be expressed in terms of traces of powers of P.
In the following we derive the propagator matrix formalism for the case of staggered fermions. The fermion matrix M can be redefined as

$$\hat{M} = iM = G + Ve^{\mu} + V^{\dagger}e^{-\mu} + im, \tag{1.36}$$

where the matrix G contains the contribution to $\hat{M}$ from the space-like links and is hermitian, V is the contribution from the forward time-links and m is the bare quark mass. The propagator matrix P can now be defined as

$$P = \begin{pmatrix} -G - im & 1 \\ -1 & 0 \end{pmatrix} V \tag{1.37}$$

and the inverse of P is given by

$$P^{-1} = V^{\dagger} \begin{pmatrix} 0 & -1 \\ 1 & -G - im \end{pmatrix}. \tag{1.38}$$

The matrix P is related to the determinant of the fermion matrix by

$$\det(M) = \det(\hat{M}) = e^{3V\mu}\det(P - e^{-\mu}) \tag{1.39}$$

As the matrix $(P - e^{-\mu})$ is diagonal in the fugacity $e^{-\mu}$, it can be expanded as a characteristic polynomial in the fugacity,

$$\det(P - e^{-\mu}) = e^{-6V\mu}\det(e^{\mu} - P^{-1}) = e^{-6V\mu}\sum_{n=0}^{6V}\hat{\omega}_n e^{n\mu}, \tag{1.40}$$

where the coefficients $\hat{\omega}_n$ are given by the recurrence relation

$$\mathrm{Tr}P^n + \sum_{i=1}^{n-1}\hat{\omega}_i \mathrm{Tr}P^{n-i} + n\hat{\omega}_n = 0 \tag{1.41}$$

with $\hat{\omega}_0 = 1$ and $\hat{\omega}_1 = -\mathrm{Tr}P$. Since the propagator matrix causes a step forward in time, $\mathrm{Tr}P^n$ is non-zero only when n is a multiple of N_τ, the temporal extend of the lattice, and we can define

$$\omega_n = \hat{\omega}_{nN_\tau} \tag{1.42}$$

By considering the hermitian conjugate of (1.39) one can show the following relation:

$$\omega_n = \omega^*_{6V-n}. \tag{1.43}$$

The formal expansion of the grand canonical partition function in terms of the canonical ones is now

$$\begin{aligned} \Omega &= \sum_{n=0}^{3V}\omega_n e^{-(3V-n)N_\tau\mu} + \omega_n^* e^{(3V-n)N_\tau\mu} \\ Z_{gc}(\mu, T, V) &= \int \mathcal{D}U\Omega e^{-S_G} \end{aligned} \tag{1.44}$$

Using the Fourier transformation (1.34) one can see that the canonical partition function for B=$(3V - n)$ fermions on the lattice is given by

$$\begin{aligned} Z_c(B,T,V) &= \frac{1}{2\pi}\int_0^{2\pi} d\phi \mathrm{e}^{-iB\phi} Z_{gc}(i\phi,T,V) \\ &= \int \mathcal{D}U \omega_B e^{-S_G} \end{aligned} \tag{1.45}$$

Due to the $Z(3)$ symmetry, the canonical partition functions are non-zero only when B is a multiple of 3. Furthermore, they are real when integrating over all gauge fields. Equation (1.44) together with the relation (1.43) shows that the fermion determinant is real for $\mu = 0$ and for imaginary chemical potential. While for real and non-zero μ the fermion determinant gets complex.

1.8 The canonical partition function

The connection between the grand canonical and the canonical formulation of QCD was discussed in section 1.6. The main problem arises from the fact that the integrand in the Fourier transformation, which eliminates the dependence on the chemical potential in favour of a fixed quark number, is highly oscillating. We will now derive an explicit expression for the canonical partition functions for Wilson fermions in terms of a hopping parameter expansion as discussed in [1]. The Fourier integral can then be performed explicitly. Later on we will concentrate on the leading order in the hopping parameter κ, which is all one needs to perform the quenched limit ($\kappa \to 0$).
Rewriting the fermionic action (1.22) by transforming the fermion fields

$$\psi'_{(\vec{x},x_4)} = \mathrm{e}^{\mu a x_4}\psi_{(\vec{x},x_4)} \quad , \quad \bar{\psi}'_{(\vec{x},x_4)} = \mathrm{e}^{-\mu a x_4}\bar{\psi}_{(\vec{x},x_4)} \tag{1.46}$$

shifts the dependence on the chemical potential into only the last time slice. The μ-independent part of the action may be written as

$$\tilde{S}_F = S_F(0) - S_F^{N_\tau}(0), \tag{1.47}$$

where $S_F^{N_\tau}$ is the only μ-dependent part of the fermionic action. Using the definition of the temperature $1/T = aN_\tau$ this part can be expressed in terms of $\mu/T = \mu a N_\tau$,

$$S_F^{N_\tau}(\mu/T) = \kappa \sum_{\vec{x}} [\mathrm{e}^{\mu/T}\bar{\psi}_{(\vec{x},N_\tau)}(1-\gamma_4)U_{x,4}\psi_{(\vec{x},1)} + \mathrm{e}^{-\mu/T}\bar{\psi}_{(\vec{x},1)}(1+\gamma_4)U^\dagger_{x,4}\psi_{(\vec{x},N_\tau)}]. \tag{1.48}$$

The chemical potential can now be completely removed from the action by including the μ-dependence in the generalized boundary conditions

$$\psi_{(\vec{x},N_\tau+1)} = -\mathrm{e}^{\mu/T}\psi_{(\vec{x},1)} \quad , \quad \bar{\psi}_{(\vec{x},N_\tau+1)} = -\mathrm{e}^{-\mu/T}\bar{\psi}_{(\vec{x},1)}. \tag{1.49}$$

The grand canonical partition function at a chemical potential $\mu/T = \mu a N_\tau$ in a volume $V = (N_\sigma a)^3$ at temperature $T = 1/N_\tau a$ now reads

$$Z_{gc}(\mu/T,T,V) = \int \prod_{x,\nu} \mathrm{d}U_{x,\nu} \prod_x \mathrm{d}\bar{\psi}_x \mathrm{d}\psi_x \mathrm{e}^{-S_F^{N_\tau}(\mu/T)} \mathrm{e}^{-S_G - \tilde{S}_F}, \tag{1.50}$$

where S_G denotes the gluonic action, which is μ-independent. For the gluonic sector we use the standard Wilson formulation (1.24). The Fourier transformation only acts on the μ-dependent part $\mathrm{e}^{-S_F^{N_\tau}}$, which only involves links pointing in the 4th direction on the last time slice of the lattice. Using the Grassmann properties of the fermionic fields this contribution can be written as

$$\mathrm{e}^{-S_F^{N_\tau}(i\phi)} = \prod_{(\vec{x},a,b,\alpha,\beta,f)} (1-\kappa \mathrm{e}^{i\phi} \bar{\psi}^{a,\alpha,f}_{(\vec{x},N_\tau)} \mathcal{U}^{a,\alpha,b,\beta}_{\vec{x}} \psi^{b,\beta,f}_{(\vec{x},1)}) \times \tag{1.51}$$

$$(1-\kappa \mathrm{e}^{-i\phi} \bar{\psi}^{a,\alpha,f}_{(\vec{x},1)} \mathcal{U}^{\dagger a,\alpha,b,\beta}_{\vec{x}} \psi^{b,\beta,f}_{(\vec{x},N_\tau)}), \tag{1.52}$$

where the product runs over all possible combinations of indices with $\vec{x}$ taking values on the three dimensional (spatial) lattice of size N_σ^3, $\alpha = 1,...,4$ and $a = 1,2,3$ denoting the spinor and color indices and $f = 1,...,n_f$ for different fermion flavours. We have ignored the possibility of having different quark masses, i.e. different hopping parameters κ for various flavours. In the following we will combine the spinor and color indices by $\mathcal{A} = (\alpha, a)$. In (1.52) we have used the notation

$$\mathcal{U}_{\vec{x}} = \Gamma_- U_{(\vec{x},N_\tau),4} \quad , \quad \mathcal{U}^\dagger_{\vec{x}} = \Gamma_+ U^\dagger_{(\vec{x},N_\tau),4} \quad , \text{ with } \Gamma_\pm = (1 \pm \gamma_4) \tag{1.53}$$

Each propagator term in (1.52) comes with a hopping parameter κ and with a complex fugacity $z = \exp(i\phi)$ for the forward propagator, respectively z^* for the backward propagator. Expanding this product in terms of the fugacity results in terms that are proportional to $z^{n-\bar{n}}$ and $\kappa^{n+\bar{n}}$, where n denotes the number of forward and $\bar{n}$ the number of backward propagating terms. The Fourier transformation

$$Z_c(B,T,V) = \frac{1}{2\pi} \int_0^{2\pi} d\phi \ \mathrm{e}^{-iB\phi} Z_{gc}(i\phi,T,V). \tag{1.54}$$

will receive a non-zero contribution only from terms with $n - \bar{n} = B$, i.e. terms that are proportional to z^B. In the following we will only concentrate on the leading order in the hopping parameter κ. As each non-vanishing term in the Fourier transformation is proportional to $\kappa^{n+\bar{n}}$, the leading order in a hopping parameter expansion arises from the $\bar{n} \equiv 0$ sector and can be summarized as

$$z^B f_B \equiv (-z\kappa)^B \sum_{X,C,D,F} \prod_{i=1}^{B} \bar{\psi}^{C_i,f_i}_{(\vec{x}_i,N_\tau)} \mathcal{U}^{C_i,D_i}_{\vec{x}_i} \psi^{D_i,f_i}_{(\vec{x}_i,1)}, \tag{1.55}$$

where X, C, D, F are B-dimensional vectors, i.e. $X = (\vec{x}_1,...,\vec{x}_B)$, $F = (\vec{f}_1,...,\vec{f}_B)$ and so on. All elements of the set $\{(\mathcal{C}_i, f_i, \vec{x}_i)\}_{i=1}^B$ as well as $\{(\mathcal{D}_i, f_i, \vec{x}_i)\}_{i=1}^B$ have to be different to give a non-vanishing contribution to the sum in (1.55). The Fourier integral (1.54) can now be performed explicitly and one obtains the canonical partition function

$$Z(B,T,V) = \int \prod_{x,\nu} \mathcal{D}U_{x,\nu} \prod_x d\hat{\psi}_x \mathrm{d}\psi_x f_B \mathrm{e}^{-S_G - \tilde{S}_F} \tag{1.56}$$

at fixed baryon (or quark) number, where the fixed quark number B is encoded in the function f_B as a sum over products of quark propagators between the time slice $x_4 = 1$ and

$x_4 = N_\tau$. In the following B denotes the quark number. Therefore the physical baryon number is given by $B/3$.
In a hopping parameter expansion (heavy quark mass limit) for the entire fermion determinant, the function f_B is all we need to generate the leading contribution, which finally will be $\mathcal{O}(\kappa^{BN_\tau})$. To this order only B quark loops that wind around the temporal direction of the lattice contribute to the determinant. In the next order in κ additional factors from an expansion of $\exp(-\tilde{S}_F)$ have to be included. In higher orders additional factors of (1.52) which have to contain an equal number of additional backward and forward propagating terms lead to contributions of anti-quarks.
As we want to perform the quenched limit in this approach, we will now have a more detailed look at the leading contribution arising from f_B. To simplify this, we perform a gauge transformation such that all the links pointing in the time direction on the last time slice are equal to unity. As these are the only gauge fields that contributed, f_B now only depends on the fermionic fields on the last time slice,

$$f_B = (-2\kappa)^B \sum_{X,A,F} \prod_{i=1}^{B} \bar{\psi}^{A_i,f_i}_{(\vec{x}_i,N_\tau)} \psi^{A_i,f_i}_{(\vec{x}_i,1)}. \tag{1.57}$$

As only two components of Γ_- are non-zero, the spinor indices α_i which are part of A_i now only take on the values $\alpha_i = 1, 2$. This also gives rise to the factor 2 in front of κ. When evaluating the Grassmann integrals each of the $\bar{\psi}$ terms can be contracted with all those ψ terms which carry the same flavour index. Each pair gives rise to a matrix element of the inverse of $\tilde{Q}$, the fermion matrix corresponding to $\tilde{S}_F$. The different pairings give rise to the Matthews-Salam determinant. We will get the product of n_f determinants, each of dimension d_l such that $\sum_{l=1}^{n_f} = B$,

$$f_B = (2\kappa)^B \sum_{X,A,F} \prod_{l=1}^{n_f} \det \mathcal{M}_l[x, A] \tag{1.58}$$

where the matrix $\mathcal{M}_l$ gives the contributions for the $l-th$ flavour and the matrix elements are the corresponding quark propagators,

$$\mathcal{M}_l^{i,j} = \tilde{Q}^{-1}_{((\vec{x}_j,1),A_j),((\vec{x}_i,N_\tau),A_i)}. \tag{1.59}$$

Each matrix element of $\mathcal{M}_l$ is $\mathcal{O}(\kappa^{(N_\tau - 1 + |\vec{x}_i - \vec{x}_j|)})$. In the heavy quark mass limit ($\kappa \to 0$), only matrix elements with $|\vec{x}_i - \vec{x}_j| = 0$ will contribute. In this case the elements $Q^{-1}_{((\vec{x}_i,1),A_j),((\vec{x}_i,N_\tau),A_i)}$ are just products of terms $\Gamma_- U_{(\vec{x}_i,k),4}$ with $k = 1, ..., N_\tau - 1$. As Γ_- is a diagonal matrix in spinor space the indices α_i and α_j have to be identical. The spinor part thus gives rise to an overall factor $2^{N_\tau - 1}$ for each i, i.e. we obtain B such factors. The multiplication of the $SU(3)$ matrices yields an element of the ordinary, complex valued Polyakov loop ($U \equiv 1$ on the last time slice) which we denote by $L^{a_i,a_j}_{\vec{x}_i}$. Finally, the sum over different color indices appearing in (1.58) leads to contributions involving only traces over powers of the Polyakov loop,

$$L_{\vec{x}} = \prod_{x_4=1}^{N_\tau} U_{(\vec{x},x_4)}. \tag{1.60}$$

As the (color, spinor) label $\mathcal{A}_i$ can take on six different values, the determinant is non-zero only if at most six quarks of a given flavour occupy a given site $\vec{x}_i$. In the quenched limit the partition function now reads

$$Z(B,T,V) = \int \prod_{n,\nu} \mathcal{D}U_\nu(n) f_B \mathrm{e}^{-S_G}. \tag{1.61}$$

A more detailed description of the canonical partition function and a general derivation of the functions f_B can be found in [1]. A more straightforward derivation of the canonical partition functions in the quenched limit will be discussed in the following section in connection to the grand canonical approach.

1.9 The grand canonical partition function

We will now have a look at the grand canonical partition function. We will derive the quenched, i.e. static limit, in this approach analogous to the derivation in [46] and show that the canonical partition functions of the previous section can be derived in a quite natural way analogous to the propagator matrix formalism discussed in section 1.7.
The fermion matrix for Wilson fermions at non-zero chemical potential is given by

$$\begin{aligned} M_{x,y} &= \delta_{x,y} - \kappa \sum_{j=1}^{3} [(1-\gamma_j) U_{x,j} \delta_{x,y-\hat{j}} + (1+\gamma_j) U^\dagger_{x,j} \delta_{x-\hat{j},y}] \\ &\quad -\kappa [\mathrm{e}^{\mu a}(1-\gamma_4) U_{x,4} \delta_{x,y-\hat{4}} + \mathrm{e}^{-\mu a}(1+\gamma_4) U^\dagger_{x,4} \delta_{x-\hat{4},y}]) \\ &= \mathbb{1} - \kappa G - \kappa(1-\gamma_4)\mathrm{e}^{\mu} V - \kappa(1+\gamma_4)\mathrm{e}^{-\mu} V^\dagger \end{aligned} \tag{1.62}$$

In the quenched limit one has to perform the limit $\kappa \to 0$ and $\mu \to \infty$, keeping the ratio $\kappa \mathrm{e}^{\mu}$ fixed [45]. As we have already seen in the canonical approach, only forward propagating terms in temporal direction contribute in this limit,

$$M_{x,y} \approx \mathbb{1} - \kappa(1-\gamma_4)\mathrm{e}^{\mu} V. \tag{1.63}$$

Each spatial point is decoupled from all others and the fermion matrix can be written as

$$M = \begin{pmatrix} 1 & -C^{-1/N_\tau} V_0 & 0 & \dots & 0 \\ 0 & 1 & -C^{-1/N_\tau} V_1 & \dots & \\ 0 & 0 & 1 & & \\ \vdots & \vdots & & \ddots & -C^{-1/N_\tau} V_{N_\tau - 1} \\ C^{-1/N_\tau} V_{N_\tau} & & & & 1 \end{pmatrix} \tag{1.64}$$

with

$$C = (2\kappa \mathrm{e}^{\mu a})^{-N_\tau}. \tag{1.65}$$

The matrices V_i are diagonal in the spatial indices,

$$V_i = Diag\left(\frac{1}{2}(1-\gamma_4) U_4(\vec{x}, x_4 = i), \vec{x}\right). \tag{1.66}$$

The fermion matrix can now be diagonalized and the fermion determinant is expressed as a product of determinants of local Polyakov loops $P_{\vec{x}} = \prod_{x_4} U_4(\vec{x}, x_4)$,

$$\begin{aligned}
\det(M) &= C^{-12V} \prod_{\vec{x}} \det(\Gamma_- P_{\vec{x}} + C) && (1.67)\\
&= C^{-6V} \prod_{\vec{x}} \left(\det(P_{\vec{x}} + C)\right)^2 && (1.68)\\
&= C^{-6V} \prod_{\vec{x}} (C^3 + C^2 \mathrm{Tr} P_{\vec{x}} + C \mathrm{Tr} P_{\vec{x}}^\dagger + 1)^2 && (1.69)\\
&= \prod_{\vec{x}} (C^{-3} + C^{-2} \mathrm{Tr} P_{\vec{x}}^\dagger + C^{-1} \mathrm{Tr} P_{\vec{x}} + 1)^2 && (1.70)\\
&= \prod_{\vec{x}} (\det(P_{\vec{x}}^\dagger + C^{-1}))^2. && (1.71)
\end{aligned}$$

This expression is comparable to the one obtained for the staggered formulation in [46] except for the square of the local determinants. The square enters here due to the spinor structure of the Wilson formulation.
The physical quark density is given by the derivative of the logarithm of the partition function with respect to the chemical potential by

$$\begin{aligned}
\langle n \rangle &= \frac{1}{a N_\tau V} \frac{\partial \ln(Z)}{\partial \mu} && (1.72)\\
&= \frac{2}{V} \left\langle \sum_{\vec{x}} \frac{C^2 \mathrm{Tr} P_{\vec{x}} + 2C \mathrm{Tr} P_{\vec{x}}^\dagger + 3}{C^3 + C^2 \mathrm{Tr} P_{\vec{x}} + C \mathrm{Tr} P_{\vec{x}}^\dagger + 1} \right\rangle . && (1.73)
\end{aligned}$$

One can now define a propagator matrix P by

$$P = \begin{pmatrix} P_0 & 0 & 0 & 0 & 0 \\ 0 & P_0 & 0 & 0 & 0 \\ 0 & 0 & \ddots & 0 & 0 \\ 0 & 0 & 0 & P_{\vec{x}} & 0 \\ 0 & 0 & 0 & 0 & P_{\vec{x}} \end{pmatrix} \qquad (1.74)$$

and the fermion determinant can be expanded as a characteristic polynomial in the coefficient C,

$$\begin{aligned}
\det(M) &= C^{-6V} \det(P + C) && (1.75)\\
&= \det(P^\dagger + C^{-1}) && (1.76)\\
&= \sum_{n=0}^{6V} C^{-n} \omega_n && (1.77)\\
&= C^{-6V} \sum_{n=0}^{6V} C^n \omega_n^* \quad , && (1.78)
\end{aligned}$$

where the ω_n are given by the recurrence relation

$$(-1)^n \mathrm{Tr}P^n + \sum_{i=1}^{n-1}(-1)^{n-i}\omega_i \mathrm{Tr}P^{n-i} + n\omega_n = 0 \tag{1.79}$$

with $\omega_0 = 1$ and $\omega_1 = \mathrm{Tr}P$ and the symmetry $\omega_n = \omega^*_{6V-n}$. The coefficients ω_n can now be interpreted as the canonical partition functions at a fixed quark number $B = n$ and one can show that they are identical to the partition functions derived in the last section. The first coefficients are given by

$$\begin{aligned}
\omega_0 &= 1 && (1.80)\\
\omega_1 &= \mathrm{Tr}P = 2\sum_{\vec{x}} \mathrm{Tr}P_{\vec{x}} && (1.81)\\
\omega_2 &= \frac{1}{2}\left(-\mathrm{Tr}P^2 + (\mathrm{Tr}P)^2\right) = -\sum_{\vec{x}} \mathrm{Tr}P^2_{\vec{x}} + 2\left(\sum_{\vec{x}} \mathrm{Tr}P_{\vec{x}}\right)^2 && (1.82)\\
\omega_3 &= \frac{1}{3}\left(\mathrm{Tr}P^3 - \frac{3}{2}\mathrm{Tr}P^2\mathrm{Tr}P + \frac{1}{2}(\mathrm{Tr}P)^3\right) && (1.83)\\
&= \frac{1}{3}\left(2\sum_{\vec{x}} \mathrm{Tr}P^3_{\vec{x}} - 6\sum_{\vec{x}} \mathrm{Tr}P^2_{\vec{x}} \sum_{\vec{x}} \mathrm{Tr}P_{\vec{x}} + 4\left(\sum_{\vec{x}} \mathrm{Tr}P_{\vec{x}}\right)^3\right) && (1.84)
\end{aligned}$$

The canonical partition functions now read

$$Z(B,T,V) = \int \prod_{n,\nu} \mathcal{D}U_\nu(n)\omega_B \mathrm{e}^{-S_G} \tag{1.85}$$

and are equivalent to the ones derived in the previous section and discussed in [6]. The equivalence, $\omega_B = f_B$, can be seen quite easily by using some calulation rules for the traces of SU(3)-matrices. Because of the Z(3)-symmetry of the action S_G, the partition functions are non-zero only if B is a multiple of 3.
The recurrence relation (1.79) can be rewritten to

$$\begin{aligned}
\omega_n &= -\sum_{i=0}^{n-1}\frac{2}{n}(-1)^{n-i}\omega_i \sum_{\vec{x}} \mathrm{Tr}\ P^{n-i}_{\vec{x}}, \quad \text{with} && (1.86)\\
\omega_0 &= 1
\end{aligned}$$

Therefore the functions $f_B = \omega_B$ can be evaluated for all B and have a more compact form than the expressions derived in [1].

Chapter 2

Observables at finite temperature and density

2.1 Thermodynamic observables

The calculation of the equation of state of QCD is one of the central goals of lattice simulations at finite temperature. The behaviour of thermodynamic observables like the pressure p, the energy density ϵ and the entropy density s are of great interest for the understanding of the QCD phase transition and the high temperature phase as it might have existed in the early universe and be produced in heavy ion collisions. The intuitive picture of the high temperature phase as a gas of weakly interacting quarks and gluons is based on leading order perturbation theory. Perturbative QCD fails to describe the equation of state even at rather high temperatures because of infrared problems of the theory. It seems that non-perturbative effects still dominate the equation of state in the temperature regime attainable in heavy ion collisions.
The high temperature behaviour of QCD is close to that of an ideal gas. Bulk thermodynamic quantities are therefore dominated by contributions from large momenta. These are most strongly influenced by finite cut-off effects. Calculations of the energy density, entropy density and pressure in $SU(3)$ gauge theory with the standard Wilson action were performed by Boyd et al. [48]. They show a strong cut-off dependence which is of $\mathcal{O}((aT)^2)$ and the deviations from the ideal gas limit are about 15% even at temperature of about $5T_c$. In [49] and [50] it was shown that these cut-off effects can be reduced to a few percent by using tree level or tadpole improved actions even on lattices with temporal extent as small as $N_\tau = 4$.
The thermodynamic quantities in lattice QCD can be calculated using basic thermodynamic relations in the continuum. All quantities can be derived from the partition function $Z(T, V, \mu)$. Its logarithm defines the free energy density,

$$f = -\frac{T}{V} \ln Z(T, V, \mu). \tag{2.1}$$

The energy density and pressure are derivatives of $\ln Z$ with respect to T and V,

$$\epsilon = \frac{T^2}{V}\frac{\partial \ln Z(T,V,\mu)}{\partial T}\Big|_{\mu/T \text{ fixed}} \tag{2.2}$$

$$p = T\frac{\partial \ln Z(T,V,\mu)}{\partial V}\Big|_{\mu/T \text{ fixed}} \tag{2.3}$$

As the logarithm of the partition function is not directly accessible within the Monte Carlo approach, the free energy density is calculated from an integration of its derivative with respect to β,

$$-\frac{\partial \ln Z}{\partial \beta} = \langle S_G \rangle = 6N_\sigma^3 N_\tau P_T, \tag{2.4}$$

where S_G is the gluonic part of action and P_T denotes the plaquette expectation value at temperature T calculated on a lattice of size $N_\sigma^3 N_\tau$. If P_0 denotes the plaquette expectation value, evaluated on a lattice of size N_σ^4, the difference of the free energy density at couplings β and β_0 is obtained as

$$\frac{f}{T^4}|_{\beta_0}^{\beta} = -6N_\tau^4 \int_{\beta_0}^{\beta} d\beta' [P_0 - P_T]. \tag{2.5}$$

This relation can also be used to calculate the free energy density at non-zero densities, while the following relations only hold for $\mu = 0$. For large, homogeneous systems the following relation,

$$\ln Z = V\frac{\partial \ln Z}{\partial V} \tag{2.6}$$

can be used to show that the pressure can directly be obtained from the free energy density,

$$p(\beta) = -[f(\beta) - f(\beta_1)], \tag{2.7}$$

with the assumption that β_1 has to be small enough, so that $p(\beta_1)$ is approximately zero. Using the relation (2.7) one can express the entropy density s and the interaction measure Δ in terms of derivatives of the pressure with respect to the temperature,

$$s = \frac{\epsilon + p}{T} = \frac{\partial p}{\partial T} \tag{2.8}$$

$$\Delta = \frac{\epsilon - 3p}{T^4} = T\frac{\partial}{\partial T}\left(p/T^4\right) \tag{2.9}$$

$$= N_\tau^4 T \frac{d\beta}{dT}[S_0 - S_T] \tag{2.10}$$

2.2 The Polyakov loop

Besides the local gauge invariance, the gluonic action S_g and for non-zero density also f_B (if B is a multiple of 3) has a global Z_3 symmetry. The elements of the center of the $SU(3)$

group, $\mathcal{C} = \{z \in SU(3) | zgz^{-1} = g \text{ for all } g \in SU(3)\}$ are given by $\exp(2\pi il/3) \in Z(3)$ with $l = 0, 1, 2$. The action and all local observables are invariant under a transformation $z \in \mathcal{C}$ with

$$U_\tau(\vec{x}, x_4) \to zU_\tau(\vec{x}, x_4), \quad \forall \vec{x}, x_4 \text{ fixed.} \tag{2.11}$$

One observable which is not invariant under this transformation is the Polyakov loop, that consists of a product of link variables along closed curves, which wind around the torus in time direction

$$L_{\vec{x}} = \mathrm{Tr} \prod_{x_4=1}^{N_\tau} U_\tau(\vec{x}, x_4). \tag{2.12}$$

Under the transformation (2.11), the Polyakov loop is rotated by an element of the center,

$$L_{\vec{x}} \to zL_{\vec{x}}. \tag{2.13}$$

The Polyakov loop can be used to define an order parameter for the deconfinement transition in the infinite volume limit at zero density,

$$\langle L \rangle_\infty = \lim_{N_\sigma \to \infty} \langle |L| \rangle_V. \tag{2.14}$$

In the confinement phase ($T < T_c$), configurations that are connected by the center symmetry are equally probable and the expectation value of the Polyakov loop vanishes. In the deconfinement phase ($T > T_c$), the center symmetry is spontaneously broken and $\langle L \rangle_\infty$ gets non-zero. As the $SU(3)$ gauge theory in four dimensions lies in the same universality class as the $Z(3)$ spin model (Potts model) in three dimensions, the phase transition is of first order for the pure gauge theory (vanishing density, $B = 0$). Therefore $\langle L \rangle_\infty$ changes discontinuously at a critical temperature T_c.

The free energy of a single quark is related to the Polyakov loop. The expectation value of Polyakov loops probe the screening properties of a static color triplet test charge in the surrounding gluonic medium. The free energy $F_q(T)$ induced by the presence of this test quark is given by

$$e^{-F_q(T)/T} \sim |\langle L \rangle| = |\langle \frac{1}{L_\sigma^3} \sum_{\vec{x}} L_{\vec{x}} \rangle|. \tag{2.15}$$

In the absence of dynamical or static quarks ($B = 0$) a single quark cannot be screened in the confined phase, therefore $F_q(T)$ is infinite and the expectation value of the Polyakov loop is zero. In fact, a simple quark does not exist as a physical state in the spectrum even for $T > T_c$. The above notion is therefore only a commonly used notation for the behaviour of a physical system consisting of a quark antiquark pair which gets separated to infinite distance.
The Polyakov loop thus reflects the large distance behaviour of the potential or access free energy between a heavy quark and a heavy anti-quark. For non-zero temperature, the heavy quark potential can be calculated using Polyakov loop correlations [3],

$$e^{-\frac{V(\vec{x}-\vec{y},T)}{T}} = \langle \mathrm{Tr} L_{\vec{x}} \mathrm{Tr} L_{\vec{y}}^\dagger \rangle \underset{|\vec{x}-\vec{y}| \to \infty}{\longrightarrow} |\langle L \rangle|^2. \tag{2.16}$$

As $\langle L \rangle$ is zero in the low temperature phase for vanishing density, the heavy quark potential is infinite (confined) for infinite separation of the quark anti-quark pair. The potential in the confined phase can be parameterised by

$$V(R,T) = V_0 + \alpha(T)/R + \sigma(T)R, \tag{2.17}$$

where $\sigma(T)$ is the temperature dependent string tension.
In QCD with dynamical light quarks the Polyakov loop is no longer an order parameter. The heavy quark potential stays finite at large distances even in the confined phase because the static quark anti-quark pair can be screened through the creation of a light quark anti-quark pair from the vacuum (*string breaking*).
At non-zero baryon number density we expect to find a similar behaviour of the heavy quark potential even in the heavy quark mass limit because the quarks needed to break the string need not be created through thermal (or vacuum) fluctuations. The static quark anti-quark sources used to probe the heavy quark potential can recombine with the already present static quarks to a baryon and a meson and will lead to a screening of the potential even in the low temperature hadronic phase. Therefore the Polyakov loop expectation value no longer serves as an order parameter at non-zero baryon density, although the integrand of the partition function, $f_B \exp(-S_G)$, is $Z(3)$ symmetric, therefore we expect that

$$\langle L \rangle \; > \; 0 \; , \text{ for all } n_B > 0 \text{ and all } \beta \geq 0. \tag{2.18}$$

At temperatures above the critical temperature T_c the Polyakov loop $\langle L \rangle$ is non-zero, due to the spontaneous breaking of the $Z(3)$ symmetry, and the heavy quark potential stays finite for infinite separation. For temperatures just above T_c perturbative arguments, that suggest a Debye-screened Coulomb potential for large temperatures, will not apply and a more general ansatz [51],

$$\frac{V(R,T)}{T} = -\frac{e(T)}{(RT)^d} e^{-\mu(T)R} \tag{2.19}$$

with an arbitrary power d, an arbitrary coefficient $e(T)$ and a simple exponential decay determined by a general screening mass $\mu(T)$ can be used.
A more detailed description of the heavy quark potential, including corrections to (2.17) can be found in [3]. Some aspects will be discussed in the following sections.

2.3 Heavy quark potentials

The understanding of the heavy quark potential, i.e. the potential between a heavy quark anti-quark pair, is important for the understanding of confinement and deconfinement. Heavy quark potentials can be used as input for spectroscopy and dissociation of quarkonia, i.e. mesonic states that contain two heavy constituent quarks, either charm or bottom (due to the large weak decay rate $t \to bW^+$, the top quark does not appear as a constituent

in bound states). Examples for such mesons are J/Ψ ($c\bar{c}$) or Υ ($b\bar{b}$).
For sufficiently heavy quarks one might hope that the characteristic time scale associated with the relative movement of the constituent quarks is much larger than that associated with the gluonic or sea quark degrees of freedom. In this case the adiabatic (or Born Oppenheimer) approximation applies and the effect of gluons and sea quarks can be represented by an averaged instantaneous interaction potential between the heavy quark sources. The bound state problem will essentially become non-relativistic and the dynamics will, to first approximation, be controlled by the Schrödinger equation,

$$\left[-\frac{\hbar^2}{2m}\Delta_{\vec{x}} + V(R)\right] \Psi_{nll_3}(\vec{R}) = E_{nl}\,\Psi_{nll_3}(\vec{R}), \tag{2.20}$$

with a potential $V(R)$. One Ansatz for the the heavy quark potential $V(R)$ is the Cornell potential [52],

$$V(R) = -\frac{e}{R} + \sigma R. \tag{2.21}$$

Extracting the string tension from fitting the exponentially measured quarkonia spectra to the Cornell potential results in values of $\sqrt{\sigma} \approx 412$ MeV [53] and $\sqrt{\sigma} \approx 427$ MeV [54]. This result is in qualitative agreement with the value $\sqrt{\sigma} \approx 429(2)$ MeV extracted in [55].
Quarkonium dissociation is one of the important signals for the production of quark gluon plasma in heavy ion collisions. Its usefulness as deconfinement probe is easily seen. If for example a J/Ψ is placed into a hot medium of deconfined quarks and gluons, color screening will dissolve the binding, so that the c and $\bar{c}$ quarks separate. When the medium cools down to the deconfinement transition point, they will therefore in general be too far apart to see each other. Since thermal production of further $c\bar{c}$ pairs is negligibly small because of the high charm quark mass, the c must combine with a light anti-quark to form a D, and the $\bar{c}$ with a light quark for a $\bar{D}$. The presence of a quark-gluon plasma will thus lead to a suppression of J/Ψ production. This dissociation of the quarkonia can again be understood with the help of heavy quark potentials, which in the deconfined region show, to first approximation, a Coulomb behaviour which is screened with a screening mass $\mu(T)$. The temperature dependence of the screening mass or in general of the heavy quark potential can be used to describe the melting pattern, i.e. the different dissociation temperatures, for different quarkonia states. With increasing temperature, a hot medium will thus lead to a successive quarkonium melting, so that the suppression or survival of specific quarkonium states serves as a thermometer for the medium. A detailed description of the quarkonium dissociation and other signals for deconfinement can be found in [31].
In the following sections we will describe our present knowledge of the heavy quark potential in the different phases of QCD for the quenched, as well as the full QCD theory, at vanishing densities.

2.3.1 Heavy quark potentials in quenched QCD

The potential between a heavy quark anti-quark pair at finite temperatures is computed from Polyakov loop correlations

$$\langle L(\vec{0})L(\vec{R})^\dagger\rangle = \exp\{-V(|\vec{R}|,T)/T\} \tag{2.22}$$

where

$$L(\vec{x}) = \frac{1}{3}\mathrm{tr} \prod_{\tau=1}^{N_\tau} U_4(\vec{x},\tau) \tag{2.23}$$

denotes the Polyakov loop at spatial coordinates $\vec{x}$. In the limit $R \to \infty$ the correlation function should approach the cluster value $|\langle L(0)\rangle|^2$ which vanishes if the potential is rising to infinity at large distance (confinement) and which acquires a finite value in the deconfinement phase.
In the limit where the flux tube between two static quarks can be considered as a string, predictions about the behaviour of the potential are available from computations of the leading terms arising in string models. For zero temperature one expects at large distance

$$V(R) = V_0 - \frac{\pi}{12}\frac{1}{R} + \sigma R \tag{2.24}$$

where V_0 denotes the self energy of the quark lines, σ is the string tension and the Coulomb-like $1/R$ term stems from fluctuations of the string [56]. Eq. (2.24) generally gives a good description of the zero temperature ground-state potential although it has been shown [57] that the excitation spectrum meets string model predictions only at large quark pair separations.
For non-vanishing temperatures below the critical temperature of the transition to deconfinement, a temperature dependent potential has been computed [58] as

$$\begin{aligned} V(R,T) &= V_0 - \left[\frac{\pi}{12} - \frac{1}{6}\arctan(2RT)\right]\frac{1}{R} \\ &\quad + \left[\sigma - \frac{\pi}{3}T^2 + \frac{2}{3}T^2 \arctan\left(\frac{1}{2RT}\right)\right] R + \frac{T}{2}\ln(1+(2RT)^2). \end{aligned} \tag{2.25}$$

In the limit $R \gg 1/T$ this goes over into

$$\begin{aligned} V(R,T) &= V_0 + \sigma(T)R + T\ln(2RT) && (2.26)\\ &= V_0 + \left[\sigma - \frac{\pi}{3}T^2\right] R + T\ln(2RT), && (2.27) \end{aligned}$$

which had been calculated previously [59]. Note the logarithmic term which originates from transverse fluctuations of the string. The temperature dependent terms appearing in (2.25) and (2.27) should be considered as thermal corrections to the zero temperature string tension. An explicitly temperature dependent string tension was computed by means of a $1/D$ expansion [60],

$$\frac{\sigma(T)}{\sigma(0)} = \sqrt{1 - \frac{T^2}{T_c^2}}, \tag{2.28}$$

where T_c was obtained as

$$T_c^2 = \frac{3}{\pi(D-2)}\sigma(0). \tag{2.29}$$

Note, however, that for $D \to \infty$ the phase transition is of second order, leading to a continuous vanishing of the string tension at the deconfinement temperature. In color $SU(2)$,

which also exhibits a second order transition, it was established [61] that $\sigma(T)$ vanishes $\sim (\beta_c - \beta)^\nu$ with a critical exponent ν taking its 3-D Ising value of 0.63 as suggested by universality. In the present case of $SU(3)$ one expects a discontinuous behaviour and a non-vanishing string tension at the critical temperature.
In the deconfined phase the Polyakov loop acquires a non-zero value. Thus, we can normalize the correlation function to the cluster value $|\langle L\rangle|^2$, thereby removing the quark-line self energy contributions,

$$\frac{\langle L(\vec{0})L(\vec{R})^\dagger\rangle}{|\langle L\rangle|^2} = \exp\{-V(|\vec{R}|,T)/T\}. \tag{2.30}$$

Moreover, the quark-antiquark pair can be in either a color singlet or a color octet state. Since in the plasma phase quarks are deconfined the octet contribution does not vanish, although it is small compared to the singlet part, and the Polyakov loop correlation is a color averaged mixture of both

$$e^{-V(R,T)/T} = \frac{1}{9}e^{-V_1(R,T)/T} + \frac{8}{9}e^{-V_8(R,T)/T}. \tag{2.31}$$

At high temperatures, perturbation theory predicts [62] that V_1 and V_8 are related as

$$V_1 = -8V_8 + \mathcal{O}(g^4). \tag{2.32}$$

Correspondingly, the color-averaged potential is given by

$$\frac{V(R,T)}{T} = -\frac{1}{16}\frac{V_1^2(R,T)}{T^2}. \tag{2.33}$$

Due to the interaction with the heat bath the gluon acquires a chromo-electric mass $m_e(T)$ as the IR limit of the vacuum polarisation tensor. To lowest order in perturbation theory, this is obtained as

$$\left(\frac{m_e^{(0)}(T)}{T}\right)^2 = g^2(T)\left(\frac{N_c}{3} + \frac{N_F}{6}\right), \tag{2.34}$$

where $g(T)$ denotes the temperature-dependent renormalised coupling, N_c is the number of colors and N_F the number of quark flavours. The electric mass is also known in next-to-leading order [63, 64] in which it depends on an anticipated chromo-magnetic gluon mass although the magnetic gluon mass itself cannot be calculated perturbatively. Fourier transformation of the gluon propagator leads to the Debye-screened Coulomb potential for the singlet channel

$$V_1(R,T) = -\frac{\alpha(T)}{R}e^{-m_e(T)R}, \tag{2.35}$$

where $\alpha(T) = g^2(T)(N_c^2-1)/(8\pi N_c)$ is the renormalised T-dependent fine structure constant. It has been stressed [65] that eq. (2.35) holds only in the IR limit $R \to \infty$ because momentum dependent contributions to the vacuum polarisation tensor have been neglected. Moreover, at temperatures just above T_c perturbative arguments will not apply

so that we have chosen to attempt a parametrisation of the numerical data with the more general ansatz [51]

$$\frac{V(R,T)}{T} = -\frac{e(T)}{(RT)^d} e^{-\mu(T)R}, \tag{2.36}$$

with an arbitrary power d of the $1/R$ term, an arbitrary coefficient $e(T)$ and a simple exponential decay determined by a general screening mass $\mu(T)$. Only for $T \gg T_c$ and large distances we expect that $d \to 2$ and $\mu(T) \to 2m_e(T)$, corresponding to two-gluon exchange.

2.3.2 Heavy quark potentials in full QCD

In lattice QCD with dynamical quarks two physical effects can be expected concerning the heavy quark potential, one at large distance and one at small distance. Within the quenched approximation the number of quarks and anti-quarks are separately conserved. In full QCD, i.e. with sea quarks, only the difference (the baryon number) is a conserved quantity. Light quark anti-quark pairs can be created from the vacuum. If the energy stored in the color string between the sources of the heavy quark potential exceeds a certain critical value at some distance, $r = r_c$, the string will "break" and decay into two static-light mesons, separated by a distance r. Therefore, for large distances, the ground state energy will stop rising with distance and saturate at a constant level. The static sources will be completely screened by light quarks that are created out of the vacuum.
The other effect will change the potential at short distances. While the vacuum polarisation due to gluons has an anti-screening effect on fundamental sources, sea quarks result in screening. Therefore, the running of the QCD coupling with the distance is slowed down with respect to the quenched approximation. The effective Coulomb strength in the presence of sea quarks should, therefore, remain at a higher value than in the quenched case for short distance [66, 67].
The heavy quark potential at zero temperature can be calculated using Wilson loops. While string breaking has not been detected in the Wilson loop [55], the finite temperature potential, extracted from Polyakov loop correlators at temperatures close to the deconfinement phase transition exhibits a flattening, once sea quarks are included into the action [2, 68]. Unlike Wilson loops, Polyakov loop correlators automatically have a non-vanishing overlap with any excitation, containing static quark and anti-quark, separated by a distance r. In particular the static quarks can be accompanied by two disjoint sea quark loops, encircling the temporal boundaries, while in the Wilson loop case, copropagating sea quarks are terminated by the extension of the Wilson loops

2.4 Chiral Condensate

QCD at low energies is well approximated by a theory with only the two lightest quarks (u and d). They are mixed by the $SU(2)_V$ isospin symmetry group. This symmetry is

exact for degenerate quark masses. For massless quarks there is an additional symmetry described by the axial $SU(2)_A$ group. The right-handed and left-handed quarks can be rotated independently and the helicity is a good quantum number. The chiral symmetry group in the massless case for two flavours is therefore $G = SU(2)_V \times SU(2)_A$ which is isomorphic to $O(4)$. A non-zero mass term breaks this symmetry explicitly analogous to a magnetic field in a spin system. Even in the massless case, the axial part of the symmetry group G is broken spontaneously by a non-zero expectation value of the chiral condensate in the vacuum state, which mixes right-handed and left-handed quarks. The Goldstone theorem tells us that the spontaneous breaking of continuous symmetries leads to low-lying excitations, the Goldstone modes, with a mass that vanishes in the absence of a symmetry breaking field. The Goldstone modes in QCD, analogous to spin waves in spin systems, are the pions with a mass that is well below the typical hadronic mass scale of about 1 GeV.
The expectation value of the chiral condensate should become zero beyond a critical temperature or a critical chemical potential, where the chiral symmetry gets restored. The restoration of the chiral symmetry at high temperatures and zero density is confirmed by lattice QCD calculations which show a critical temperature of about 170 MeV.
The QCD partition function can be written as a functional integral in Euclidean space,

$$Z = \int DA_\mu \prod_{f=1}^{N_f} \det(\mathcal{D} + m_f) e^{-S_G}, \tag{2.37}$$

where N_f is the number of quark flavours and S_G is the gluonic part of the action. The QCD Dirac operator is given by

$$\mathcal{D} = \gamma_\mu(\partial_\mu + igA_\mu) \tag{2.38}$$

with non-abelian gauge fields A_μ. This operator is anti-hermitian, $\mathcal{D}^\dagger = -\mathcal{D}$, and satisfies

$$\{\gamma_5, \mathcal{D}\} = 0 \tag{2.39}$$

This relation is a compact expression of chiral symmetry, i.e. of the fact that right-handed and left-handed quarks can be rotated independently. One can write down an eigenvalue equation for the Dirac operator $\mathcal{D}$,

$$\mathcal{D}\psi_n = i\lambda_n \psi_n. \tag{2.40}$$

From eq. (2.39) follows that the non-zero eigenvalues of $\mathcal{D}$ occur in pairs $\pm i\lambda_n$ with eigenfunctions ψ_n and $\gamma_5\psi_n$. There can also be zero eigenvalues, $\lambda_n = 0$. The corresponding eigenfunctions can be arranged to be simultaneous eigenfunctions of γ_5 with definite chirality and eigenvalues ± 1.
In a chiral basis with

$$\gamma_5 \psi^{R/L} = \pm \psi^{R/L} \tag{2.41}$$

one can use (2.39) to show that

$$\langle \psi_m^R | \mathcal{D} | \psi_n^R \rangle = 0 = \langle \psi_m^L | \mathcal{D} | \psi_n^L \rangle \tag{2.42}$$

for all m and n. Based on the eigenvalue equation (2.40) the spectral density of the Dirac operator can be defined by

$$\rho(\lambda) = \left\langle \sum_n \delta(\lambda - \lambda_n) \right\rangle . \tag{2.43}$$

The spectral density is related to the order parameter for spontaneous chiral symmetry breaking, the chiral condensate,

$$\langle \bar{\psi}\psi \rangle = - \lim_{m_f \to 0} \lim_{V \to \infty} \frac{1}{V} \frac{\partial}{\partial m_f} \log Z(m_f). \tag{2.44}$$

Using eq. (2.37), this yields

$$\langle \bar{\psi}\psi \rangle = - \lim_{m_f \to 0} \lim_{V \to \infty} \left\langle \frac{1}{V} \sum_n \frac{1}{i\lambda_n + m_f}. \right\rangle . \tag{2.45}$$

Since the non-zero eigenvalues occur in pairs $\pm i\lambda_n$, their contribution to the sum can be written as $2m_f/(\lambda_n^2 + m_f^2)$. In the infinite volume limit, the sum over the eigenvalues can be converted to an integral and in the limit $m \to 0$ (2.45) leads to the Banks-Casher relation [69],

$$\Sigma \equiv |\langle \bar{\psi}\psi \rangle| = \lim_{m_f \to 0} \lim_{V \to \infty} \frac{\pi \rho(0)}{V}. \tag{2.46}$$

This relation shows that spontaneous breaking of the chiral symmetry is encoded in an accumulation of the small Dirac eigenvalues. The order parameter is non-zero only if $\rho(0)/V > 0$.
In lattice QCD the chiral condensate on a lattice of size $N_\sigma^3 N_\tau$ can directly be derived from the partition function

$$\langle \bar{\psi}\psi \rangle = \frac{1}{N_\sigma^3 N_\tau} \frac{N_f}{4} \frac{\partial}{\partial m_f a} \log Z(m_f a) \tag{2.47}$$

$$= \frac{1}{N_\sigma^3 N_\tau} \frac{N_f}{4} \left\langle \mathrm{Tr}\ M^{-1} \right\rangle . \tag{2.48}$$

The factor $N_f/4$ corrects for the number of flavours (for staggered fermions). Results for two flavours of staggered fermions in the full QCD theory are described in [70] and a discussion of the flavour dependence of the chiral phase transition for different numbers of flavours can be found in [71].
The chiral condensate can also be evaluated in the quenched theory [72], i.e. infinite quark mass limit for dynamical quarks. Therefore one calculates the inverse of the fermion matrix (2.48) on gauge configurations obtained by using only the gluonic part of the action in the update scheme.
The mass term in full QCD breaks the $Z(3)$ symmetry of the action explicitly. Gauge configurations with a Polyakov loop expectation value in the complex $Z(3)$ sectors are suppressed. In the quenched theory, configurations with Polyakov loops in the three different $Z(3)$ sectors are equally probable. The chiral condensate turns out to be sensitive

to different sectors [73, 74]. To understand this problem qualitatively, one may look at the eigenvalue spectrum of the free Dirac operator [75], i.e. $A_\mu = 0$, as this is connected to the chiral condensate via (2.46). A $Z(3)$ transformation on the gauge fields,

$$U(\vec{x}, 1/T) = zU(\vec{x}, 0) \tag{2.49}$$

with $z = \exp(2\pi i/3\ j),\ j = 0..2$, changes the boundary conditions in the Euclidean time direction for the fermion fields from antiperiodic,

$$\psi(\vec{x}, 1/T) = -\psi(\vec{x}, 0) \tag{2.50}$$

to twisted,

$$\psi(\vec{x}, 1/T) = -z\psi(\vec{x}, 0). \tag{2.51}$$

The spectrum of the Dirac operator in the $z = 1$ sector is given by $\lambda^2 = \vec{k}^2 + ((2n+1)\pi T)^2$, while in the other two sectors becomes $\lambda^2 = \vec{k}^2 + ((2n+1/3)\pi T)^2$. The smallest eigenvalue moves from $\lambda = \pi T$ to $\lambda = \pi T/3$. Thus the chiral condensate in the two complex sectors is larger than in the real sector. This behaviour was also shown by calculating the effective potential for the chiral condensate of a Nambu-Jona-Lasinio model in a uniform temperature dependent A_0 gauge field background [74, 76]. This behaviour was also discussed in terms of the Gross-Neveu model [77].

Chapter 3

The quenched limit at non-zero baryon number

A numerical analysis of the thermodynamics at fixed quark number B can closely follow the standard approach at $B = 0$, i.e. in a pure $SU(3)$ gauge theory [48]. After describing the details of the simulation and a discussion of the sign problem at non-zero quark number density we analyze the temperature dependence of bulk thermodynamics, the Polyakov loop expectation value and its susceptibilities and the free energy density. Heavy quark potentials are calculated using Polyakov loop correlations. They are compared with quenched and full QCD results at zero density. Finally the chiral condensate is calculated on quenched configurations at non-zero density. All results are compared with quenched data at zero density.

3.1 Details of the simulation

The partition function in the canonical approach for non-zero quark number density in the quenched limit is given by

$$Z(B,T,V) = \int \prod_{n,\nu} \mathcal{D}U_\nu(n) f_B \mathrm{e}^{-S_G}. \tag{3.1}$$

S_G denotes the gluonic part of the action, for which we have used the standard Wilson gauge action described by equation (1.24). The constraint on the baryon number in (3.1) is encoded in the function f_B which depends on the local Polyakov loops. For different values of the quark number B, f_B is calculated using the recurrence relation derived in section 1.9,

$$f_n = -\sum_{i=0}^{n-1} \frac{2}{n} (-1)^{n-i} f_i \sum_{\vec{x}} \mathrm{Tr}\ P_{\vec{x}}^{n-i}. \tag{3.2}$$

with $f_0 = 1$ and the symmetry $f_n = f^*_{6V-n}$. $P_{\vec{x}}$ denotes the local Polyakov loop at site $\vec{x}$. The expressions for some values of the quark number B are calculated section 1.9.
The global $Z(3)$ symmetry of the QCD partition function at non-zero quark number is preserved also in the quenched limit, i.e. the function f_B is invariant under global $Z(3)$ transformations if B is a multiple of 3. As the gluonic action S_G also shares this property, the partition function $Z(B,T,V)$ is non-zero only if B is a multiple of 3.
The function f_B is a complex valued function of the Polyakov loops, but when integrating over all gauge fields in the canonical partition function (3.1), the contribution from the imaginary part of f_B vanishes and the partition function is real, as it should be. Actual calculations can thus be performed using the real part of f_B. The sign problem that remains in this formulation can be handled by shifting the dependence on the sign into the observables and using a reweighting method [78] to calculate expectation values according to

$$\langle \mathcal{O} \rangle = \frac{\langle \mathcal{O} \cdot \mathrm{sgn}(\mathrm{Re} f_B) \rangle_{||}}{\langle \mathrm{sgn}(\mathrm{Re} f_B) \rangle_{||}}, \tag{3.3}$$

where the expectation values $\langle \dots \rangle_{||}$ are calculated using the partition function

$$Z_{||}(B,T,V) = \int \prod_{x,\nu} \mathcal{D}U_{x,\nu} |\mathrm{Re} f_B| \mathrm{e}^{-S_G}. \tag{3.4}$$

Our simulations were performed using a combination of a Metropolis update and over-relaxation steps to reduce autocorrelations. Each sweep consists of one Metropolis and four over-relaxation steps. Measurements of the observables were performed after each sweep. For each link update the change in the function f_B is calculated and a possible change in sign is monitored. The errors on observables were calculated using a Jackknife error analysis with 10 Jackknife-blocks. Interpolations were performed using the Ferrenberg Swendsen method.

$N_\sigma^3 \times N_\tau$	B	n_B/T^3	$N_\sigma^3 \times N_\tau$	B	n_B/T^3
$8^3 \times 2$	0	0.0000	$8^3 \times 4$	6	0.2500
$8^3 \times 2$	6	0.0313	$10^3 \times 4$	6	0.1280
$8^3 \times 2$	12	0.0625	$12^3 \times 4$	6	0.0741
$10^3 \times 2$	0	0.0000	$16^3 \times 4$	0	0.0000
$10^3 \times 2$	12	0.0320	$16^3 \times 4$	6	0.0313
			$16^3 \times 4$	12	0.0625

Table 3.1: *Lattice sizes and densities of the simulations.*

Our simulations have been carried out in the vicinity of the critical coupling for the deconfinement transition at $B = 0$. Calculations with fixed B were performed on lattices of size $N_\sigma^3 \times N_\tau$ with $N_\tau = 2$ and 4 and various values for N_σ. The temperature is varied by changing the coupling $\beta = 6/g^2$. The temperature scales in our plots are set by a strong coupling expansion of the string tension [79] for the $N_\tau = 2$ results, resp. by the β-function of [48] for $N_\tau = 4$. The dimensionless parameter kept fixed in the simulation is the quark number density in units of the temperature cubed,

$$\frac{n_B}{T^3} = \frac{B}{3} \left(\frac{N_\tau}{N_\sigma} \right)^3. \tag{3.5}$$

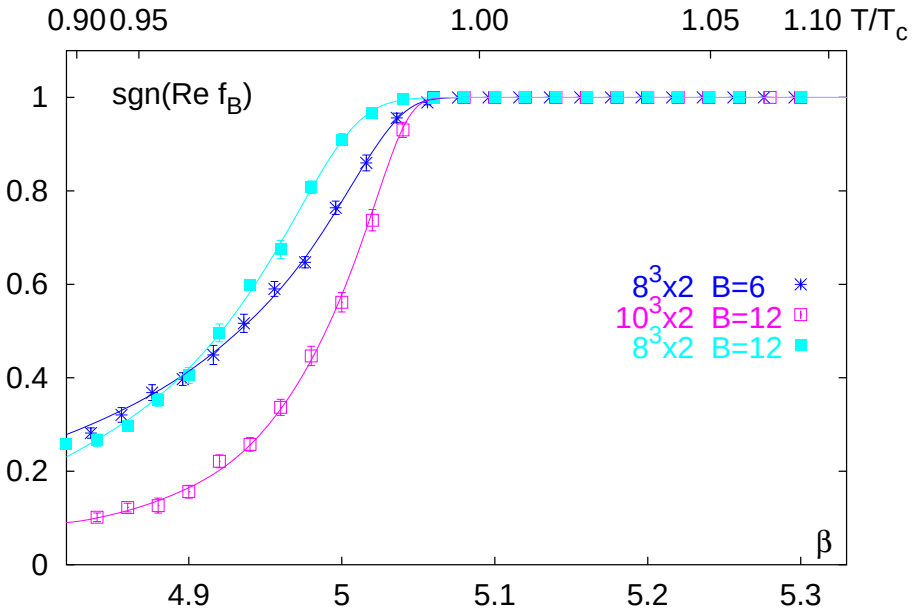

Figure 3.1: *Expectation value of the sign of* $\mathrm{Re}f_B$, $\langle \mathrm{sgn}(\mathrm{Re}f_B)\rangle_{||}$, *for* $N_\sigma^3 \times 2$.

The quark number density in physical units thus is

$$n_B = \frac{B}{3}\left(\frac{N_\tau}{N_\sigma}\right)^3 \left(\frac{T}{200\ \mathrm{MeV}}\right)^3 \mathrm{fm}^{-3}. \tag{3.6}$$

For orientation we note that close to T_c, which for the $SU(3)$ gauge theory is known to be about 270 MeV, a simulation on an $8^3 \times 2$ or $16^3 \times 4$ lattice with $B = 12$ corresponds to a baryon number density of $n_B \simeq 0.15/\mathrm{fm}^3$, i.e. approximately nuclear matter density. The various lattice sizes and densities of our simulations are listed in Tab. 3.1.

3.2 The sign problem

In all cases we have studied, we find that $\langle \mathrm{sgn}(\mathrm{Re}f_B)\rangle_{||}$ can be well determined and is positive and non-zero. Figures 3.1 and 3.2 show the average sign as a function of the coupling β. For large values of the coupling it is almost always positive and there is no sign problem. Below the critical coupling the average sign drops exponentially.
Looking at a fixed volume we see only a small dependence of the average sign on the density that indicates that the onset of the sign problem is shifted toward smaller values of β and the drop is steeper. The expectation value of $\mathrm{sgn}(\mathrm{Re}f_B)$ mainly depends on the spatial volume N_σ^3, but even for a $16^3 \times 4$ lattice the average sign can be determined quite well in the studied β-region and is non-zero within the errors. We will see later that the values of observables do not depend much on the sign. The error obtained from a jackknife

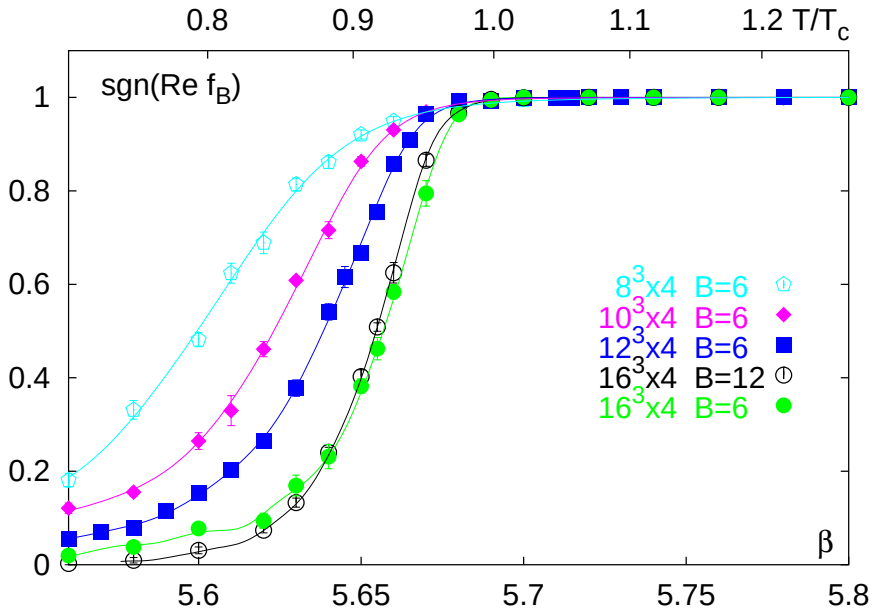

Figure 3.2: *Expectation value of the sign of* $\mathrm{Re}f_B$, $\langle \mathrm{sgn}(\mathrm{Re}f_B)\rangle_{||}$, *for* $N_\sigma^3 \times 4$.

analysis for these observables are substantially smaller than those for the average sign.
Looking at the definition of f_B it is obvious that $\mathrm{sgn}(\mathrm{Re}f_B)$ on a single configuration is correlated to the value of the Polyakov loop on this configuration. Figure 3.3 shows the distribution of the Polyakov loop in the complex plane spanned by $\mathrm{Re}(\mathrm{Tr}L)$ and $\mathrm{Im}(\mathrm{Tr}L)$ for $B = 0$ and 6 calculated on a $16^3 \times 4$ lattice for different values of the coupling β. For vanishing density and small coupling the Polyakov loops are distributed symmetrical around a value of 0. Near the critical coupling three additional regions are visible, which reflects the Z(3) symmetry of the action. At large couplings $\mathrm{Tr}L$ is distributed in one of the cones due to spontaneous breaking of the Z(3) symmetry.
For $B = 6$ and small coupling the Polyakov loops with positive and negative contributions are again distributed around 0. Near the phase transition one sees 6 (or in general B) different cones for the positive and negative distribution. To understand this one can look at the leading order in f_B in the dilute limit, for $B \ll N_\sigma^3$,

$$f_B \sim \left(\sum_{\vec{x}} \mathrm{Tr}L_{\vec{x}}\right)^B \sim |L|e^{iB\phi}, \tag{3.7}$$

where ϕ is the angle of $L = \sum_{\vec{x}} \mathrm{Tr}L_{\vec{x}}$ in the complex plane. This explains the existence of B positive and B negative cones in the distributions. For large values of the coupling $\mathrm{Tr}L$ is distributed in one of the Z(3) cones and therefore the sign of f_B is always positive for large β.
The role of the Polyakov loop in the grand canonical approach was discussed in [80]. In the static limit [46] the phase of the fermion determinant is strongly correlated to the imaginary part of the Polyakov loop. This might also be the case for full QCD with

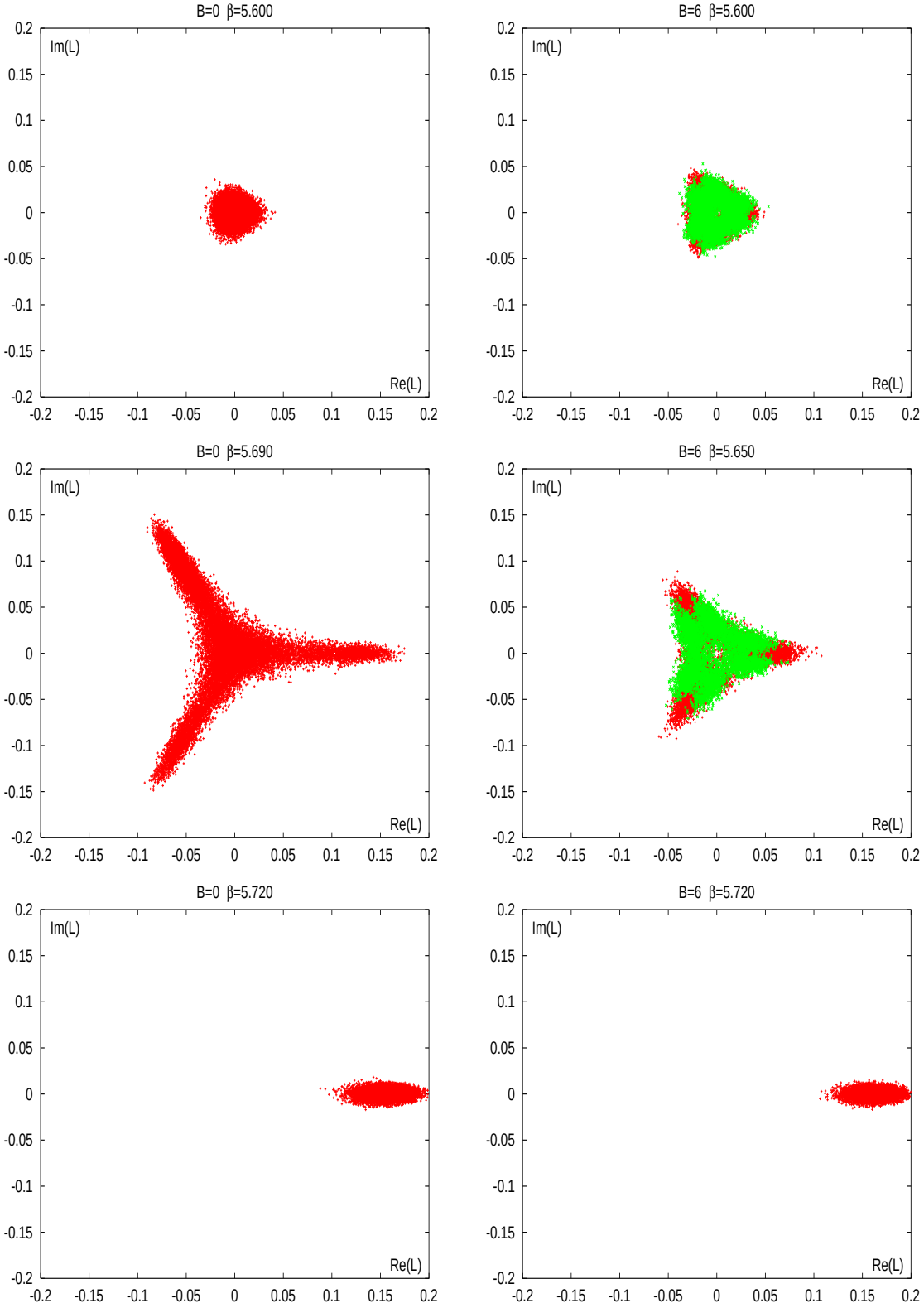

Figure 3.3: *Polyakov loop distribution in the complex plane spanned by* $\mathrm{Re}(\mathrm{Tr}L)$ *and* $\mathrm{Im}(\mathrm{Tr}L)$ *for* $B = 0$ *(left) and* $B = 6$ *(right) on a* $16^3 \times 4$ *lattice and different* β*-values. Red points are Polyakov loops that give a positive* f_B *and green points give a negative* f_B*.*

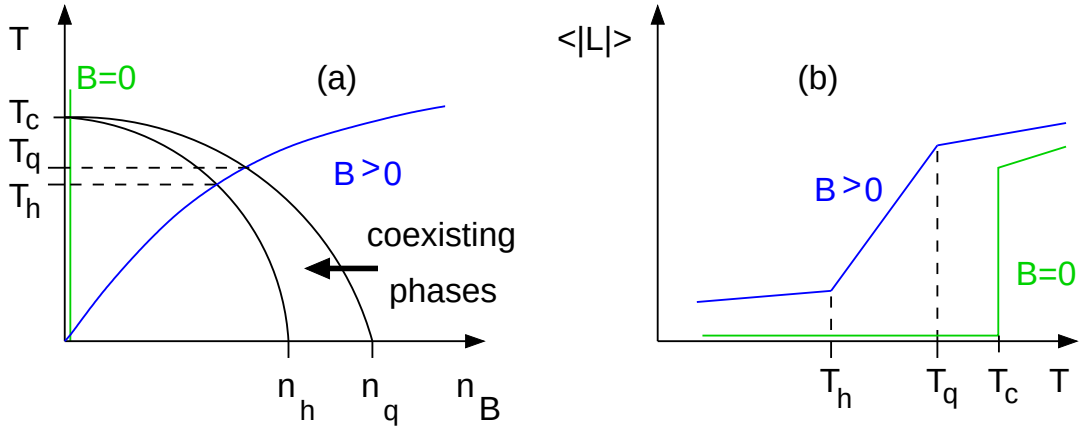

Figure 3.4: *Schematic plot of the QCD phase diagram (a) in the temperature-baryon number density plane for the case of first order phase transitions in the entire plane. For $B > 0$ and $T_h < T < T_q$ the system stays in a region of two coexisting phases. For $B = 0$ the transition occurs at a unique temperature T_c. In (a) we also show the paths followed when varying the coupling β in a Monte-Carlo simulation with fixed B, N_σ and N_τ. In (b) the expected behaviour of the Polyakov loop expectation value along these paths of non-zero B as well as for $B = 0$ is shown.*

dynamical quarks for large quark masses as in an expansion for large quark mass the leading term affected by the chemical potential is the Polyakov loop.

3.3 The deconfinement phase transition

To analyze the phase transition separating the confined phase for small temperatures and the high temperature deconfined phase, we have calculated expectation values of the Polyakov loop in a temperature range of $T \approx 0.8 \ldots 1.2\ T_c$ for different lattice sizes and various densities shown in Table 3.1. The results for $\langle |L| \rangle_V$ are shown in figure 3.5 (for $N_\tau = 2$) and figure 3.6 (for $N_\tau = 4$). The solid lines in the figures are interpolations using the Ferrenberg-Swendsen method.
For vanishing quark number density there is a clear signal for a first order phase transition which leads to a discontinuity in $\langle L \rangle$. The pseudo-critical couplings of $\beta = 5.069(1)$ for the $8^3 \times 2$ and $10^3 \times 2$ lattices at $B = 0$ are compatible with the result from [72], and for the $16^3 \times 4$ lattice with the result from [48], $\beta_c = 5.6908(2)$. The Polyakov expectation values drop from large values at high temperatures to small values at the critical temperature. $\langle |L| \rangle_V$ does not become zero because of the finite volumes, but the data for the $8^3 \times 2$ and $10^3 \times 2$ lattices indicate that in the infinite volume limit, $\langle L \rangle$ becomes zero at zero density for $T < T_c$ while it stays finite for $T > T_c$.
For all $B > 0$ we clearly observe a transition from a low temperature phase with small Polyakov loop expectation value to the high temperature regime characterised by a large Polyakov loop expectation value. Comparing the data for the $8^3 \times 2$ lattice at $B = 6$ with

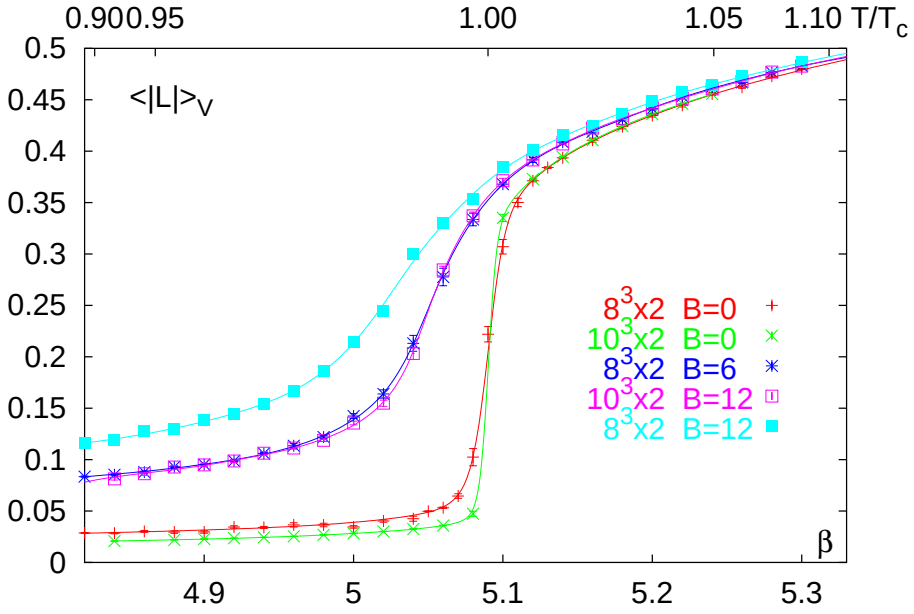

Figure 3.5: *Expectation value of the Polyakov loop for* $N_\sigma^3 \times 2$.

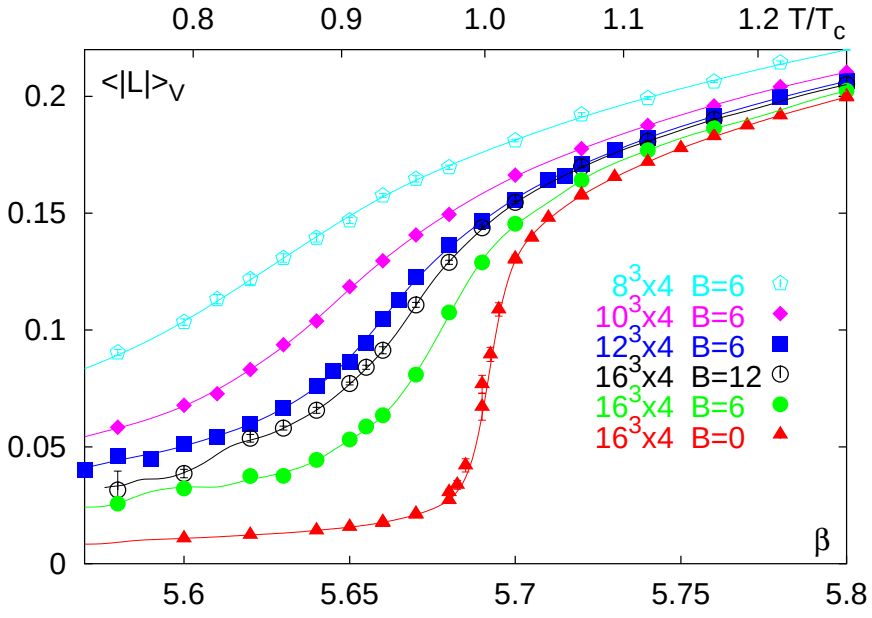

Figure 3.6: *Expectation value of the Polyakov loop for* $N_\sigma^3 \times 4$.

the $10^3 \times 2$ lattice at $B = 12$, which correspond to approximately the same density of $n_B/T^3 = 0.0313$ respectively 0.0320, we see no significant volume dependence at fixed n_B. This indicates that in the thermodynamic limit the physical observables will only depend on the density rather than on quark number and volume separately. It also indicates that for the small temperature regime the Polyakov loop $\langle L \rangle$ stays finite for non-zero density while it gets zero for vanishing density.
For non-vanishing density the transition occurs in a temperature interval that broadens with increasing quark number density and gets shifted towards smaller temperatures. There is no indication for a discontinuous transition in contrast to the $B = 0$ case. In fact, this is the expected behaviour in a canonical calculation, even if the transition is of first order. By changing the gauge coupling β we vary the lattice cut-off and through this also the quark number density continuously through a region of two coexisting phases. This situation is schematically illustrated in figure 3.4. The question now is whether the transition region really is a region of coexisting phases. In this case the values of thermodynamic observables result as the superposition of contributions from two different phases appropriately weighted by the fraction each phase contributes to the coexistence region (for an illustration see e.g. figure 3.4b).
To gain further insight into the structure of this regime we also analyze various susceptibilities. In figures 3.7 and 3.8 we show the conventional Polyakov loop susceptibility,

$$\chi_L = N_\sigma^3 \left(\langle |L|^2 \rangle - \langle |L| \rangle^2 \right), \tag{3.8}$$

and in figures 3.9 and 3.10 the derivative of $\langle |L| \rangle$ with respect to β,

$$\chi_\beta = \frac{\partial \langle |L| \rangle}{\partial \beta} = N_\sigma^3 \left(\langle |L| \times S_G \rangle - \langle |L| \rangle \langle S_G \rangle \right). \tag{3.9}$$

Both response functions reflect the existence of a transition region that becomes broader with increasing n_B and is shifted towards smaller temperatures. Compared to the behaviour at $B = 0$ they also change continuously in this region. Such a behaviour might as well just correspond to a smooth crossover to the high temperature regime; a conclusion also drawn from the heavy quark simulations with non-zero chemical potential [46]. To establish the existence of a region of coexisting phases with certainty will thus require a further, detailed analysis of finite size effects.

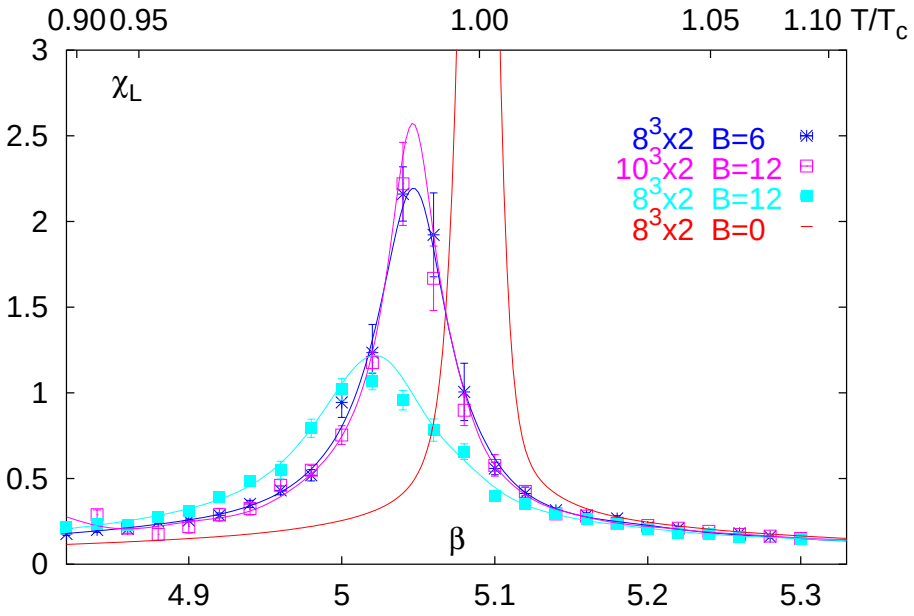

Figure 3.7: *Expectation value of the Polyakov loop susceptibility for* $N_\sigma^3 \times 2$.

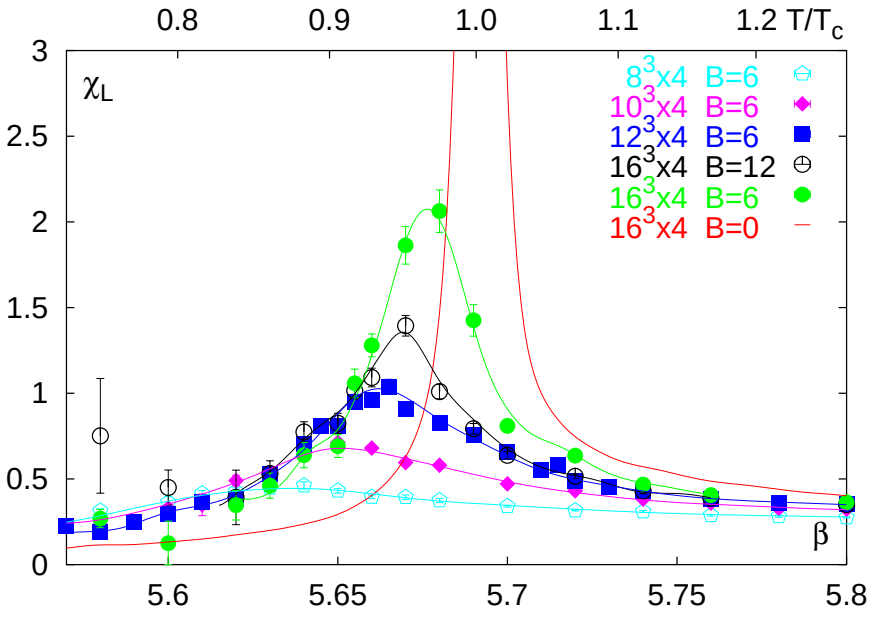

Figure 3.8: *Expectation value of the Polyakov loop susceptibility for* $N_\sigma^3 \times 4$.

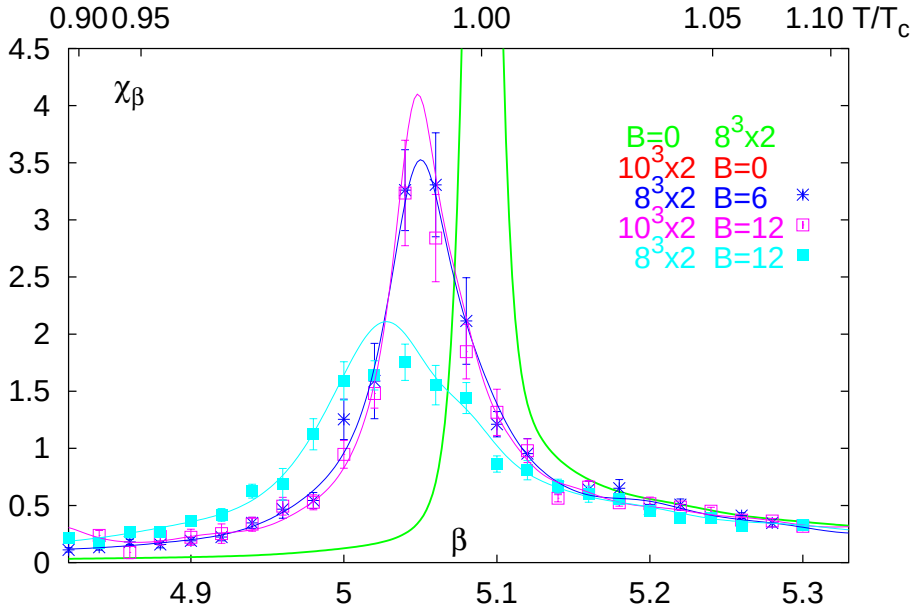

Figure 3.9: *Expectation value of the susceptibility χ_β, as defined in (3.9), for $N_\sigma^3 \times 2$.*

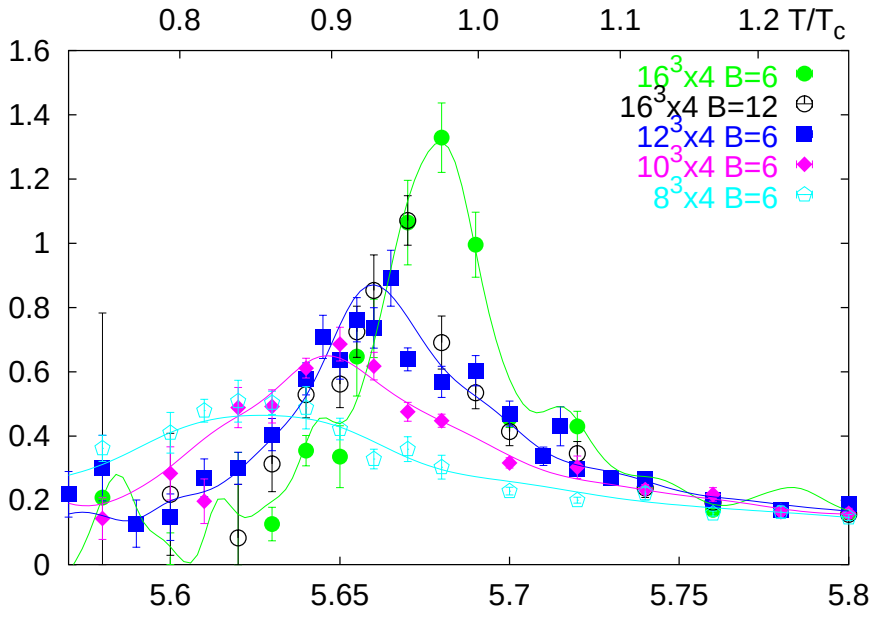

Figure 3.10: *Expectation value of the susceptibility χ_β, as defined in (3.9), for $N_\sigma^3 \times 4$.*

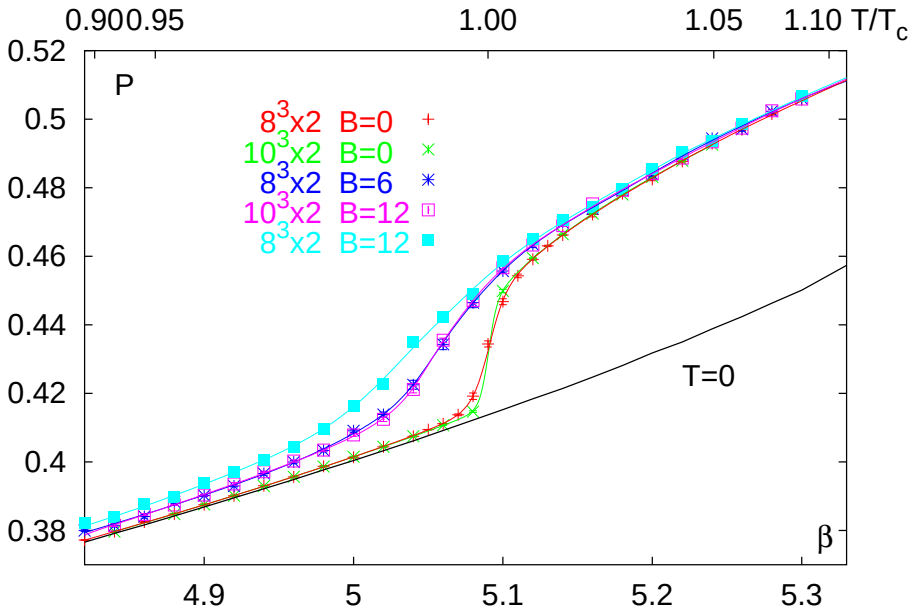

Figure 3.11: *Plaquette expectation value P for $N_\sigma^3 \times 2$.*

3.4 Thermodynamics

Although in principle all thermodynamic quantities can be derived from the free energy density, in practice a direct computation of the partition function or free energy on the lattice is not possible. A way out is to calculate the expectation value of the action, i.e. the derivative of $\ln Z$ with respect to the bare coupling β. Up to a normalisation constant, resulting from the lower integration limit β_0, the free energy density is then obtained by integrating this expectation value

$$\frac{f}{T^4}|_{\beta_0}^{\beta} = -N_\tau^4 \int_{\beta_0}^{\beta} d\beta' \left[S_0 - S_T\right], \tag{3.10}$$

where S_0 and S_T denote the expectation value of the action for zero and finite temperature. We have used the zero density results for the action at zero temperature S_0 for all densities, because a calculation of S_0 at non-zero density is impossible due to the sign problem. To calculate the free energy density using (3.10), we have calculated the plaquette expectation values,

$$P = \frac{1}{6V} \sum_{n,\mu<\nu} \frac{1}{2N_c} \mathrm{Tr}\, \{U_{\mu\nu}(n) + U_{\mu\nu}^\dagger(n)\}, \tag{3.11}$$

as they appear in the definition of the action (1.24).
Figure 3.11 ($N_\tau = 2$) and 3.12 ($N_\tau = 4$) show the results for P for the different lattice sizes and quark number densities shown in Table 3.1. These results show a similar behaviour

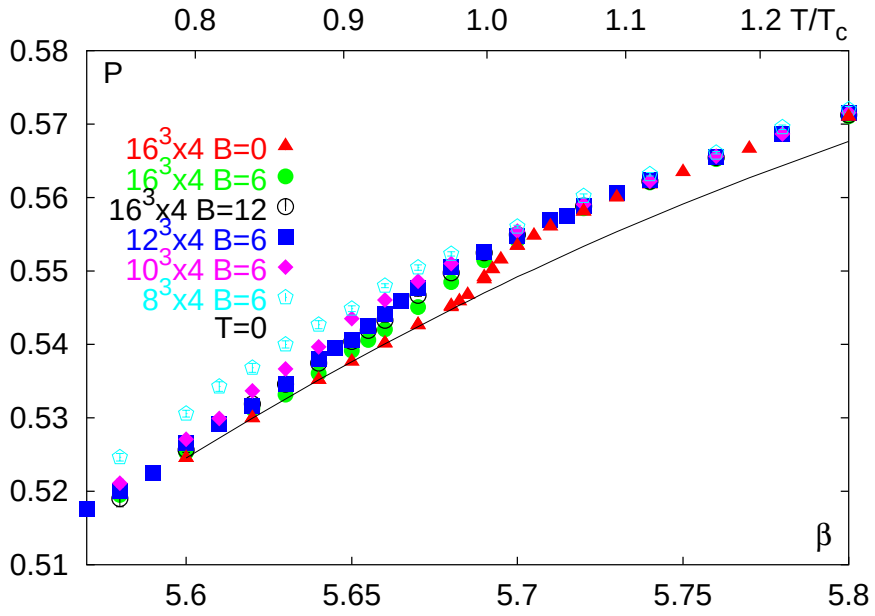

Figure 3.12: *Plaquette expectation value for* $N_\sigma^3 \times 4$.

like the Polyakov loop expectation values. We see a broadening of the transition region with increasing quark number density and a shift of the transition region towards smaller temperatures. Important for the calculation of the free energy density is the fact that the region between the zero temperature and finite temperature results for the action,

$$\Delta S = S_0 - S_T, \tag{3.12}$$

shown in figure 3.13 and 3.15, grows with increasing density. This leads to a decrease of the free energy density with increasing n_B as can be seen in figure 3.14 and 3.16. For large values of the coupling, i.e. large temperatures, the plaquette expectation values for non-zero densities tend to the zero density results and therefore the qualitative behaviour of the free energy density is comparable for all values of B, but shifted toward smaller values of f/T^4 with increasing B.
The problem in calculating the free energy density at non-zero quark number density is the limitation to simulate at smaller temperatures due to the sign problem. Because the quark number density n_B/T^3 decreases when decreasing the temperature, the difference between the zero and the non-zero density results should get smaller for smaller values of the coupling β. But as can be seen especially for $N_\tau = 4$ in figure 3.15, the action difference ΔS does not tend to zero at non-zero B for the β-range we have analyzed. Therefore the lower integration limit β_0 in (3.10) is not small enough for our data to get results that are independent of β_0. This problem would lead to a shift of the free energy densities at non-zero B. Therefore the results in figure 3.14 and 3.16 show only a qualitative picture of the free energy.

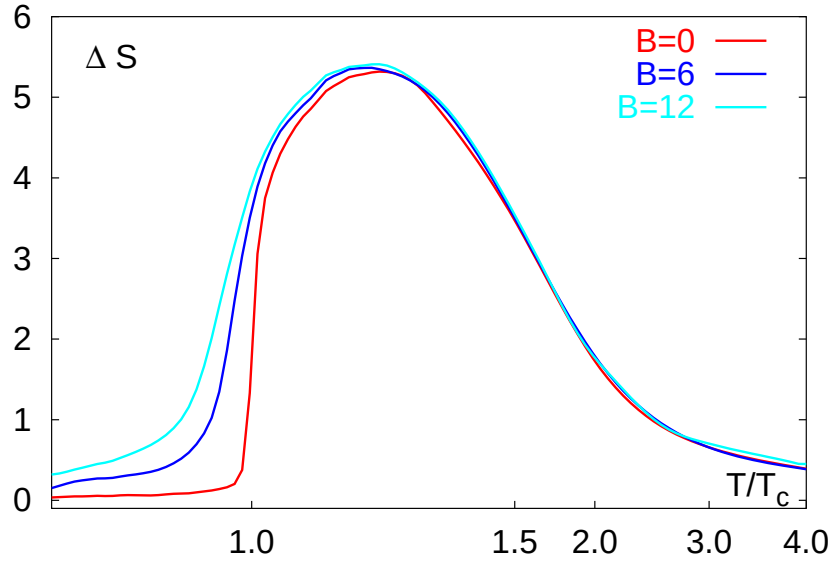

Figure 3.13: *The difference between the zero and finite temperature plaquette expectation values, $\Delta S = S_0 - S_T$, for the $N_\tau = 2$ lattices.*

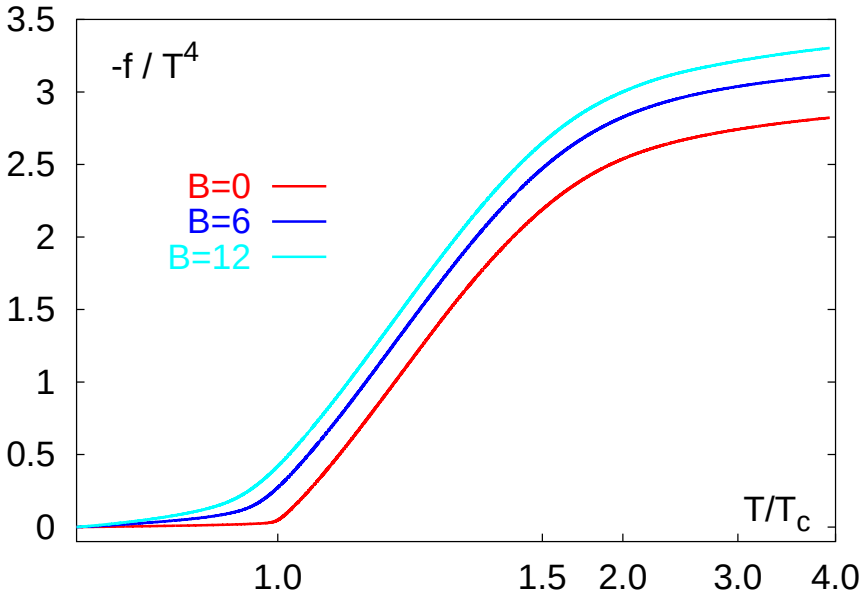

Figure 3.14: *The free energy density $-f/T^4$, defined in (3.10), for the $N_\tau = 2$ lattices.*

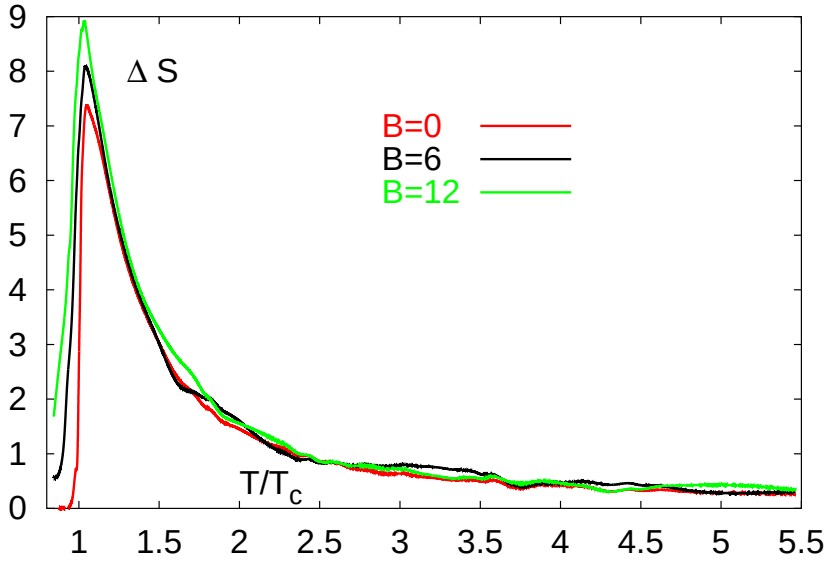

Figure 3.15: *The difference between the zero and finite temperature plaquette expectation values, $\Delta S = S_0 - S_T$, for the $N_\tau = 4$ lattices.*

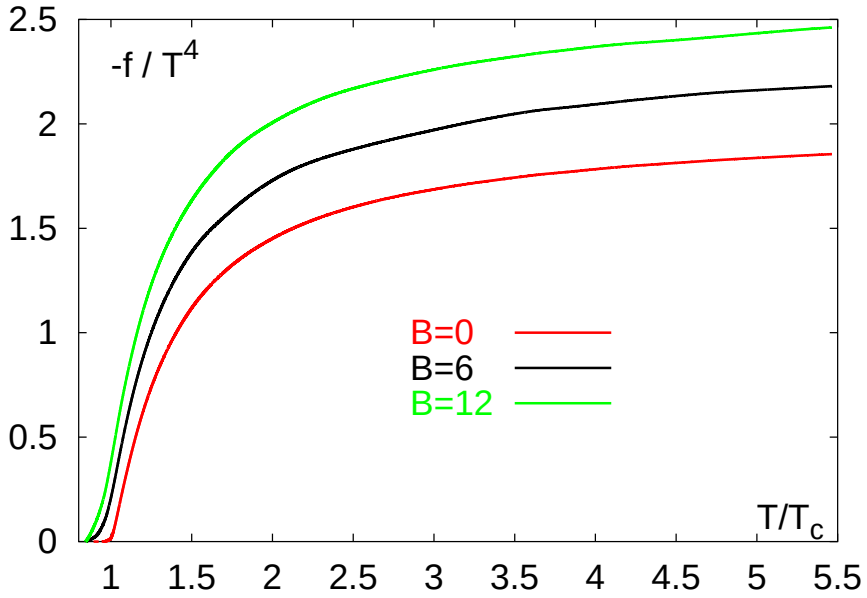

Figure 3.16: *The free energy density $-f/T^4$, defined in (3.10), for the $N_\tau = 4$ lattices.*

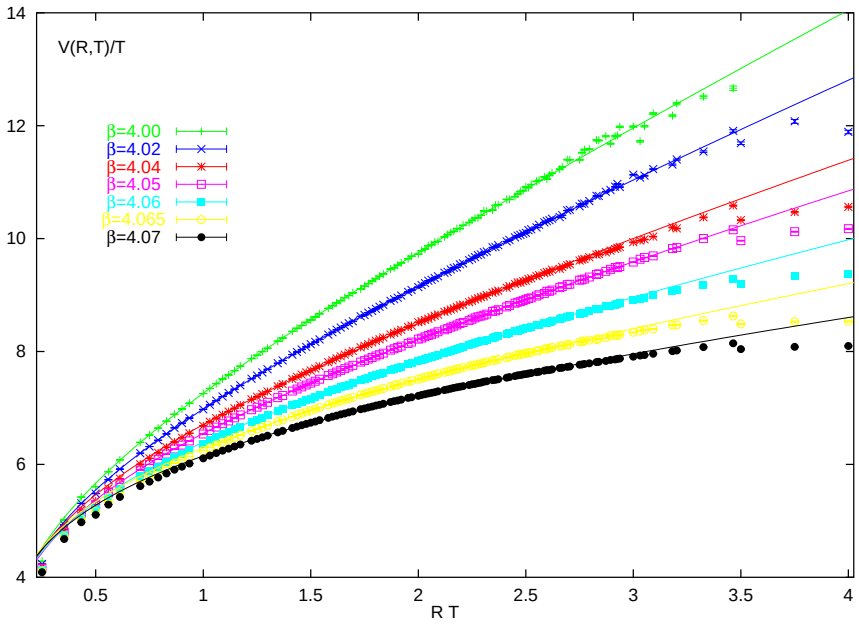

Figure 3.17: *The heavy quark potentials for $T < T_c$ in units of the temperature which is fixed by choosing different values of the coupling β as indicated in the figure.*

3.5 Heavy quark potentials at vanishing density

The results for the heavy quark potential at vanishing density will be discussed in the following paragraph. The results were generated with a tree-level Symanzik-improved gauge action consisting of 1x1 and 2x1 loops on lattices of size $32^3 \times 4$. We used a pseudo-heatbath algorithm [81] with FHKP updating [82, 83] in the $SU(2)$ subgroups. Each heatbath iteration is supplemented by 4 over-relaxation steps [84]. To improve the signal in calculations of Polyakov loop correlation functions link integration [85, 86, 87] was employed. The correlation functions (2.22) for $T < T_c$, resp. (2.30) for $T > T_c$, have been computed for all on-axis separations and almost all off-axis distance vectors $\vec{R}$. For each β-value the data set contains 20000 to 30000 measurements separated by one sweep. The errors on the potentials were determined by a jackknife analysis.

3.5.1 Results below T_c

The results for the potential at temperatures below T_c are shown in figure 3.17. We see that rotational symmetry is quite well satisfied due to the use of an improved action in this case. For the largest separation we see some effects of the periodic boundary conditions which mainly influence the on-axis correlations.
The potentials have been fitted to (2.27) with two free parameters, the self-energy V_0

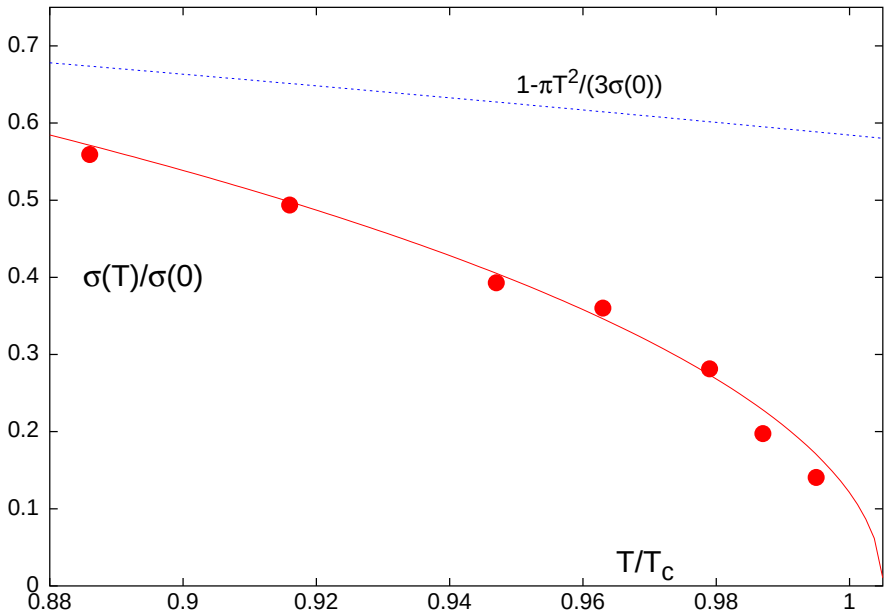

Figure 3.18: *The string tension as obtained from fits with eq. (2.27), normalized to its zero temperature value. The line is the result of a fit to this ratio with the string model motivated ansatz eq. (3.13). The data is compared with the lowest order temperature effect on the linear part of the potential, eq. (2.27).*

and a temperature dependent string tension $\sigma(T)$. A more detailed description of the temperature dependence of the string tension and the logarithmic term in (2.27) can be found in [3]. The resulting temperature dependent string tension, normalized to its zero temperature value is shown in Figure 3.18. The temperature dependence compares well with the (modified) prediction [60] of the Nambu-Goto model

$$\frac{\sigma(T)}{\sigma(0)} = a\sqrt{1 - b\frac{T^2}{T_c^2}}. \tag{3.13}$$

The string model prediction assumes a second order transition with a continuous vanishing of the string tension at the critical temperature. As the deconfinement transition in pure $SU(3)$ gauge theory is known to be of first order, a discontinuity at the critical temperature is expected. To account for this, the coefficients a and b in eq. (3.13) are allowed to deviate from unity. The fit to the data, shown in figure 3.18, results in the values $a = 1.21(5)$ and $b = 0.990(5)$. This leads to a non-vanishing string tension at the critical temperature of

$$\frac{\sigma(T_c)}{\sigma(0)} = 0.121(35). \tag{3.14}$$

This gives a (physical) mass gap at the transition point of $m_{phys}(T_c)/T_c = \sigma(T_c)/T_c^2 = 0.30(9)$, which is a bit below but not incompatible with earlier results of dedicated analyzes of the order of the deconfinement transition, $m_{phys}(T_c)/T_c = 0.4 - 0.8$, as summarized in

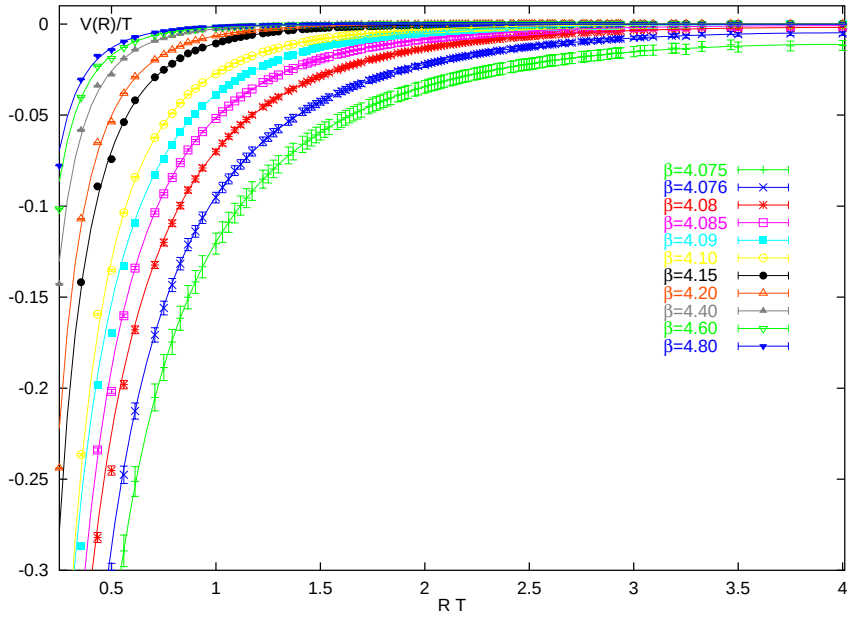

Figure 3.19: *The heavy quark potentials for $T > T_c$ in units set by the temperature for different values of the coupling β. The Polyakov loop correlations have been normalized to their cluster value.*

[88].
The dotted line in figure 3.18 shows the leading order of the temperature dependent string tension $\sigma(T)$ as given in eq. (2.27). One can see that non-leading terms contribute substantially even at temperatures down to 0.88 T_c. The critical behaviour at T_c cannot be understood in terms of the leading order contribution.

3.5.2 Results above T_c

Above the critical temperature we have normalized the Polyakov loop correlations to their cluster value

$$V(|\vec{R}|, T) = -T \log \frac{\langle L(0) L^\dagger(\vec{R}) \rangle}{|\langle L(0) \rangle|^2} \tag{3.15}$$

to eliminate the self-energy contributions. The results in figure 3.19 were obtained with a tree-level Symanzik-improved gauge action on lattices of size $32^3 \times 4$ at vanishing quark number density.
We fit the potentials above T_c with the generalized ansatz (2.36), where the exponent d of the Coulomb part is treated as a free parameter. It turns out that the value of the exponent and the value of the screening mass μ are strongly correlated. These fluctuations have been taken into account in our estimates of the error bars.

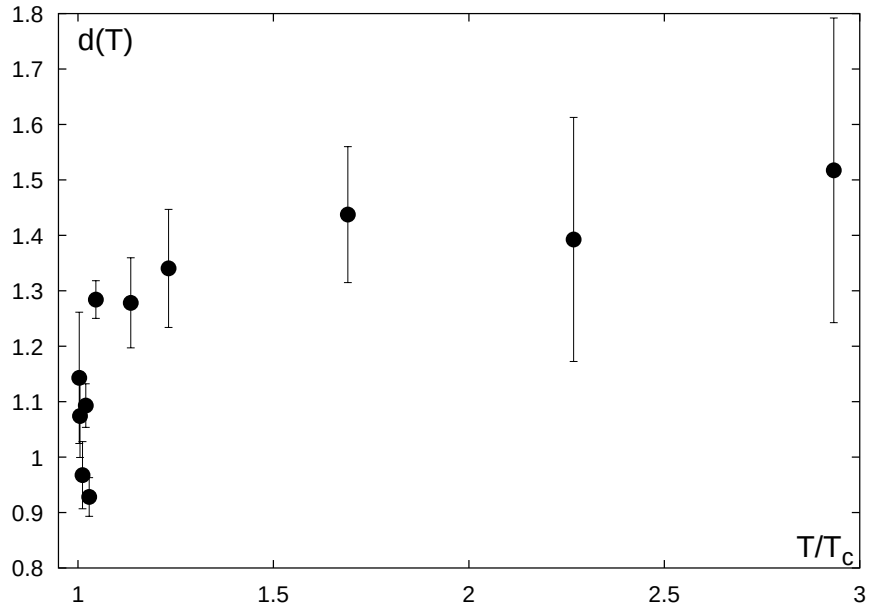

Figure 3.20: *Fit results for the exponent d of the Coulomb -like part of the heavy quark potential above T_c, eq. (2.36), as a function of the temperature.*

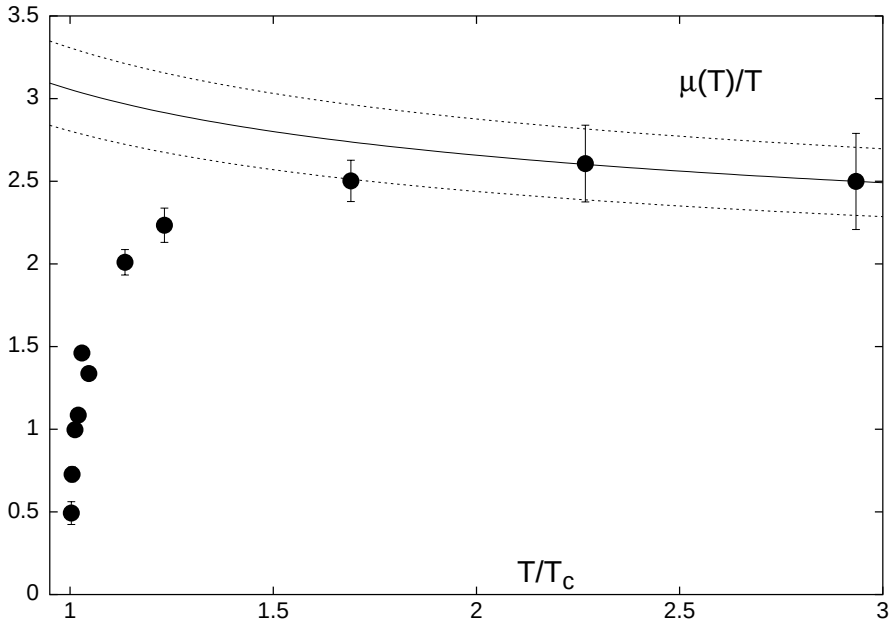

Figure 3.21: *Screening masses $\mu(T)/T$ for vanishing density, computed by fits of eq. (2.19) with a free exponent d.*

At the highest temperatures analyzed we observed that at large quark separations the Polyakov loop correlation decreases below the cluster value. In [65] it was argued that finite momentum contributions to the vacuum polarization tensor can give rise to a modified screening function which undershoots the exponential Debye decay at intermediate distances and approaches the infinite distance limit from below. We have taken an operational approach and have added an overall constant to our fit ansatz.
The results for the exponent d are summarized in figure 3.20. At temperatures very close to T_c the exponent is compatible with 1. When the temperature is increased slightly, d starts rising to about 1.4 for temperatures up to 2 T_c. Between 2 and 3 times T_c, the exponent centers around 1.5 and the error bars tend to become rather large. A value of 2 as predicted by perturbation theory seems to be ruled out in the investigated temperature range. Figure 3.21 shows the results for the screening mass $\mu(T)$ obtained from the same fits with (2.36). The screening mass tends to smaller values near the critical temperature, but stays finite. This is expected due to the first order of the transition. With increasing temperature it rises rapidly and reaches a value of about $2.5T$ at high temperatures. The lines in figure 3.21 show the prediction in lowest order perturbation theory, $\mu(T) = A \times m_e^{(0)}(T)$ with $m_e^{(0)}(T)$ as given in (2.34). For the temperature dependent renormalized coupling $g^2(T)$ the two-loop formula

$$g^{-2}(T) = 2b_0 \ln\left(\frac{2\pi T}{\Lambda_{\overline{MS}}}\right) + \frac{b_1}{b_0} \ln\left(2 \ln\left(\frac{2\pi T}{\Lambda_{\overline{MS}}}\right)\right) \tag{3.16}$$

was used, where $T_c/\Lambda_{\overline{MS}} = 1.14(4)$ [50, 89]; the lattice scale was set by the lowest Matsubara frequency $2\pi T$. The data points for the two highest temperatures, $T > 2\ T_c$, lead to a value of $A = 1.82(15)$, which is close to the perturbation theory prediction of 2. In view of the results for the exponent d we regard this as an accidental coincidence.

3.6 Heavy quark potentials in full QCD

To analyze string breaking in full QCD we have performed simulations with two light flavours of staggered dynamical quarks on lattices of size $16^3 \times 4$ [2] and $12^3 \times 4$ (configurations from [90, 91]) at fixed values for the quark mass of $m_q/T = 0.15$ and 0.075. The couplings were chosen to cover temperatures T below the critical temperature T_c in the range of approximately $0.7 < T < T_c$. The heavy quark potential was extracted from Polyakov loop correlations (2.22). In the limit $R \to \infty$ the correlation function should approach the cluster value $|\langle L(0)\rangle|^2$ which vanishes if the potential is rising at large distances (as we have seen in the quenched potentials below T_c) and which acquires a small but finite value if the string breaks.
In figures 3.23 and 3.22 the data for the potential are presented in lattice units at the values of β analyzed. The critical couplings β_c have been determined as 5.306 for $N_\tau = 4$ and 5.415 for $N_\tau = 6$. The Polyakov loop correlations have been computed for on-axis and for a couple of off-axis distances. Rotational invariance is reasonable well recovered if one uses the lattice Coulomb behaviour to determine the quark-antiquark separation, $|\vec{R}| = 1/G_{lat}(\vec{R})$.

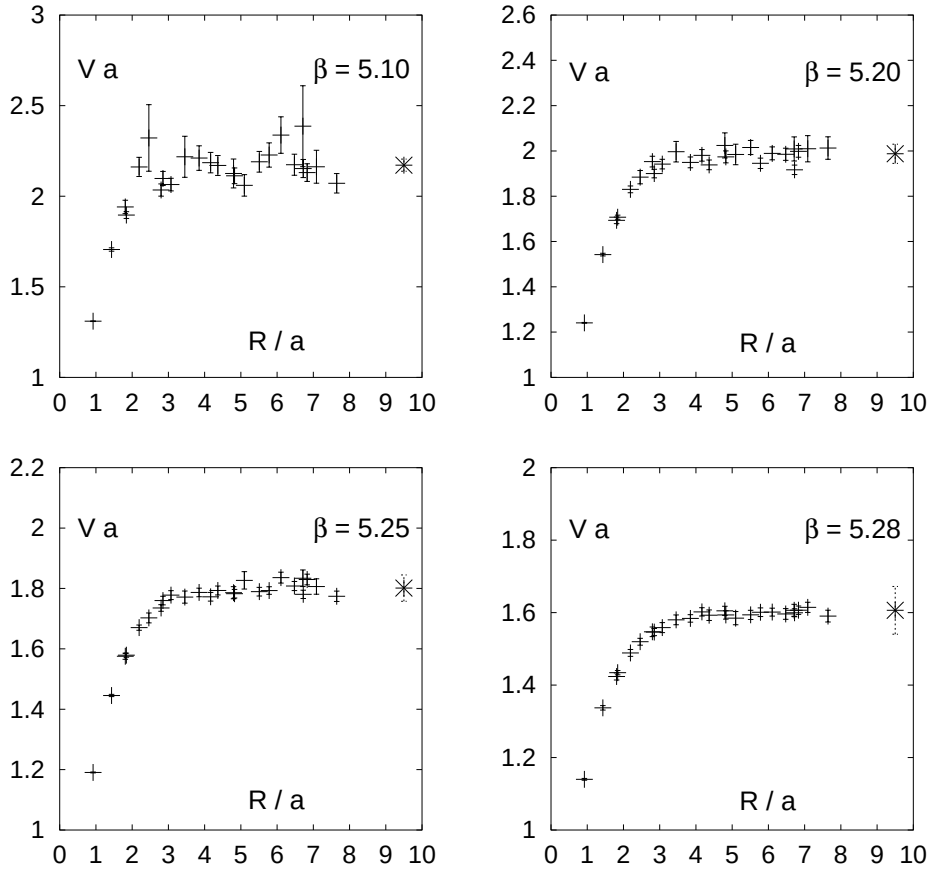

Figure 3.22: *Heavy quark potentials in lattice unites for staggered fermions and* $N_\tau = 4$. *The right-most data points plotted at* $R/a = 9.5$ *and denoted by stars are the infinite distance cluster values* $-T \ln |\langle L \rangle|^2$.

The data quite clearly show a flattening of the potential at lattice distances of about 3 ro 4 lattice spacings, depending on β. This is in agreement with earlier results [92, 68] on smaller lattices of size $8^3 \times 4$. Moreover, the height of the potential at these distances is in nice agreement already with the infinite distance cluster value, shown as the right-most data point in each of the plots.
In figure 3.24 quenched [3] and full QCD [2] potentials are compared. In order to obtain a rough estimate of the corresponding temperatures in units of the critical temperature, the vector meson mass $m_V a$ as well as the ratio of pseudoscalar to vector meson mass, m_{PS}/m_V were estimated. The absolute scale was determined from conventional Wilson loop measurements of the string tension at zero temperatures at the critical β_c values. The dashed line denotes $\pi/(12R) + (420\text{MeV})^2 R$ which gives a good description of the zero temperature quenched potential. Again, the comparison with quenched potentials at the same temperature demonstrates that the potential in the presence of dynamical quarks becomes flat within the error bars at distances of about 1 fm. From figure 3.24

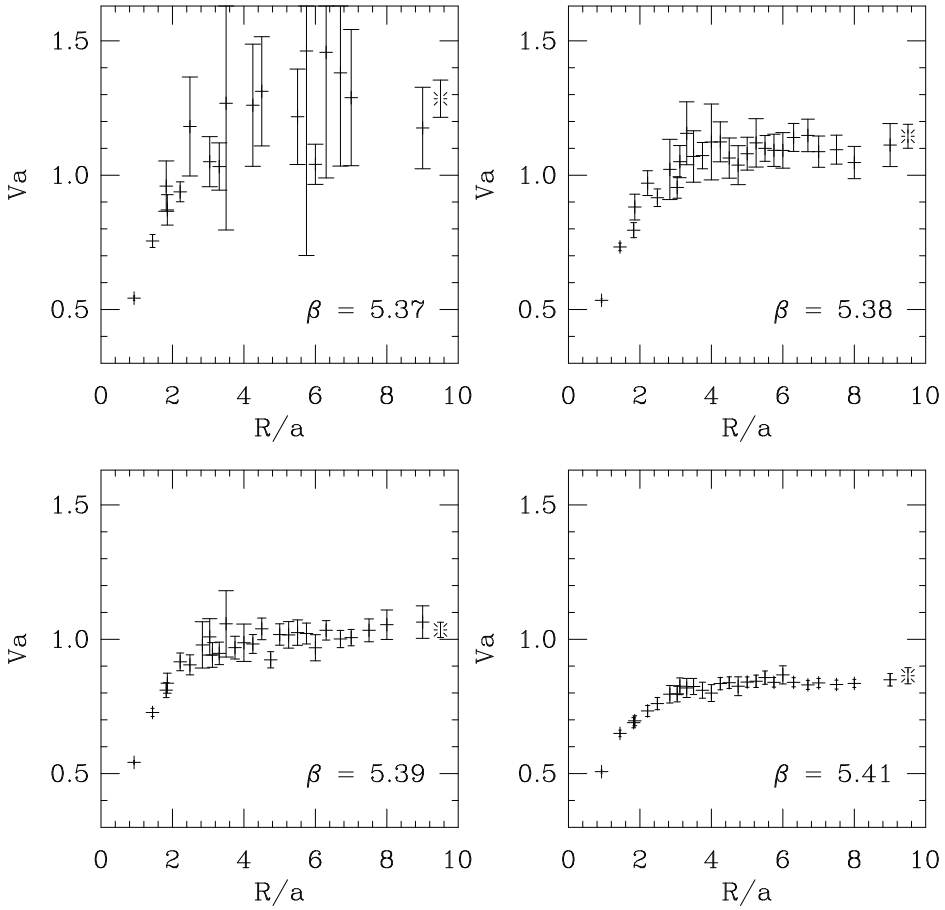

Figure 3.23: *Heavy quark potentials in lattice unites for staggered fermions and* $N_\tau = 6$. *The right-most data points plotted at* $R/a = 9.5$ *and denoted by stars are the infinite distance cluster values* $-T \ln |\langle L \rangle|^2$.

we conclude that the observed string breaking, albeit at finite temperature, is an effect caused by the presence of dynamical fermions.

We have seen that string breaking is relatively easy to observe in the Polyakov loop correlation, while it is difficult to detect through the conventional Wilson loop observable. In the case of string breaking, the ground state of the Hamiltonian is expected to consist of two isolated heavy-light mesons. Such a state with an extra light dynamical quark pair has poor overlap with the flux-tube state which is created by the Wilson loop observable. An improved Wilson loop style determination of the heavy quark potential in full QCD would employ a variational superposition of the flux-tube and two-heavy-meson states [93, 94, 95]. The Polyakov loop approach, on the other hand, although limited in practical application to temperatures close or above T_c, builds in no prejudices about the structure of the static-pair ground state wave function. Screening from light quarks in the thermal ensemble occurs readily.

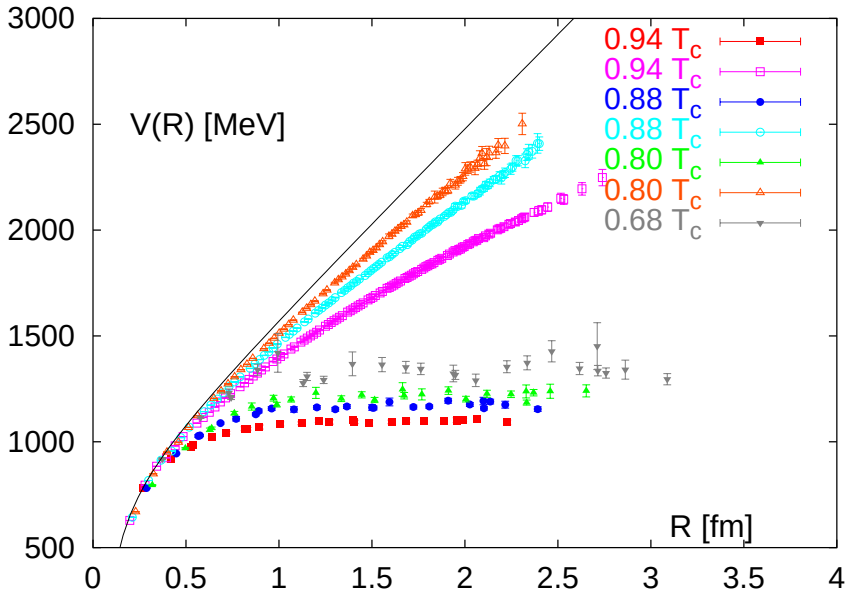

Figure 3.24: *Heavy quark potentials in physical units at various temperatures. Compared are quenched (open symbols) and full (filled symbols) QCD potentials at the same temperature. The dashed line is the zero temperature quenched potential. The data has been slightly shifted as to agree at distances around 0.3 fm.*

3.7 Heavy quark potentials at non-zero density

$N_\sigma^3 \times N_\tau$	B	n_B/T^3
$16^3 \times 4$	0	0.0000
$16^3 \times 4$	6	0.0313
$16^3 \times 4$	12	0.0625

Table 3.2: *Lattice sizes and densities of the simulations.*

The heavy quark potentials at non-zero baryon number density were calculated using the canonical partition function (3.1) where we have used the standard Wilson gauge action for S_G. The correlation functions were calculated on $16^3 \times 4$ lattices for different densities as shown in table (3.7) and various β-values. The errors on the potentials were determined by a jackknife analysis with 10 jackknife blocks and the sign problem has been taken into account by using the reweighting formula (3.3).

3.7.1 Results below T_c

The results for the potentials below the critical temperature T_c are shown in figure 3.26. For comparison figure 3.25 shows the heavy quark potentials on the $16^3 \times 4$ lattice at vanishing density. They show a worse rotational symmetry, but a qualitatively same behaviour as the results in figure 3.17. As we have seen in figure 3.6, the expectation value

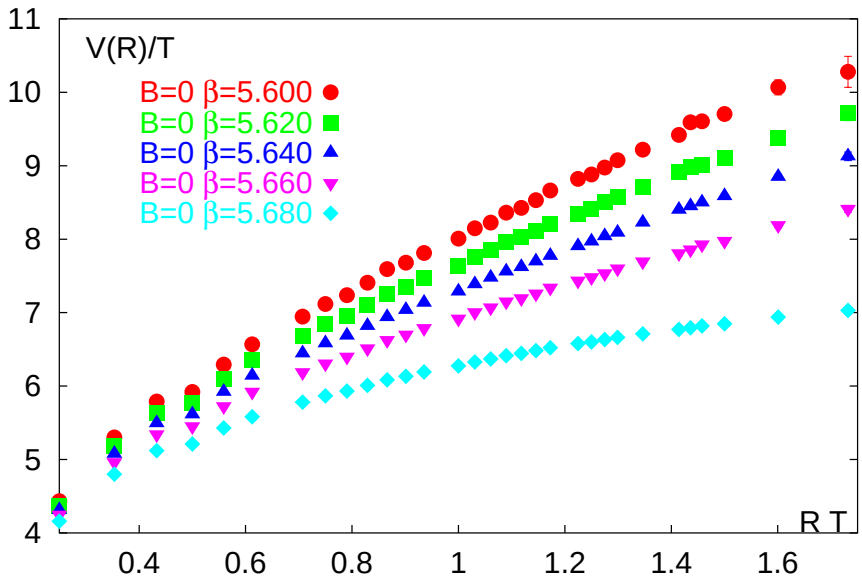

Figure 3.25: *Heavy quark potentials below T_c for vanishing density on $16^3 \times 4$ lattices.*

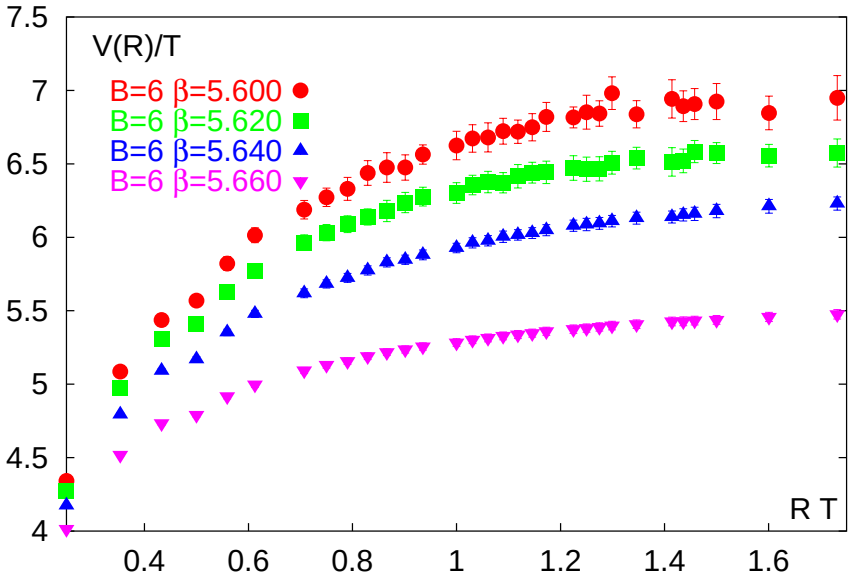

Figure 3.26: *Heavy quark potentials below T_c for $B = 6$ and different β-values on $16^3 \times 4$ lattices.*

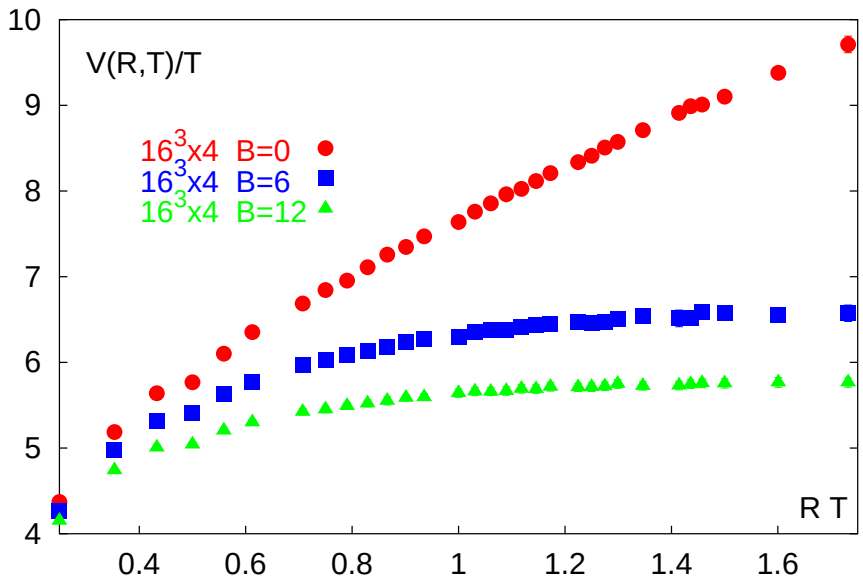

Figure 3.27: *Heavy quark potentials below T_c for $\beta = 5.620$ and different densities on $16^3 \times 4$ lattices.*

of the Polyakov loop stays non-zero for finite baryon number density even for temperatures below the phase transition. In the limit of infinite separation the potential can be expressed in terms of the Polyakov loop expectation value (2.16). Therefore we expect that the potential stays constant at large separations for $n_B/T^3 > 0$. In figure 3.26 we see exactly this behaviour. For small separations the usual (quenched) behaviour can be identified and is comparable to the potentials in figures 3.17 and 3.25. For larger distances the potential gets screened and stays constant in the limit of infinite separations. This modification of the long distance part of the heavy quark potential can be explained by the non-zero density of heavy quarks on the lattice. The static quark anti-quark source used to probe the potential can recombine with the already present static quarks on the lattice, forming a baryon and a meson, and therefore the potential gets screened. In figure 3.27 the potentials for $\beta = 5.620$ and the densities described in table (3.7) are shown. With increasing quark number density the screening of the heavy quark potential is increased and the plateau where the potential stays constant gets smaller.
Although the mechanism which leads to a breaking of the string is different for the quenched case at non-zero density compared to the full QCD case discussed in section 3.6, the heavy quark potentials show a quite similar behaviour. For small separations they are comparable with the quenched case, while at some distance R the string breaks and the potential stays constant for large separations. While in the full QCD case a quark anti-quark pair has to be created out of the vacuum to break the string, in the case of non-zero density the quarks are already present and at large separation it is energetically favourable that the string breaks.

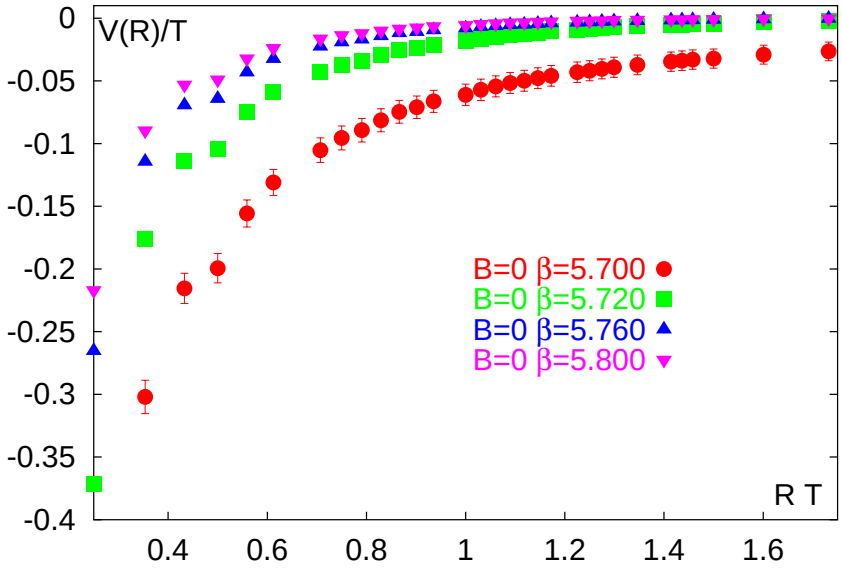

Figure 3.28: *Heavy quark potentials above T_c for vanishing density on $16^3 \times 4$ lattices.*

3.7.2 Results above T_c

The heavy quark potentials for temperatures above the critical temperature were normalized to their cluster value according to eq. (3.15) to eliminate the self-energy contributions. The potentials for vanishing quark number density (figure 3.28) show the screened Coulomb potential behaviour described by eq. (2.19) with some power d of the Coulomb part and screening masses μ comparable to figure 3.21. The potentials for different values of the quark number density but identical value of the coupling, $\beta = 5.720$, and therefore at identical temperature,are plotted in figure 3.29. At non-zero density the general form of the potential does not change, but the screening masses seem to increase with increasing density. This can be expected, because the already present quarks on the lattice lead to an additional screening of the quark anti-quark sources that probe the heavy quark potential. In figure 3.29 the potentials are plotted logarithmically. Due to the form of the potential (2.19), the screening masses are given by the gradient of the potential for large separations, while the slope for small separations is influenced by the Coulomb part.
Due to the bad rotational symmetry and the small volume, fits to the heavy quark potentials are limited to the ansatz

$$\frac{V(R,T)}{T} = -\frac{e(T)}{(RT)^d} e^{-\mu(T)R} \tag{3.17}$$

with a fixed d. As we have seen in figure 3.20, the exponent d is compatible with a value of 1.5 for temperatures slightly above T_c. Therefore to analyze the screening mass for the potentials at non-zero density, we fix d to 1.5 and use the fit-ansatz (3.17) with only two free parameters $e(T)$ and $\mu(T)$. For comparison we use the zero density potentials from

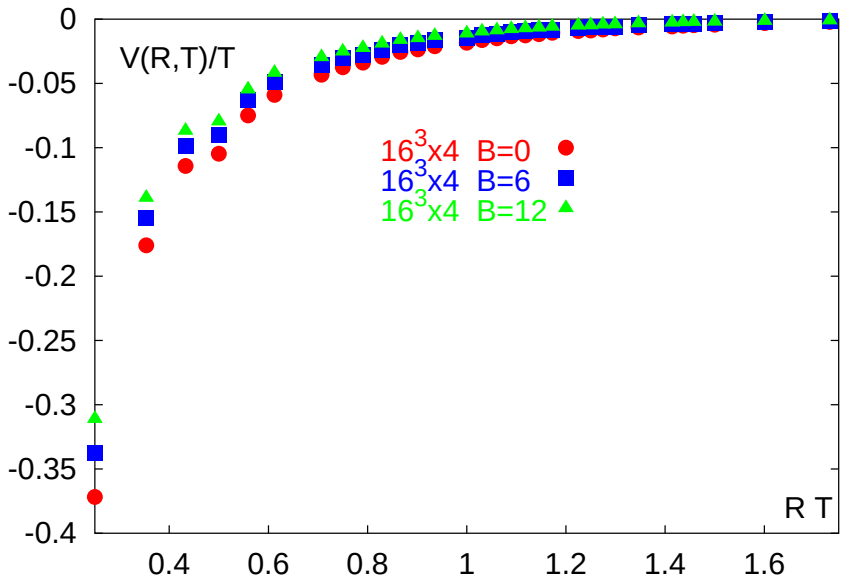

Figure 3.29: *Heavy quark potentials above T_c for $\beta = 5.720$ and different densities on $16^3 \times 4$ lattices.*

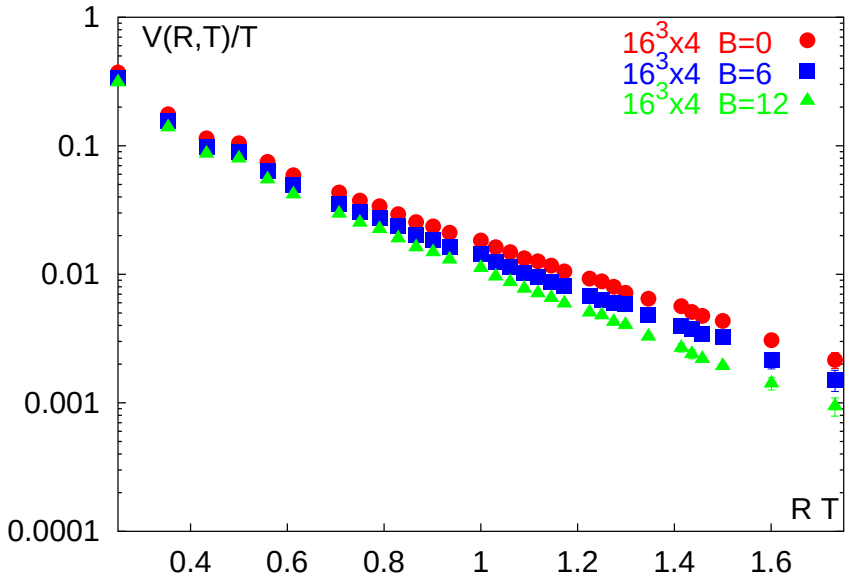

Figure 3.30: *Logarithmic plot of the heavy quark potentials above T_c for $\beta = 5.720$ and different densities on $16^3 \times 4$ lattices.*

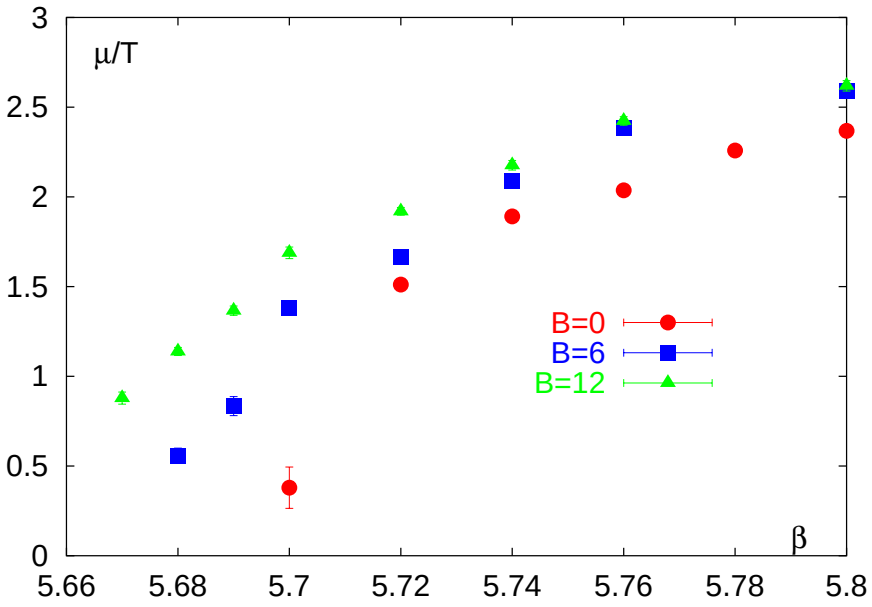

Figure 3.31: *Screening masses $\mu(T)/T$ for different densities extracted from the fit-ansatz (3.17) with $d = 1.5$.*

figure 3.28 as the systematic errors are comparable, rather than the ones from figure 3.19. Because of the simple ansatz, this can only be considered as a first qualitative analysis. The results for the screening masses $\mu(T)/T$ are plotted in figure 3.31. The zero density results are comparable with the results in figure 3.21. The screening masses are large for large β-values and tend to a small but non-zero value near the critical coupling. With increasing quark number density, $\mu(T)/T$ increases for all couplings. At the critical coupling for $B = 0$ the screening masses for $B \neq 0$ are still large and continue to decrease at smaller couplings. This shows again the shift of the phase transition towards smaller temperatures with increasing quark number density. Furthermore figure 3.31 shows that the non-zero density leads to an increasing screening due to the additional heavy quarks in the system. For a more detailed analysis of the heavy quark potential in the deconfined region, including a determination of the exponent d, larger volumes and improved actions are needed to reduce the systematic errors.

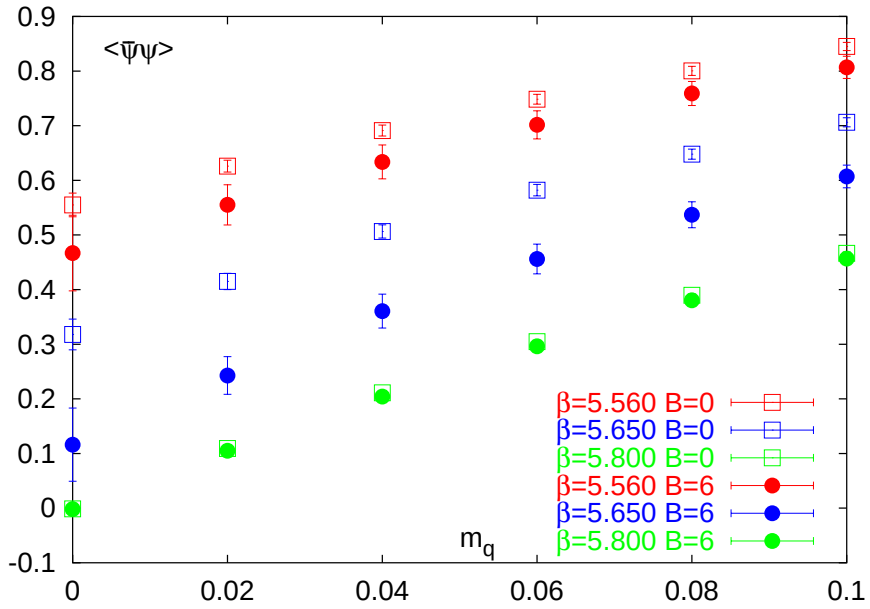

Figure 3.32: The chiral condensate for different β-values and various quark masses m_q together with the extrapolation to $m_q = 0$.

3.8 The chiral condensate

We have calculated the chiral condensate $\langle\bar{\psi}\psi\rangle$ using equation (2.48) on quenched configurations obtained from the partition function (3.4) for quark numbers of $B = 0$, 3, 6 and 9. The expectation values were calculated according to the reweighting method (3.3). We used two flavours of staggered fermions in the standard discretization with various quark masses from 0.02 to 0.1.

The Z(3)-dependence of the chiral condensate was discussed in section 2.4. As the integrand of the partition function (3.4) is Z(3)-symmetric, configurations that are connected by the Z(3)-symmetry are equally probable. Therefore we have used a Z(3) transformation on each configuration to calculate $\langle\bar{\psi}\psi\rangle$ in each of the 3 sectors and analyzed the averaged chiral condensate as well as the one in the real sector.

The results for the chiral condensate in the real sector for three β-values is plotted in figure 3.32 together with the linear extrapolation to $m_q = 0$. We see that $\langle\bar{\psi}\psi\rangle(m_q)$ extrapolates to a non-zero value for the small couplings, while for $\beta = 5.800$ the chiral condensate gets zero in the limit $m_q \to 0$. For the largest coupling, the $B = 0$ and $B = 6$ values coincide. The difference between them is largest for $\beta = 5.650$ and gets smaller again for the smallest coupling.

In figures 3.33 and 3.34 the extrapolated values $\langle\bar{\psi}\psi\rangle(m_q = 0)$ for the sector-averaged chiral condensate as well as for the one in the real sector are plotted. Both show a similar behaviour. In the deconfined phase, the $B = 0$ and $B = 6$ results agree. The non-zero density results tend to smaller values already for smaller couplings and the difference be-

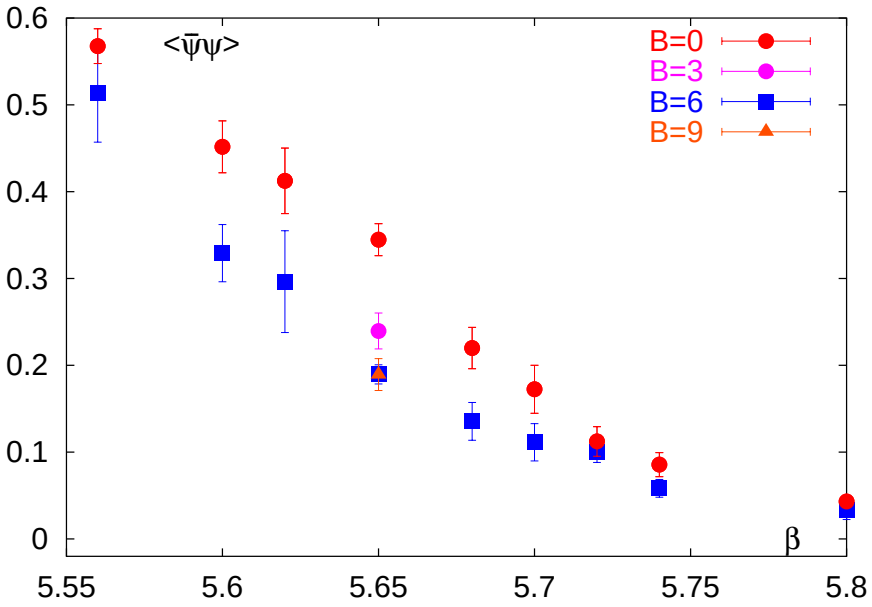

Figure 3.33: The $m_q = 0$ extrapolation of the chiral condensate averaged over all three Z(3) sectors.

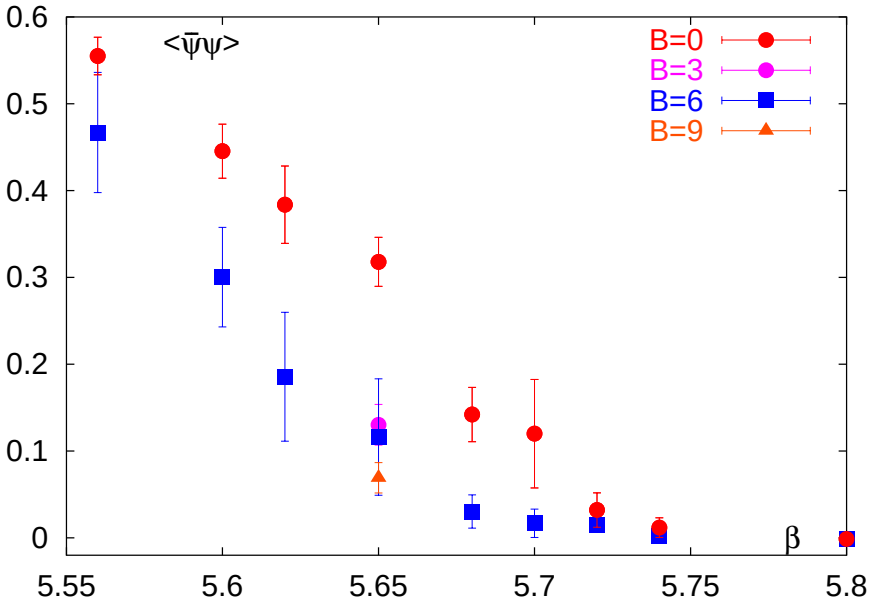

Figure 3.34: The $m_q = 0$ extrapolation of the chiral condensate in the real Z(3) sector.

tween the zero and non-zero density values seem to be largest in the transition region. For smaller values of β they seem to get together again.
The chiral condensates in figures 3.33 and 3.34 mainly differ in the vicinity and above the phase transition. For the smallest coupling they agree within errors. While the chiral condensate calculated in only the real sector extrapolates to zero for $\beta = 5.80$ for both densities, it stays non-zero for the sector-averaged condensate. The behaviour for the quenched chiral condensate for vanishing density in [73, 74] suggests that for larger couplings both methods should give the same result. Therefore we expect that also the averaged condensate extrapolates to zero for larger β-values.

Chapter 4

The quenched limit in the grand canonical approach

In this chapter we discuss the results obtained for the grand canonical approach of lattice QCD in the quenched limit. After describing the details of the simulation and a discussion of the sign problem at non-zero chemical potential we analyze the temperature dependence of bulk thermodynamics, the Polyakov loop expectation value and its susceptibility as well as baryon number density. All results are compared with the results of the canonical approach discussed in the previous chapter. We will also discuss the possibility of a critical endpoint of the first order phase transition and analyze its properties.

4.1 Details of the simulation

The simulations for the grand canonical approach in the limit of static quarks, i.e. the limit $\mu \to \infty$ and $\kappa \to 0$, keeping κe^{μ} fixed, were performed with the partition function

$$Z_{gc} = \int dU |\mathrm{Re}(\det(M))| e^{-S_G}, \tag{4.1}$$

where $\det(M)$ is the quenched limit of the fermion determinant in the Wilson formulation, as derived in section 1.9,

$$\begin{aligned} \det(M) &= \prod_{\vec{x}} \left(\det \left(P_{\vec{x}}^{\dagger} + C^{-1} \right) \right)^2 \\ &= \prod_{\vec{x}} \left(C^{-3} + C^{-2} \mathrm{Tr}\ P_{\vec{x}}^{\dagger} + C^{-1} \mathrm{Tr}\ P_{\vec{x}} + 1 \right)^2, \end{aligned} \tag{4.2}$$

with $C = (2\kappa e^{\mu a})^{-N_\tau}$. $P_{\vec{x}} = \prod_{x_4} U_4(\vec{x}, x_4)$ is the local Polyakov loop at the spatial point $\vec{x}$. S_G denotes the gluonic part of the action, for which we have used the standard Wilson

gauge action. The determinant (4.2) is a complex valued function of the Polyakov loops, but when integrating over all gauge fields in the grand canonical partition function (4.1), the imaginary parts of $\det(M)$ vanish. The sign problem that remains in this formulation can be handled by shifting the dependence on the sign into the observables and using a reweighting method [78] to calculate expectation values according to

$$\langle \mathcal{O} \rangle = \frac{\langle \mathcal{O} \cdot \mathrm{sgn}(\mathrm{Re} f_B) \rangle_{gc}}{\langle \mathrm{sgn}(\mathrm{Re} f_B) \rangle_{gc}}, \tag{4.3}$$

which is the same method used in the canonical calculations in the previous chapter. Our calculations were performed in the vicinity of the critical coupling on $16^3 \times 4$ lattices with $C = 0.0$, 0.0008, 0.001, 0.002, 0.005 and 0.01 using a combination of a Metropolis update and over-relaxation steps to reduce autocorrelations. Each sweep consists of one Metropolis and four over-relaxation steps. For each link update the change in $\mathrm{Re}(\det(M))$ is calculated and a possible change in sign is monitored. Measurements of the observables were performed after each sweep. The errors on observables were calculated using a Jackknife error analysis with 10 Jackknife-blocks. Interpolations were performed using the Ferrenberg-Swendsen method.

4.2 The sign problem

The average sign of the real part of the fermion determinant, $\mathrm{Re}(\det(M))$, is plotted in figure 4.2. The sign problem is small in the whole β-range for the values of the parameter C analyzed in our calculations. For $C = 0.0008$, 0.001 and 0.002, the average sign is one for nearly all couplings. Only near the phase transition it drops slightly towards smaller values. For larger values of C the sign problem gets stronger, but even for $C = 0.010$ the average sign is larger than 0.3.
If we look at the baryon number density in figure 4.11, we can see that the average sign mainly depends on the density rather than depending on the parameter C. For small values of C the density stays small in the whole β-range and the average sign is one for almost all couplings. For increasing C, the density n_B/T^3 increases even for small couplings and the sign problem gets stronger. Near the phase transition the rise of the density is strongest and the average sign has its minimum. Although the density is further increasing in the high temperature phase, the average sign gets larger again. This behaviour is similar to the sign problem in the canonical approach. For the densities analyzed there, we have seen no sign problem in the deconfined region. In the confined region, the average sign decreases with increasing baryon number density. The same behaviour can be seen here. Due to the strong increase of the density at the phase transition, the average sign is smallest near the critical coupling.
Figure 4.1 shows the distribution of the Polyakov loop spanned by $\mathrm{Re}(\mathrm{Tr}\ L)$ and $\mathrm{Im}(\mathrm{Tr}\ L)$ for $C = 0.001$ and 0.005 for different β-values on the $16^3 \times 4$ lattice. For the small value of C we see a similar behaviour to the quenched case (for comparison see figure 3.3). The sign is positive for all β-values. For small couplings the Polyakov loops are distributed symmetrically around the center of the complex plane indicating that the $Z(3)$ symmetry

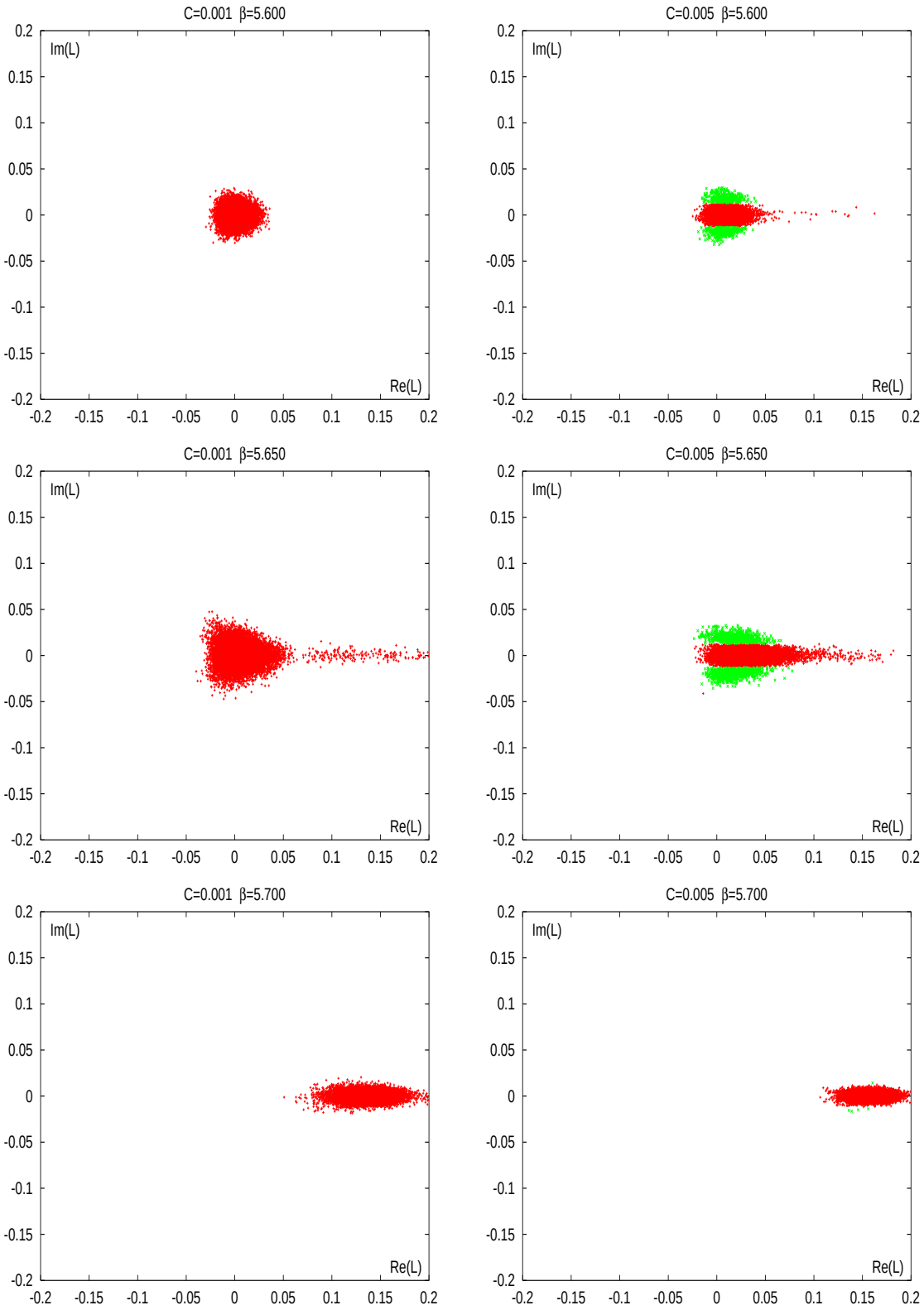

Figure 4.1: *Polyakov loop distributions in the complex plane spanned by* $\mathrm{Re}(\mathrm{Tr}L)$ *and* $\mathrm{Im}(\mathrm{Tr}L)$ *for* $C = 0.001$ *(left) and* $C = 0.005$ *(right) on* $16^3 \times 4$ *lattices and different* β*-values. Red points are Polyakov loops that give a positive* $\mathrm{Re}(\det(M))$ *and green points give a negative* $\mathrm{Re}(\det(M))$.

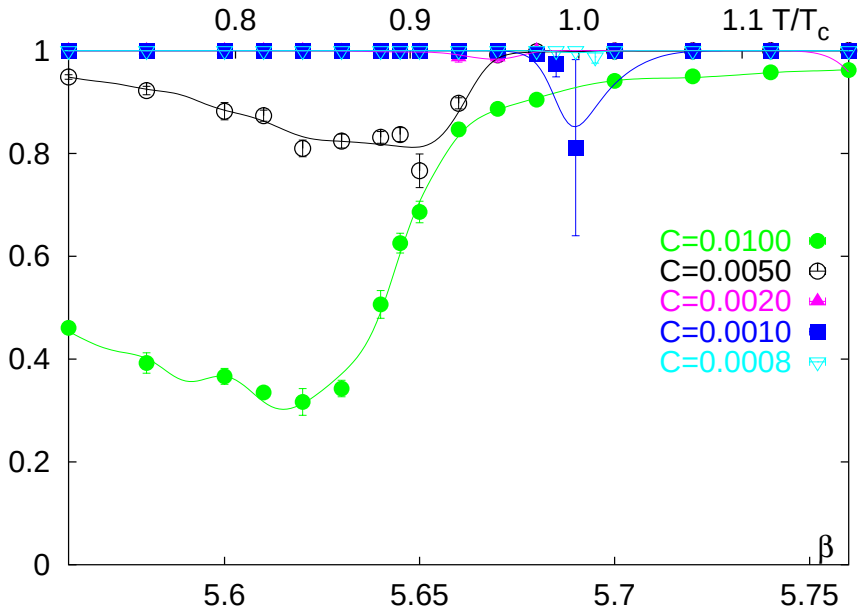

Figure 4.2: *Expectation value of the sign of* $\mathrm{Re}(\det(M))$ *on* $16^3 \times 4$ *lattices and different values of* C.

is only slightly broken by the small value of C. Increasing the coupling, and hence the temperature, the Polyakov loop values move towards the positive real axis. For $C = 0.005$ the Z(3) symmetry is disturbed for all couplings. Values in the positive real sector are favoured. This indicates an increasing breaking of the $Z(3)$ symmetry with increasing C. The Polyakov loops with a positive real part of $\det(M)$ are distributed in a band around the real axis and two additional sectors for the negative sign occur symmetrically around the real axis. Increasing the coupling, the distributions move towards larger values of the real part. In the deconfined region at $\beta = 5.700$, only the Polyakov loops with a positive real fermion determinant remain.

4.3 The confinement-deconfinement phase transition

In order to analyze the phase transition separating the confined and the deconfined phases, we have calculated expectation values of the Polyakov loop. In contrast to the canonical approach, observables show a discontinuous behaviour (in the infinite volume limit) at the critical coupling for a first order transition.
In figure 4.3 our results on $16^3 \times 4$ lattices with different values of the parameter C are shown. For small couplings, i.e. small temperatures, the Polyakov loop expectation values for different values of C seem to reach a similar value in the limit of small temperatures. In the infinite volume limit, this value should extrapolate to zero at small T. At some critical coupling we see a sharp rise of the Polyakov loop, which can be identified

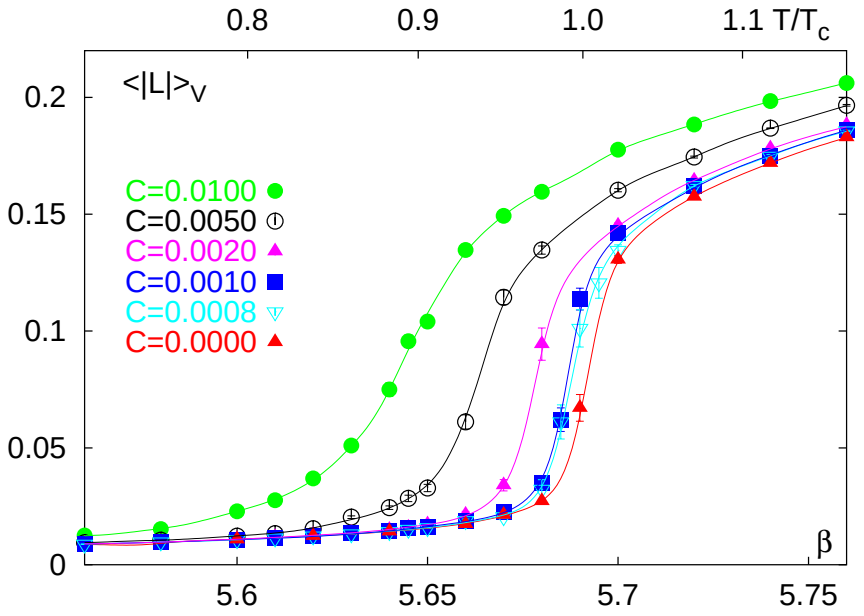

Figure 4.3: *Expectation value of the Polyakov loop on* $16^3 \times 4$ *lattices for different values of* C.

with the deconfinement phase transition. This pseudo critical couplings decreases with increasing C. Therefore the critical temperature T_c decreases with increasing parameter C as one would expect from the conjectured phase diagrams discussed in Chapter 1. For $C = 0.0008$ and 0.001 the gradient of the slope of the Polyakov loop at the critical temperature is comparable to the one at vanishing density ($C = 0.000$), which might indicate that the phase transition is still of first order for small values of the parameter C. The data for $C = 0.005$ and 0.010 show a weakening of this transition. The transition gets continuous indicating a crossover behaviour rather than a real phase transition. Therefore it seems that there exists a critical endpoint of the first order phase transition at some $C_c > 0$ in contrast to the arguments in [46] where a vanishing of the

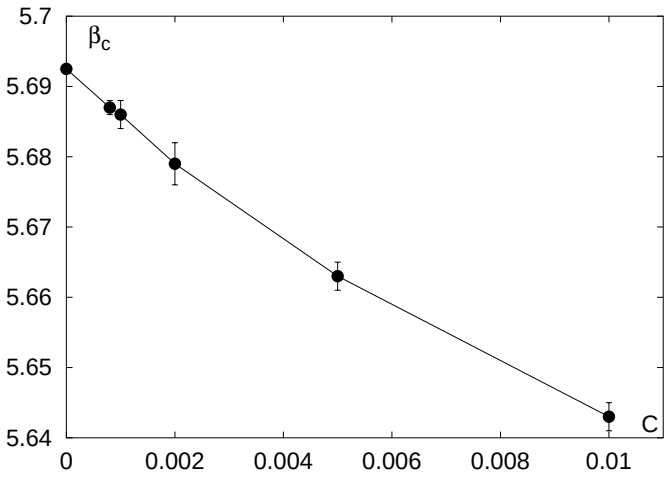

Figure 4.6: *The pseudo-critical couplings in the grand canonical approach, extracted from the peak positions of the Polyakov loop susceptibilities.*

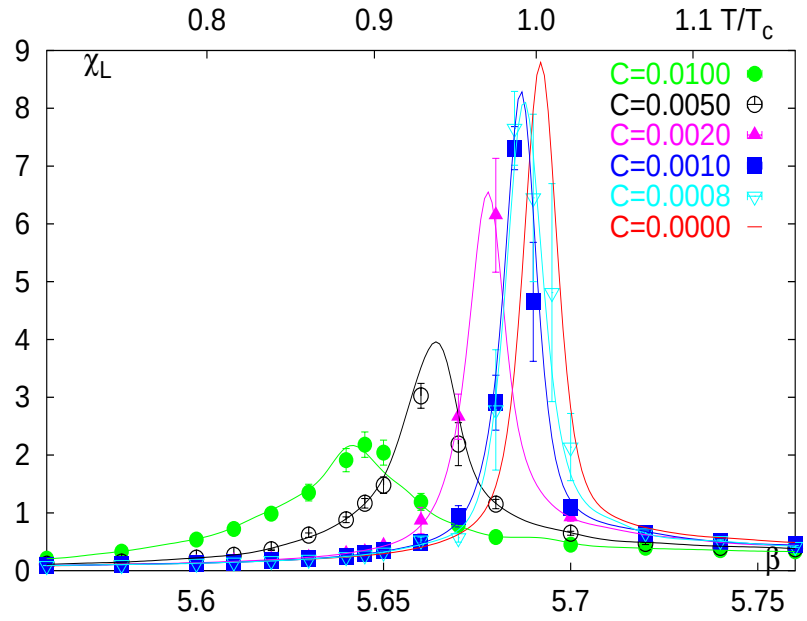

Figure 4.4: *Expectation value of the Polyakov loop susceptibility on* $16^3 \times 4$ *lattices for different values of* C.

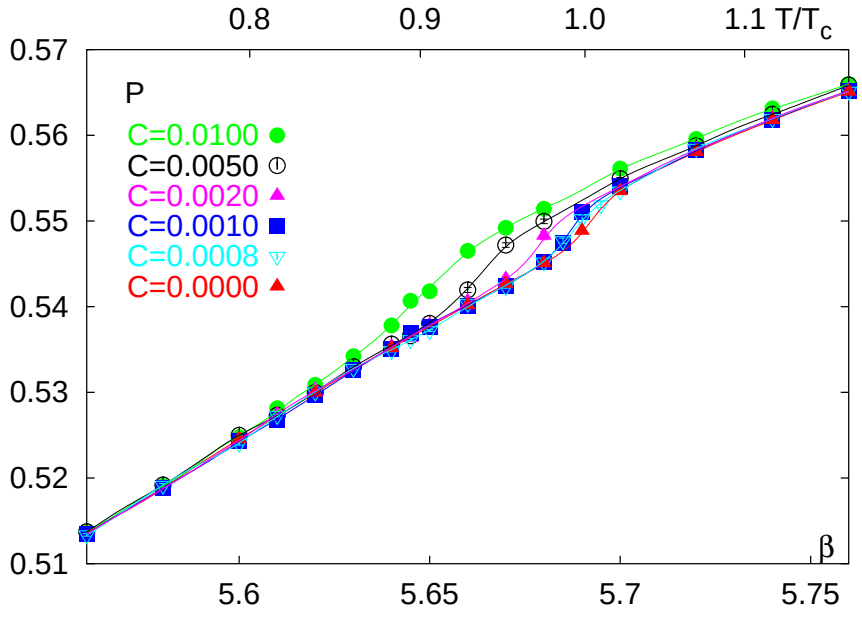

Figure 4.5: *Expectation value of the plaquette on* $16^3 \times 4$ *lattices for different values of* C.

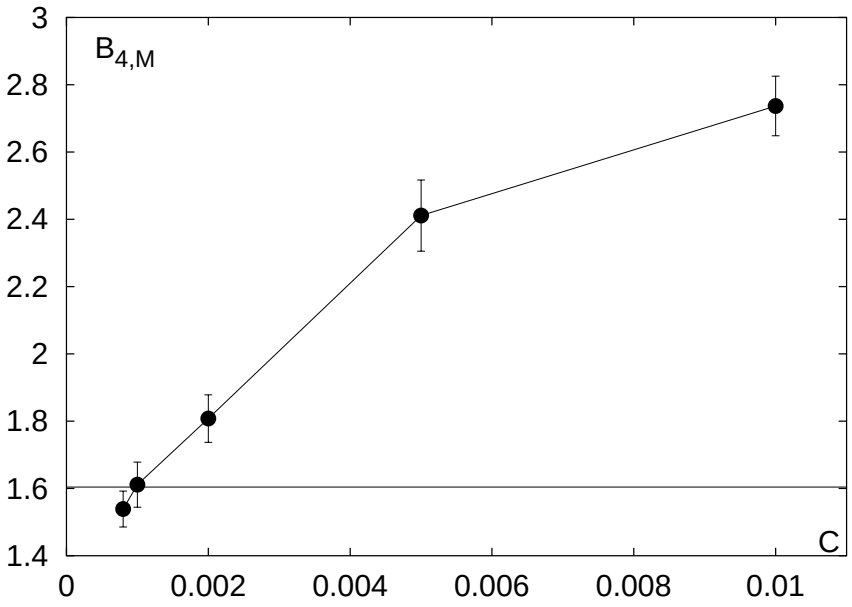

Figure 4.7: *The fourth Binder cumulant $B_{4,M}$ plotted against the parameter C. The solid line indicates the universal Ising value of 1.604(1).*

first order transition for any non-zero C was proposed. The authors of [46] argue that the behaviour of their data might be comparable to a simple function such as $\tanh(\frac{T-T_c}{h^x})$ which has a discontinuity for $h \to 0$ but a crossover at any non-zero h. We will see later that this argument is not supported by our calculations.
The susceptibility of the Polyakov loop is plotted in figure 4.4. We see the shift of the phase transition towards smaller values of the coupling, i.e. smaller temperatures, with increasing values of the parameter C as indicated by the Polyakov loop expectation values in figure 4.3. The pseudo-critical couplings, extracted from the position of the peak of the Polyakov loop susceptibility, are shown in table 4.4 and plotted in figure 4.6. We see again a similar behaviour for $C = 0.0008$, 0.001 and the zero density results. The peak height is slightly decreasing with increasing C but there is no broadening of the peak for this values. For the two largest values of C we see a broadening of the peak and a strong decrease of the peak height, which indicates the weakening of the phase transition. This behaviour of the Polyakov loop susceptibilities suggests again that the phase transition remains of first order for small values of C and that a critical endpoint might exist. In the following section we will discuss the evidence for such an endpoint in more detail.

4.4 The critical endpoint

From the data discussed in the previous section, one might suggest that the phase transition remains of first order for small values of C. The transition weakens with increasing

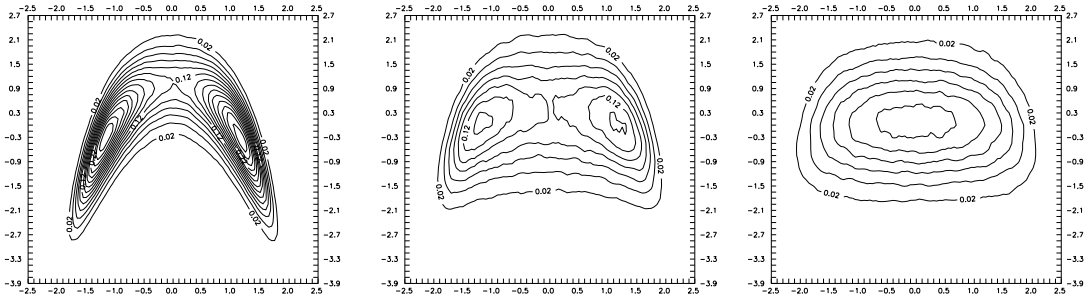

(a) Ising (b) $O(2)$ (c) $O(4)$

Figure 4.8: *The distribution of E- and M-like observables for different spin models at the critical point. The horizontal axis shows ΔM, the vertical axis ΔE.*

C and might end at second order critical point for some $C = C_c$. It is expected that this endpoint of the first order transition belongs to the universality class of the 3-d Ising model. For $C > C_c$, we expect to see a crossover.

To analyze the existence of such a critical point C_c we follow the ideas discussed for the Potts model [96], SU(2)-Higgs [97] and the liquid-gas phase transition [98, 99]. Due to the limited statistics on only one lattice size, an analysis of the volume dependence of the peak heights of the susceptibilities is not possible. The only criteria we can use at present are the Binder cumulants and joint histograms for the energy and Polyakov loop distributions. This can of course only give some qualitative characterization, whether the phase transition stays first order for small values of the parameter C, but no quantitative specification of the critical value C_c or the universality class of this endpoint.

C	β_c	$T_c(C)/T_c(0)$	$B_{4,M}$	$n_B(T_c)/T_c^3$
0.0008	5.687(1)	0.991(5)	1.539(53)	0.00742(45)
0.0010	5.686(2)	0.989(5)	1.611(67)	0.00933(70)
0.0020	5.679(3)	0.972(7)	1.808(71)	0.02135(81)
0.0050	5.663(2)	0.935(5)	2.411(106)	0.04951(133)
0.0100	5.643(2)	0.890(5)	2.737(88)	0.10900(164)

Table 4.1: *Pseudo-critical couplings, temperatures, fourth Binder cumulants and densities at the phase transition.*

We will now follow the method of decorrelating energy- and magnetic-like observables discussed for the Potts model in [96]. For QCD with heavy quarks the gluonic action takes the role of the energy and the Polyakov loop the one of the magnetisation of a spin system. Since the Polyakov loop for non-zero chemical potential is no longer an exact order-parameter one cannot expect to read off the same scaling properties at the critical endpoint as for the proper order parameter of a system in the same universality class. A non-zero field in a spin system, i.e. a non-zero chemical potential here, leads to a mixing of E-(energy) and M-(magnetisation) like observables. Therefore one defines new

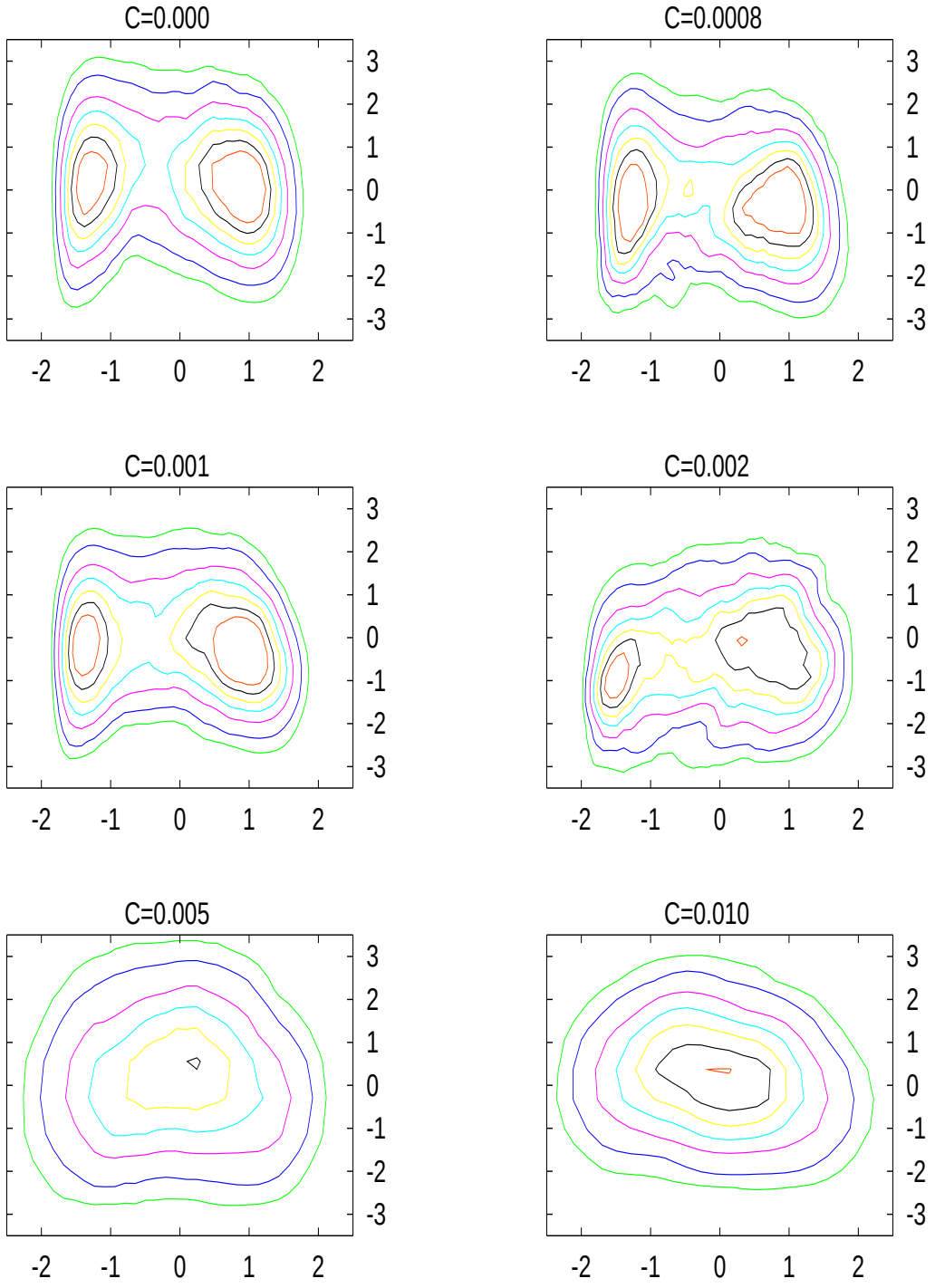

Figure 4.9: *The joint distributions for E- and M-like observables for different values of C.*

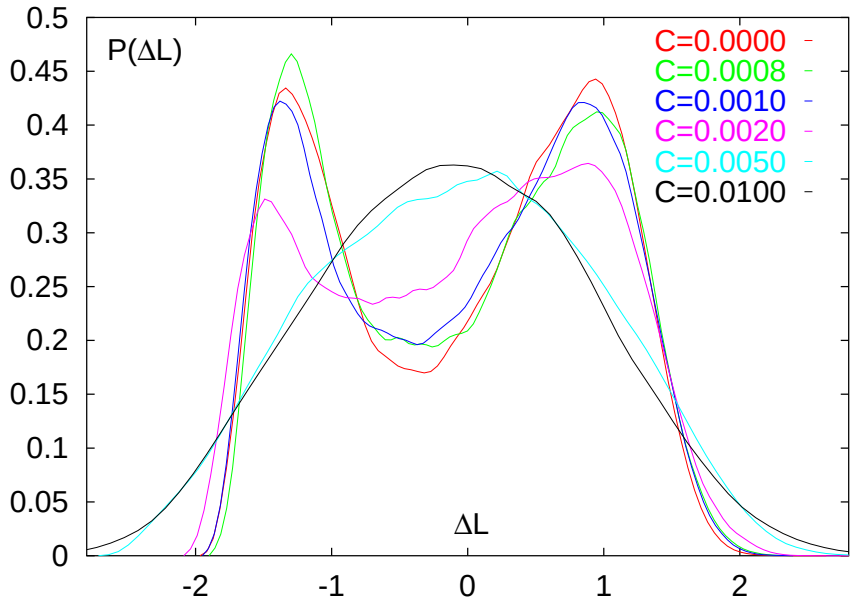

Figure 4.10: *The distribution of the M-like observable for different values of C.*

observables E and M which are the result of a coordinate transformation,

$$\begin{aligned} E &= A_{11} S_G + A_{12} L \\ M &= A_{21} S_G + A_{22} L, \end{aligned} \tag{4.4}$$

where A is the basis transformation matrix which diagonalizes the fluctuation matrix F in $E-M$ space. F is defined as

$$F = \begin{pmatrix} \langle (\Delta S_G)^2 \rangle & \langle (\Delta S_G)(\Delta L) \rangle \\ \langle (\Delta S_G)(\Delta L) \rangle & \langle (\Delta L)^2 \rangle \end{pmatrix}. \tag{4.5}$$

The new E- and M-like observables are now orthogonal in coupling space.
The third and fourth Binder cumulant of M are defined by

$$B_{3,M} = \frac{\langle (\Delta M)^3 \rangle}{\langle (\Delta M)^2 \rangle^{3/2}} \tag{4.6}$$

$$B_{4,M} = \frac{\langle (\Delta M)^4 \rangle}{\langle (\Delta M)^2 \rangle^2}, \tag{4.7}$$

with $\Delta \mathcal{O} \equiv \mathcal{O} - \langle \mathcal{O} \rangle$. The pseudo-critical couplings β_c at fixed C have been extracted from the peak position of the Polyakov loop susceptibilities in the previous section (see table 4.4). The probability distribution of the order parameter is symmetric at the pseudo-critical coupling. This is characterized by a vanishing of the third Binder cumulant, $B_{3,M} = 0$. The fourth Binder cumulant should be volume independent at the critical endpoint and therefore the values of $B_{4,M}$ for different volumes should intersect at a

universal value C_c. In [96] it was shown that for the Potts model, the critical external field is in very good agreement with the universal Ising value of 1.604(1). The universal values for $O(2)$ and $O(4)$ are 1.092(3) and 1.233(6). The results for the fourth Binder cumulant are shown in table 4.4. In figure 4.7 we see that the fourth Binder cumulant reaches the universal Ising value for a value of the parameter C around 0.001. This value might serve as a first indication for the critical point. Simulations on larger lattices are needed to see if the Binder cumulants intersect at this point.
The distribution of the M-like observable is plotted in figure 4.10. We see a clear double-peak structure up to $C = 0.001$, indicating the existence of a phase transition. For the large values of C, only one symmetric peak remains showing a crossover behaviour. This behaviour favors again a value of C_c around 0.001.
Finally we analyze the joint E- and M-like distributions. They are normalized such that $\langle(\Delta M)^2\rangle = 1$ and $\langle(\Delta E)^2\rangle = 1$. For the different universality classes discussed in connection with the Potts model and QCD, the Ising, O(4) and O(2) joint distributions at the critical endpoint are plotted in figure 4.8. The joint distributions of the rotated Polyakov loop M and the rotated action E are investigated on $16^3 \times 4$ lattices at the pseudo critical coupling. They are plotted in figure 4.9 for different values of C. The distributions for $C = 0.000$ and 0.0008 look quite similar indicating the first order nature of the transition. For $C = 0.001$ one finds a certain structure in the distribution which shows feature of the Ising or O(2) distribution shown in figure 4.8. The distribution for $C > 0.002$ look more like a crossover. The two largest values show a rotationally symmetric distribution which is a clear signal for a crossover. Therefore one might conclude that the transition is still of first order for small values of C and turns into a crossover at approximately $C \approx 0.001 - 0.002$. However, for the joint distributions the lattice volume and the statistics seems to be too small to determine an exact position of the critical endpoint. Simulations on larger lattices are needed to determine the location of the critical point and its universality class. We have seen that the methods used for the Potts model also seem to work for QCD at non-zero chemical potential.

4.5 The baryon number density

Unlike in the canonical approach, the baryon number density is an observable in the grand canonical approach. It can be calculated by the derivative of the logarithm of the partition function with respect to the chemical potential μ,

$$\frac{\langle n_B\rangle}{T^3} = \frac{1}{3T^3}\frac{1}{aN_\tau V}\frac{\partial \ln(Z)}{\partial \mu} \tag{4.8}$$

$$= \frac{2N_\tau^3}{3N_\sigma^3}\left\langle \sum_{\vec{x}} \frac{C^2 \mathrm{Tr}P_{\vec{x}} + 2C\mathrm{Tr}P_{\vec{x}}^\dagger + 3}{C^3 + C^2\mathrm{Tr}P_{\vec{x}} + C\mathrm{Tr}P_{\vec{x}}^\dagger + 1}\right\rangle \tag{4.9}$$

The results for n_B/T^3 are shown in figure 4.11 and figure 4.12. Below the critical temperature the density is small. It shows a strong increase at the phase transition and turns to large values in the deconfined phase. With increasing value of the parameter C, the baryon number density rises towards larger values. For the smallest values of C the slope of the

density at the critical coupling is very steep comparable to the behaviour of the Polyakov loop expectation values in figure 4.3. This indicates again that the phase transition is of first order for small values of C. The densities at the pseudo-critical couplings are shown in table 4.4.
All baryon number densities which we have analyzed in the canonical approach seem to be in the crossover region, rather than in the region of first order phase transition. Therefore it is not surprising that we have found no clear signals for a region of coexisting phases in the canonical approach. The broadening of the phase transition region might also be explained by a cross-over behaviour. Simulations for even smaller densities in the canonical approach have to be performed to see signals for a region of coexisting phases.

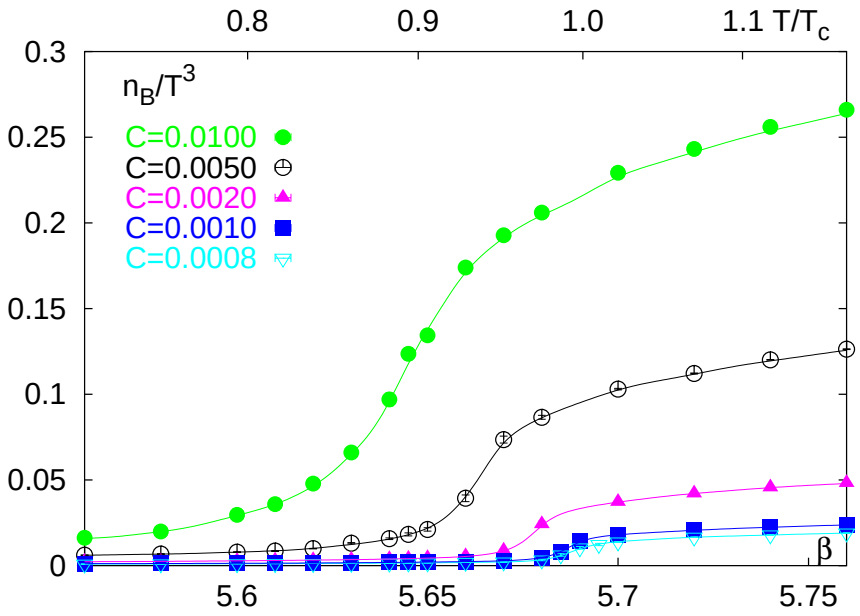

Figure 4.11: *The baryon number density normalized by the temperature cubed for different values of C.*

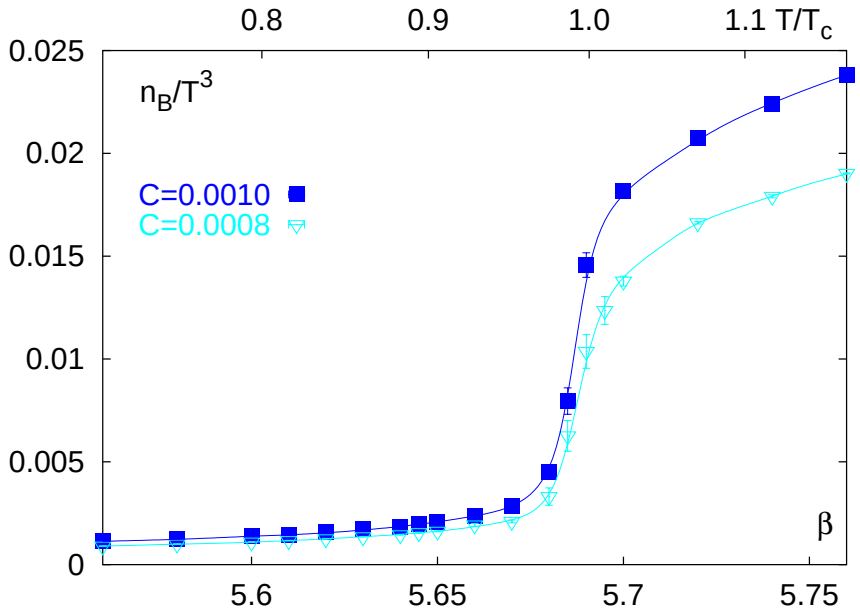

Figure 4.12: *The baryon number density normalized by the temperature cubed for small values of C.*

Conclusions

In this work we discussed the quenched limit of lattice QCD in the canonical and grand canonical approach. For the grand canonical approach we derived a closed expression of the partition function in terms of local Polyakov loops. From this expression we obtained a simple recurrence relation for the canonical partition functions, which allows a faster calculation of f_B for all B in our simulations in contrast to our earlier formulation which was limited to small values of the quark number B. Although a sign problem remains in both approaches, we have seen that it can be handled quite well in the vicinity and above the deconfinement transition for the densities and lattice volumes we have analyzed.
The results for the canonical approach show the expected behaviour. We see a broadening of the transition region with increasing quark number densities and a shift of the transition region towards smaller temperatures. Whether the broadening can be interpreted as a sign for a region of coexisting phases, as expected if the phase transition would be of first order, can not be answered up to now. We have analyzed the heavy quark potentials for the quenched case at zero and non-zero density, as well as for full QCD at zero density and compared all results. The quenched potentials at non-zero density show a qualitatively similar behaviour to the potentials obtained from the theory with dynamical quarks. Below the deconfinement transition, they show a flattening at large separations, which can be interpreted as a screening of the test quarks by the quarks already present in the system due to the non-zero quark density. This is comparable to string breaking in the full theory, although the mechanism is different. Above the transition, the screening masses increase with increasing density, again due to an additional contribution from static quarks.
The results for the grand canonical approach again show a shift of the phase transition towards smaller temperatures with increasing chemical potential, but no broadening of the transition region. The phase transition stays first order for small values of the chemical potential, but weakens with increasing chemical potential. The first order transition line ends at a second order critical point. The existence of this point has been established. However, because of the limited statistics on only one lattice volume, only a crude estimate for the position of this point at $C = 0.001$ could be given. For larger chemical potentials a crossover can be identified. Higher statistics and larger lattices are needed to determine the position and the universality class of the critical point in greater detail.
The quark densities used in the canonical approach were larger than the densities at the second order endpoint determined in the grand canonical approach. A region of coexisting phases in the parameter space analyzed in the canonical case may thus be ruled out. Calculations in the canonical approach for baryon number densities in the region

of the first order transition, i.e. at even smaller densities, are needed to observe signals for a region of coexisting phases. Larger lattices might improve the signatures for this coexistence, but will also lead to a more severe sign problem. Therefore the formulation and algorithms have to be improved to handle, or even remove, the sign problem also for larger lattice volumes.
With this work we intended to explore a new starting point for a non-perturbative analysis of QCD at finite density on the lattice. Within the static approximation we could establish many of the basic changes in the thermodynamic behaviour of QCD that are expected to occur in the presence of a non-vanishing baryon number density. The screening of the heavy quark potential and the reduction of chiral symmetry breaking are the most striking effects. The next step will be to allow for large, but finite quark masses, which will include also the propagation of the quarks in spatial direction. As the sign problem will be enhanced in this case, new algorithms or different formulations of the theory need to be developed. Further effort in this field will hopefully lead to a better understanding of the physics of strongly interacting matter as it will be created in experiments, existed in the early universe and might exist in the cores of compact stars.

Appendix A

Tables of the results

	$\beta = 5.60$	$B = 0$	$\beta = 5.62$	$B = 0$	$\beta = 5.64$	$B = 0$
R	$V(R)/T$	$\Delta V(R)/T$	$V(R)/T$	$\Delta V(R)/T$	$V(R)/T$	$\Delta V(R)/T$
0.0000000	2.195177e+00	5.612769e-05	2.194599e+00	8.231983e-05	2.193657e+00	1.164036e-04
1.0000000	4.432303e+00	8.958306e-04	4.370289e+00	7.567707e-04	4.310837e+00	7.758643e-04
1.4142136	5.300304e+00	1.521423e-03	5.186653e+00	1.526772e-03	5.076937e+00	1.418957e-03
1.7320508	5.789670e+00	2.746433e-03	5.639329e+00	2.350014e-03	5.494327e+00	2.588450e-03
2.0000000	5.919454e+00	2.726625e-03	5.767279e+00	2.618553e-03	5.613743e+00	2.183170e-03
2.2360680	6.292921e+00	3.535159e-03	6.101783e+00	2.838497e-03	5.921304e+00	2.386581e-03
2.4494897	6.568696e+00	4.484024e-03	6.352648e+00	2.596333e-03	6.141727e+00	3.581328e-03
2.8284271	6.945009e+00	5.564562e-03	6.686751e+00	3.041290e-03	6.444404e+00	4.891201e-03
3.0000000	7.117338e+00	4.643774e-03	6.844000e+00	3.061188e-03	6.582144e+00	5.069087e-03
3.1622777	7.238188e+00	7.128702e-03	6.954427e+00	5.965821e-03	6.686198e+00	5.211735e-03
3.3166248	7.406921e+00	7.390522e-03	7.110628e+00	7.548632e-03	6.818610e+00	5.667071e-03
3.4641016	7.592849e+00	9.644043e-03	7.257062e+00	6.576258e-03	6.939508e+00	6.567053e-03
3.6055513	7.680067e+00	6.552145e-03	7.347165e+00	9.097664e-03	7.036318e+00	8.547489e-03
3.7416574	7.813110e+00	7.955387e-03	7.470380e+00	8.494131e-03	7.134693e+00	6.853326e-03
4.0000000	8.007337e+00	1.183027e-02	7.638400e+00	1.223507e-02	7.286591e+00	9.207411e-03
4.1231056	8.148617e+00	1.094161e-02	7.758891e+00	7.991322e-03	7.387162e+00	7.798008e-03
4.2426407	8.226413e+00	1.323237e-02	7.856004e+00	1.304368e-02	7.476459e+00	9.732352e-03
4.3588989	8.361504e+00	1.185326e-02	7.961342e+00	9.123402e-03	7.559676e+00	1.060322e-02
4.4721360	8.427064e+00	1.246277e-02	8.025661e+00	1.157299e-02	7.620399e+00	8.883656e-03
4.5825757	8.531490e+00	1.505315e-02	8.115779e+00	1.259854e-02	7.696534e+00	9.771756e-03
4.6904158	8.663607e+00	1.913807e-02	8.208289e+00	1.117710e-02	7.772624e+00	9.115422e-03
4.8989795	8.820651e+00	1.499406e-02	8.336488e+00	1.547657e-02	7.905704e+00	1.181230e-02
5.0000000	8.880800e+00	1.990825e-02	8.412158e+00	1.541681e-02	7.968664e+00	1.184405e-02
5.0990195	8.975107e+00	2.179816e-02	8.507358e+00	1.820454e-02	8.040757e+00	1.256687e-02
5.1961524	9.074920e+00	4.032937e-02	8.573304e+00	1.696064e-02	8.089269e+00	1.305162e-02
5.3851648	9.219449e+00	1.816967e-02	8.709725e+00	2.183369e-02	8.226222e+00	1.957426e-02
5.6568542	9.419900e+00	5.081252e-02	8.912274e+00	3.177950e-02	8.400381e+00	2.579924e-02
5.7445626	9.591221e+00	3.917818e-02	8.989616e+00	2.515498e-02	8.448818e+00	2.326003e-02
5.8309519	9.605271e+00	3.798434e-02	9.009316e+00	3.601300e-02	8.499660e+00	2.302885e-02
6.0000000	9.704383e+00	4.697385e-02	9.101601e+00	3.856917e-02	8.585431e+00	2.453378e-02
6.4031242	1.006758e+01	1.028668e-01	9.379549e+00	3.808192e-02	8.849348e+00	3.471759e-02
6.9282032	1.027985e+01	2.110401e-01	9.710735e+00	9.666858e-02	9.127452e+00	5.827713e-02
7.0000000	1.017875e+01	1.991746e-01	9.607003e+00	1.034219e-01	9.011232e+00	4.176885e-02
8.0000000	1.068467e+01	7.040868e-02	9.914415e+00	2.113406e-01	9.128650e+00	5.965334e-02

Table A.1: The heavy quark potentials for $B = 0$ (figure 3.25).

	$\beta = 5.66$	$B = 0$	$\beta = 5.68$	$B = 0$	$\beta = 5.60$	$B = 6$
R	$V(R)/T$	$\Delta V(R)/T$	$V(R)/T$	$\Delta V(R)/T$	$V(R)/T$	$\Delta V(R)/T$
0.0000	2.192093e+00	1.463824e-04	2.187407e+00	2.124049e-04	2.189309e+00	1.848690e-03
1.0000	4.248518e+00	1.313626e-03	4.159960e+00	1.908997e-03	4.341691e+00	1.191301e-02
1.4142	4.965017e+00	2.398089e-03	4.799412e+00	4.062993e-03	5.085961e+00	2.365677e-02
1.7320	5.343720e+00	3.756978e-03	5.120896e+00	5.732179e-03	5.436481e+00	4.024753e-02
2.0000	5.453846e+00	3.946189e-03	5.210577e+00	6.133714e-03	5.569226e+00	3.865565e-02
2.2360	5.725858e+00	4.670958e-03	5.428492e+00	7.793819e-03	5.821445e+00	4.749981e-02
2.4494	5.922896e+00	6.135797e-03	5.581695e+00	8.995278e-03	6.014012e+00	5.072183e-02
2.8284	6.189226e+00	7.798261e-03	5.780578e+00	1.161951e-02	6.188327e+00	6.303483e-02
3.0000	6.308142e+00	8.439360e-03	5.866399e+00	1.272150e-02	6.272407e+00	6.222171e-02
3.1622	6.399997e+00	8.105853e-03	5.931206e+00	1.364072e-02	6.329784e+00	7.812033e-02
3.3166	6.512949e+00	8.722369e-03	6.009849e+00	1.460781e-02	6.437798e+00	8.405653e-02
3.4641	6.627455e+00	1.093301e-02	6.084376e+00	1.555820e-02	6.475336e+00	1.011344e-01
3.6055	6.700295e+00	1.181394e-02	6.133100e+00	1.647286e-02	6.475413e+00	8.625004e-02
3.7416	6.788959e+00	1.180710e-02	6.192047e+00	1.752462e-02	6.563706e+00	6.547030e-02
4.0000	6.918046e+00	1.575112e-02	6.275205e+00	1.917228e-02	6.625047e+00	9.693986e-02
4.1231	7.005587e+00	1.515043e-02	6.328514e+00	2.006806e-02	6.672881e+00	9.359741e-02
4.2426	7.070548e+00	1.625915e-02	6.369246e+00	2.103500e-02	6.680095e+00	9.923598e-02
4.3588	7.152382e+00	1.653766e-02	6.413702e+00	2.189586e-02	6.722414e+00	8.805614e-02
4.4721	7.197069e+00	1.636643e-02	6.444787e+00	2.263997e-02	6.719153e+00	7.923854e-02
4.5825	7.260390e+00	1.976964e-02	6.481869e+00	2.325266e-02	6.749377e+00	9.267044e-02
4.6904	7.340721e+00	2.057044e-02	6.521900e+00	2.499226e-02	6.819791e+00	9.851563e-02
4.8989	7.437307e+00	2.128655e-02	6.579160e+00	2.574756e-02	6.816396e+00	7.130386e-02
5.0000	7.482835e+00	2.178571e-02	6.601542e+00	2.722543e-02	6.851878e+00	1.157425e-01
5.0990	7.536245e+00	2.521042e-02	6.633521e+00	2.806136e-02	6.842898e+00	8.663726e-02
5.1961	7.601146e+00	2.340587e-02	6.662079e+00	2.922988e-02	6.981169e+00	1.110530e-01
5.3851	7.697214e+00	2.781506e-02	6.710516e+00	2.957194e-02	6.837637e+00	9.290371e-02
5.6568	7.808134e+00	3.350697e-02	6.771349e+00	3.292517e-02	6.942538e+00	1.305804e-01
5.7445	7.860449e+00	2.842957e-02	6.793319e+00	3.222945e-02	6.892614e+00	1.049684e-01
5.8309	7.928702e+00	3.087645e-02	6.818589e+00	3.375375e-02	6.907084e+00	1.052762e-01
6.0000	7.977161e+00	3.124491e-02	6.848148e+00	3.398539e-02	6.924625e+00	1.227445e-01
6.4031	8.190880e+00	3.614668e-02	6.938800e+00	3.684048e-02	6.846521e+00	1.144498e-01
6.9282	8.412977e+00	4.748189e-02	7.029597e+00	4.065465e-02	6.949595e+00	1.513076e-01
7.0000	8.242425e+00	2.831035e-02	6.943296e+00	3.917749e-02	6.942942e+00	1.330674e-01
8.0000	8.351243e+00	5.898439e-02	6.982273e+00	3.974387e-02	7.035027e+00	1.488300e-01

Table A.2: The heavy quark potentials for $B = 0$ (figure 3.25) and for $B = 6$ (figure 3.26).

	$\beta = 5.62$	$B = 6$	$\beta = 5.64$	$B = 6$	$\beta = 5.66$	$B = 6$
R	$V(R)/T$	$\Delta V(R)/T$	$V(R)/T$	$\Delta V(R)/T$	$V(R)/T$	$\Delta V(R)/T$
0.0000	2.185063e+00	2.000393e-03	2.180891e+00	5.234351e-04	2.168553e+00	7.552123e-04
1.0000	4.270493e+00	1.340515e-02	4.173900e+00	6.728703e-03	4.014567e+00	6.703244e-03
1.4142	4.972180e+00	2.792687e-02	4.793238e+00	1.342233e-02	4.518615e+00	1.136396e-02
1.7320	5.311102e+00	3.583744e-02	5.090891e+00	1.642152e-02	4.734736e+00	1.400662e-02
2.0000	5.412403e+00	4.285889e-02	5.168970e+00	1.800745e-02	4.791251e+00	1.574223e-02
2.2360	5.628230e+00	4.001598e-02	5.352424e+00	2.194579e-02	4.917574e+00	1.740976e-02
2.4494	5.774231e+00	4.532448e-02	5.478550e+00	2.472686e-02	4.997808e+00	1.869762e-02
2.8284	5.964151e+00	5.305668e-02	5.618762e+00	2.969644e-02	5.093525e+00	2.123892e-02
3.0000	6.031734e+00	5.552345e-02	5.682897e+00	2.793144e-02	5.131402e+00	2.183479e-02
3.1622	6.089494e+00	5.698220e-02	5.723806e+00	3.008018e-02	5.157155e+00	2.231420e-02
3.3166	6.138676e+00	5.524233e-02	5.774517e+00	3.124929e-02	5.190958e+00	2.316675e-02
3.4641	6.179300e+00	7.234018e-02	5.829563e+00	3.138978e-02	5.218445e+00	2.318101e-02
3.6055	6.236790e+00	6.876418e-02	5.847268e+00	3.128909e-02	5.236733e+00	2.427675e-02
3.7416	6.277096e+00	6.427620e-02	5.880364e+00	3.350257e-02	5.256687e+00	2.463196e-02
4.0000	6.301937e+00	7.029691e-02	5.927464e+00	3.222121e-02	5.283595e+00	2.642351e-02
4.1231	6.355856e+00	6.627639e-02	5.962529e+00	3.479155e-02	5.302400e+00	2.618516e-02
4.2426	6.376419e+00	7.299843e-02	5.976611e+00	3.491274e-02	5.314966e+00	2.655922e-02
4.3588	6.371549e+00	6.869121e-02	6.003886e+00	3.884352e-02	5.328641e+00	2.641834e-02
4.4721	6.415809e+00	7.957401e-02	6.016351e+00	3.563334e-02	5.338246e+00	2.703759e-02
4.5825	6.440151e+00	7.087263e-02	6.028660e+00	3.699339e-02	5.347962e+00	2.752603e-02
4.6904	6.442201e+00	7.631044e-02	6.048281e+00	3.779046e-02	5.360442e+00	2.779859e-02
4.8989	6.471790e+00	8.385661e-02	6.078837e+00	3.828000e-02	5.375004e+00	2.884088e-02
5.0000	6.463675e+00	8.246070e-02	6.087330e+00	4.209590e-02	5.382003e+00	2.829965e-02
5.0990	6.466264e+00	8.268516e-02	6.094859e+00	4.039584e-02	5.389396e+00	2.827280e-02
5.1961	6.507911e+00	7.804979e-02	6.109972e+00	3.905001e-02	5.398910e+00	2.914013e-02
5.3851	6.538867e+00	7.380982e-02	6.130554e+00	4.058806e-02	5.408657e+00	2.885964e-02
5.6568	6.513364e+00	9.665272e-02	6.137952e+00	4.078202e-02	5.427105e+00	2.964529e-02
5.7445	6.520614e+00	8.071642e-02	6.152595e+00	4.156607e-02	5.428721e+00	3.001215e-02
5.8309	6.583989e+00	7.533009e-02	6.159639e+00	4.510174e-02	5.433190e+00	2.960681e-02
6.0000	6.573891e+00	7.123660e-02	6.178893e+00	4.544871e-02	5.437674e+00	2.993584e-02
6.4031	6.555864e+00	7.656488e-02	6.211418e+00	4.674396e-02	5.458012e+00	3.105616e-02
6.9282	6.573772e+00	9.564884e-02	6.229918e+00	4.538604e-02	5.475927e+00	3.190125e-02
7.0000	6.620050e+00	7.058026e-02	6.204914e+00	4.548219e-02	5.455278e+00	3.022240e-02
8.0000	6.516197e+00	5.964754e-02	6.219687e+00	5.210504e-02	5.465245e+00	3.132139e-02

Table A.3: The heavy quark potentials for for $B = 6$ (figure 3.26).

	$\beta = 5.62$	$B = 12$	$\beta = 5.70$	$B = 0$	$\beta = 5.72$	$B = 0$
R	$V(R)/T$	$\Delta V(R)/T$	$V(R)/T$	$\Delta V(R)/T$	$V(R)/T$	$\Delta V(R)/T$
0.0000	2.174889e+00	1.786768e-03	2.102479e+00	1.375793e-03	2.067274e+00	5.794007e-04
1.0000	4.151868e+00	1.212239e-02	3.515387e+00	8.006737e-03	3.325114e+00	2.776710e-03
1.4142	4.740729e+00	1.886650e-02	3.769433e+00	1.094492e-02	3.520915e+00	3.527517e-03
1.7320	5.006136e+00	2.771484e-02	3.855979e+00	1.224341e-02	3.582707e+00	3.810987e-03
2.0000	5.041432e+00	3.416902e-02	3.872094e+00	1.264305e-02	3.592202e+00	4.019805e-03
2.2360	5.204744e+00	3.268742e-02	3.915722e+00	1.354122e-02	3.621959e+00	4.126671e-03
2.4494	5.299403e+00	3.332181e-02	3.940465e+00	1.398030e-02	3.637955e+00	4.218032e-03
2.8284	5.424132e+00	3.819674e-02	3.966253e+00	1.462502e-02	3.653640e+00	4.351842e-03
3.0000	5.450781e+00	3.893550e-02	3.975948e+00	1.482223e-02	3.659448e+00	4.375162e-03
3.1622	5.491342e+00	3.821001e-02	3.982166e+00	1.503501e-02	3.663076e+00	4.369933e-03
3.3166	5.520590e+00	4.027562e-02	3.990064e+00	1.525883e-02	3.667523e+00	4.379516e-03
3.4641	5.551007e+00	4.771933e-02	3.996766e+00	1.533822e-02	3.671397e+00	4.442417e-03
3.6055	5.586035e+00	3.652808e-02	4.000510e+00	1.551621e-02	3.673315e+00	4.472195e-03
3.7416	5.594449e+00	4.062776e-02	4.005171e+00	1.569521e-02	3.675816e+00	4.487869e-03
4.0000	5.640970e+00	4.825389e-02	4.010323e+00	1.593178e-02	3.678573e+00	4.534241e-03
4.1231	5.659960e+00	4.793728e-02	4.014367e+00	1.594450e-02	3.680627e+00	4.523145e-03
4.2426	5.657935e+00	4.581671e-02	4.017083e+00	1.608357e-02	3.682009e+00	4.539604e-03
4.3588	5.665996e+00	5.006986e-02	4.019746e+00	1.614707e-02	3.683568e+00	4.594032e-03
4.4721	5.691135e+00	5.052820e-02	4.021560e+00	1.617043e-02	3.684274e+00	4.603467e-03
4.5825	5.688117e+00	5.009762e-02	4.023651e+00	1.623380e-02	3.685203e+00	4.632685e-03
4.6904	5.714427e+00	5.001732e-02	4.025488e+00	1.627774e-02	3.686341e+00	4.585246e-03
4.8989	5.708902e+00	4.803483e-02	4.028439e+00	1.633968e-02	3.687621e+00	4.617785e-03
5.0000	5.711464e+00	5.095869e-02	4.029559e+00	1.651966e-02	3.688078e+00	4.672615e-03
5.0990	5.720935e+00	5.084517e-02	4.031051e+00	1.657921e-02	3.688890e+00	4.672057e-03
5.1961	5.748553e+00	5.176167e-02	4.032364e+00	1.647877e-02	3.689700e+00	4.669537e-03
5.3851	5.725260e+00	4.948882e-02	4.034246e+00	1.664421e-02	3.690425e+00	4.732998e-03
5.6568	5.729773e+00	5.016659e-02	4.036832e+00	1.686524e-02	3.691239e+00	4.688039e-03
5.7445	5.745346e+00	5.128821e-02	4.037610e+00	1.676136e-02	3.691786e+00	4.707041e-03
5.8309	5.757134e+00	5.226823e-02	4.038453e+00	1.679182e-02	3.692136e+00	4.770970e-03
6.0000	5.754666e+00	5.464586e-02	4.039263e+00	1.689352e-02	3.692548e+00	4.712432e-03
6.4031	5.766255e+00	5.771518e-02	4.042353e+00	1.703595e-02	3.693810e+00	4.771647e-03
6.9282	5.765644e+00	5.526662e-02	4.044993e+00	1.713512e-02	3.694729e+00	4.707500e-03
7.0000	5.770438e+00	5.307850e-02	4.042660e+00	1.699544e-02	3.693998e+00	4.886819e-03
8.0000	5.810096e+00	6.777742e-02	4.044030e+00	1.707018e-02	3.694656e+00	5.010235e-03

Table A.4: The heavy quark potentials for $B = 12$ (figure 3.27) and for $B = 0$ (figure 3.28).

	$\beta = 5.76$	$B = 0$	$\beta = 5.80$	$B = 0$
R	$V(R)/T$	$\Delta V(R)/T$	$V(R)/T$	$\Delta V(R)/T$
0.0000	2.025994e+00	2.615001e-04	1.994491e+00	1.649468e-04
1.0000	3.131752e+00	9.615212e-04	3.002675e+00	5.125201e-04
1.4142	3.282682e+00	1.216371e-03	3.130063e+00	6.309800e-04
1.7320	3.327747e+00	1.222089e-03	3.166579e+00	7.381844e-04
2.0000	3.332795e+00	1.242007e-03	3.170608e+00	6.824041e-04
2.2360	3.353909e+00	1.335470e-03	3.187439e+00	6.917528e-04
2.4494	3.364674e+00	1.364012e-03	3.195800e+00	6.850378e-04
2.8284	3.374567e+00	1.454883e-03	3.203316e+00	7.100104e-04
3.0000	3.377971e+00	1.385835e-03	3.206029e+00	7.597249e-04
3.1622	3.380153e+00	1.390379e-03	3.207644e+00	7.310503e-04
3.3166	3.382857e+00	1.397984e-03	3.209646e+00	7.327422e-04
3.4641	3.385323e+00	1.435145e-03	3.211110e+00	7.497913e-04
3.6055	3.386209e+00	1.426524e-03	3.212194e+00	7.392257e-04
3.7416	3.387606e+00	1.434689e-03	3.213125e+00	7.551264e-04
4.0000	3.388899e+00	1.443820e-03	3.214011e+00	7.072186e-04
4.1231	3.390254e+00	1.458714e-03	3.215005e+00	7.173487e-04
4.2426	3.390960e+00	1.422530e-03	3.215487e+00	7.414193e-04
4.3588	3.391706e+00	1.421350e-03	3.216050e+00	7.858652e-04
4.4721	3.392057e+00	1.454220e-03	3.216239e+00	7.368077e-04
4.5825	3.392618e+00	1.447068e-03	3.216632e+00	7.522747e-04
4.6904	3.393125e+00	1.456809e-03	3.217013e+00	7.026983e-04
4.8989	3.393660e+00	1.476892e-03	3.217428e+00	7.289175e-04
5.0000	3.393887e+00	1.456825e-03	3.217574e+00	7.552647e-04
5.0990	3.394330e+00	1.468405e-03	3.217819e+00	7.657799e-04
5.1961	3.394610e+00	1.563395e-03	3.218195e+00	7.905192e-04
5.3851	3.394916e+00	1.470273e-03	3.218275e+00	7.472364e-04
5.6568	3.395413e+00	1.466546e-03	3.218589e+00	7.658886e-04
5.7445	3.395575e+00	1.483088e-03	3.218628e+00	7.691572e-04
5.8309	3.395681e+00	1.454950e-03	3.218738e+00	7.716651e-04
6.0000	3.395887e+00	1.448406e-03	3.218877e+00	7.431228e-04
6.4031	3.396386e+00	1.480130e-03	3.219153e+00	7.456663e-04
6.9282	3.396742e+00	1.587837e-03	3.219360e+00	7.026771e-04
7.0000	3.396369e+00	1.512606e-03	3.219212e+00	7.499511e-04
8.0000	3.396326e+00	1.528490e-03	3.219362e+00	7.136117e-04

Table A.5: The heavy quark potentials for $B = 0$ (figure 3.28).

	$\beta = 5.72$	$B = 6$	$\beta = 5.72$	$B = 12$
R	$V(R)/T$	$\Delta V(R)/T$	$V(R)/T$	$\Delta V(R)/T$
0.0000	2.056227e+00	1.066575e-03	2.046831e+00	7.297964e-04
1.0000	3.275227e+00	5.330544e-03	3.234002e+00	3.233304e-03
1.4142	3.457849e+00	6.642578e-03	3.406031e+00	4.139833e-03
1.7320	3.514226e+00	7.240392e-03	3.458236e+00	4.472233e-03
2.0000	3.522383e+00	7.335437e-03	3.465479e+00	4.452191e-03
2.2360	3.549320e+00	7.640440e-03	3.490371e+00	4.639951e-03
2.4494	3.563474e+00	7.769065e-03	3.503258e+00	4.801604e-03
2.8284	3.577304e+00	8.016672e-03	3.515429e+00	4.871574e-03
3.0000	3.582122e+00	8.056253e-03	3.519890e+00	4.923406e-03
3.1622	3.584952e+00	8.101070e-03	3.522556e+00	4.957480e-03
3.3166	3.588874e+00	8.197244e-03	3.526040e+00	4.939227e-03
3.4641	3.592325e+00	8.315499e-03	3.528835e+00	5.087911e-03
3.6055	3.594004e+00	8.269568e-03	3.530210e+00	5.049079e-03
3.7416	3.596271e+00	8.337454e-03	3.532015e+00	5.035980e-03
4.0000	3.598070e+00	8.361358e-03	3.533846e+00	5.026880e-03
4.1231	3.600081e+00	8.453554e-03	3.535455e+00	5.102515e-03
4.2426	3.601136e+00	8.445150e-03	3.536362e+00	5.087299e-03
4.3588	3.602298e+00	8.519499e-03	3.537336e+00	5.108327e-03
4.4721	3.603039e+00	8.497166e-03	3.537944e+00	5.131576e-03
4.5825	3.603924e+00	8.548835e-03	3.538511e+00	5.124147e-03
4.6904	3.604405e+00	8.560225e-03	3.539133e+00	5.118428e-03
4.8989	3.605737e+00	8.663872e-03	3.540020e+00	5.163115e-03
5.0000	3.606216e+00	8.621757e-03	3.540255e+00	5.135794e-03
5.0990	3.606578e+00	8.625797e-03	3.540793e+00	5.171152e-03
5.1961	3.606718e+00	8.631576e-03	3.541019e+00	5.199189e-03
5.3851	3.607753e+00	8.613263e-03	3.541783e+00	5.154476e-03
5.6568	3.608597e+00	8.718842e-03	3.542373e+00	5.155268e-03
5.7445	3.608806e+00	8.706090e-03	3.542658e+00	5.122236e-03
5.8309	3.609135e+00	8.672547e-03	3.542859e+00	5.211814e-03
6.0000	3.609324e+00	8.690401e-03	3.543116e+00	5.203886e-03
6.4031	3.610413e+00	8.756339e-03	3.543640e+00	5.181260e-03
6.9282	3.611043e+00	8.669325e-03	3.544111e+00	5.220756e-03
7.0000	3.610421e+00	8.857434e-03	3.544239e+00	5.287036e-03
8.0000	3.610899e+00	8.870494e-03	3.544359e+00	5.398514e-03

Table A.6: The heavy quark potentials for $B = 6$ and 12 (figure 3.29).

	$B=0$		$B=6$		$B=12$	
β	$\mu(T)$	$\Delta\mu(T)$	$\mu(T)$	$\Delta\mu(T)$	$\mu(T)$	$\Delta\mu(T)$
5.67					0.219617	0.008407
5.68			0.139201	0.010757	0.284626	0.005647
5.69			0.208419	0.013241	0.341434	0.006480
5.70	0.094868	0.028810	0.344702	0.009650	0.422048	0.008116
5.72	0.377818	0.006431	0.416221	0.010024	0.479862	0.005350
5.74	0.472800	0.004651	0.522179	0.005757	0.543997	0.006678
5.76	0.509122	0.005149	0.596179	0.004902	0.605879	0.005992
5.78	0.564647	0.004683				
5.80	0.592046	0.004807	0.647424	0.009103	0.654775	0.007231

Table A.7: The screening masses $\mu(T)$ for $B = 0$, 6 and 12 (figure 3.31)

	$B=0$		$B=6$	
β	$\langle\psi\psi\rangle$	$\Delta\langle\psi\psi\rangle$	$\langle\psi\psi\rangle$	$\Delta\langle\psi\psi\rangle$
5.560	5.675975e-01	1.999751e-02	5.141182e-01	5.710701e-02
5.600	4.516934e-01	2.993775e-02	3.292075e-01	3.296467e-02
5.620	4.125112e-01	3.770406e-02	2.963828e-01	5.869031e-02
5.650	3.447211e-01	1.842360e-02	1.895866e-01	1.099939e-02
5.680	2.199510e-01	2.377878e-02	1.354169e-01	2.179290e-02
5.700	1.724013e-01	2.767812e-02	1.113506e-01	2.145039e-02
5.720	1.123391e-01	1.705682e-02	9.971245e-02	1.155948e-02
5.740	8.559863e-02	1.383918e-02	5.825762e-02	1.021383e-02
5.800	4.318381e-02	5.547616e-03	3.324330e-02	1.086050e-02
	$B=3$		$B=9$	
5.650	2.395582e-01	2.064072e-02	1.893213e-01	1.838337e-02

Table A.8: The chiral condensate for $B = 0$, 3, 6 and 9 (figure 3.33)

	$B=0$		$B=6$	
β	$\langle\psi\psi\rangle$	$\Delta\langle\psi\psi\rangle$	$\langle\psi\psi\rangle$	$\Delta\langle\psi\psi\rangle$
5.560	5.550248e-01	2.161521e-02	4.668751e-01	6.922858e-02
5.600	4.453723e-01	3.116627e-02	3.003278e-01	5.733124e-02
5.620	3.837429e-01	4.456664e-02	1.855921e-01	7.426015e-02
5.650	3.179101e-01	2.820616e-02	1.161515e-01	6.703597e-02
5.680	1.420890e-01	3.129058e-02	3.036821e-02	1.920882e-02
5.700	1.200041e-01	6.243432e-02	1.678132e-02	1.630390e-02
5.720	3.208167e-02	1.982048e-02	1.503684e-02	8.310794e-03
5.740	1.179322e-02	1.136064e-02	1.860205e-03	7.063125e-03
5.800	-1.227372e-03	3.884930e-03	-1.853167e-03	6.036416e-03
	$B=3$		$B=9$	
5.650	1.302718e-01	2.349215e-02	6.916529e-02	1.752395e-02

Table A.9: The chiral condensate for $B = 0$, 3, 6 and 9 (figure 3.34)

Bibliography

[1] J. Engels, O. Kaczmarek, F. Karsch, and E. Laermann, "The quenched limit of lattice QCD at non-zero baryon number", *Nucl. Phys.* **B558** (1999) 307.

[2] C. DeTar, O. Kaczmarek, F. Karsch, and E. Laermann, "String breaking in lattice quantum chromodynamics", *Phys. Rev.* **D59** (1999) 031501.

[3] O. Kaczmarek, F. Karsch, E. Laermann, and M. Lütgemeier, "Heavy quark potentials in quenched QCD at high temperature", *Phys. Rev.* **D62** (2000) 034021.

[4] E. Laermann, C. DeTar, O. Kaczmarek, and F. Karsch, "String breaking in lattice QCD", *Nucl. Phys. Proc. Suppl.* **73** (1999) 447. 16th International Symposium on Lattice Field Theory (LATTICE 98).

[5] C. DeTar, O. Kaczmarek, F. Karsch, and E. Laermann, "The heavy-quark potential in QCD at finite temperature". In Copenhagen 1998, Strong and electroweak matter.

[6] J. Engels, O. Kaczmarek, F. Karsch, and E. Laermann, "The non-zero baryon number formulation of QCD", *Nucl. Phys. Proc. Suppl.* **83** (2000) 369–371. 17th International Symposium on Lattice Field Theory (LATTICE 99).

[7] O. Kaczmarek, J. Engels, F. Karsch, and E. Laermann, "Lattice QCD at non-zero baryon number". In Trento 1999, Understanding deconfinement in QCD.

[8] H. J. Rothe, "Lattice gauge theories: An introduction". Singapore, Singapore: World Scientific (1992) 381 p.

[9] I. Montvay and G. Münster, "Quantum fields on a lattice". Cambridge, UK: Univ. Pr. (1994) 491 p. (Cambridge monographs on mathematical physics).

[10] H. Meyer-Ortmanns, "Phase transitions in quantum chromodynamics", *Rev. Mod. Phys.* **68** (1996) 473–598.

[11] M. Fukugita, M. Okawa, and A. Ukawa, "Finite size scaling study of the deconfining phase transition in pure SU(3) lattice gauge theory", *Nucl. Phys.* **B337** (1990) 181.

[12] A. Peikert, "QCD thermodynamics with 2+1 quark flavours in lattice simulations", *Ph.D. Thesis* **Bielefeld** (2000).

[13] R. D. Pisarski and F. Wilczek, "Remarks on the chiral phase transition in chromodynamics", *Phys. Rev.* **D29** (1984) 338–341.

[14] M. Lütgemeier, "Phasenübergänge in der QCD mit fundamentalen und adjungierten Quarks", *Ph.D. Thesis* **Bielefeld** (1998).

[15] M. A. Halasz, A. D. Jackson, R. E. Shrock, M. A. Stephanov, and J. J. M. Verbaarschot, "On the phase diagram of QCD", *Phys. Rev.* **D58** (1998) 096007.

[16] J. Pochodzalla *et al.*, "Probing the nuclear liquid - gas phase transition", *Phys. Rev. Lett.* **75** (1995) 1040.

[17] W. Trautmann, "Multifragmentation in relativistic heavy-ion reactions". In Dronten 1996, Correlations and clustering phenomena in subatomic physics, 115-135.

[18] M. Alford, "Color superconductivity in dense quark matter", `hep-ph/0003185`.

[19] P. Braun-Munzinger, "Towards the quark-gluon plasma", *Nucl. Phys.* **A663-664** (2000) 183.

[20] M. Alford, "New possibilities for QCD at finite density", *Nucl. Phys. Proc. Suppl.* **73** (1999) 161.

[21] D. Bailin and A. Love, "Superfluidity and superconductivity in relativistic fermion systems", *Phys. Rept.* **107** (1984) 325.

[22] J. Bardeen, L. N. Cooper, and J. R. Schrieffer, "Theory of superconductivity", *Phys. Rev.* **108** (1957) 1175–1204.

[23] R. Rapp, T. Schäfer, E. V. Shuryak, and M. Velkovsky, "Diquark bose condensates in high density matter and instantons", *Phys. Rev. Lett.* **81** (1998) 53–56.

[24] M. Alford, K. Rajagopal, and F. Wilczek, "QCD at finite baryon density: Nucleon droplets and color superconductivity", *Phys. Lett.* **B422** (1998) 247.

[25] M. Alford, K. Rajagopal, and F. Wilczek, "Color-flavor locking and chiral symmetry breaking in high density QCD", *Nucl. Phys.* **B537** (1999) 443.

[26] M. Stephanov, K. Rajagopal, and E. Shuryak, "Signatures of the tricritical point in QCD", *Phys. Rev. Lett.* **81** (1998) 4816–4819.

[27] J. Berges and K. Rajagopal, "Color superconductivity and chiral symmetry restoration at nonzero baryon density and temperature", *Nucl. Phys.* **B538** (1999) 215.

[28] O. Kiriyama, M. Maruyama, and F. Takagi, "Chiral phase transition at high temperature and density in the QCD-like theory", *Phys. Rev.* **D62** (2000) 105008.

[29] M. Stephanov, K. Rajagopal, and E. Shuryak, "Event-by-event fluctuations in heavy ion collisions and the QCD critical point", *Phys. Rev.* **D60** (1999) 114028.

[30] U. Heinz, "The little bang: Searching for quark-gluon matter in relativistic heavy-ion collisions", `hep-ph/0009170`.

[31] H. Satz, "Colour deconfinement in nuclear collisions", *Rept. Prog. Phys.* **63** (2000) 1511.

[32] H. Satz, "The search for the QGP: A critical appraisal", `hep-ph/0009099`.

[33] K. Rajagopal, "The phases of QCD in heavy ion collisions and compact stars", `hep-ph/0009058`.

[34] R. V. Gavai, "Chemical potential on the lattice revisited", *Phys. Rev.* **D32** (1985) 519.

[35] P. Hasenfratz and F. Karsch, "Chemical potential on the lattice", *Phys. Lett.* **B125** (1983) 308.

[36] J. B. Kogut, M. A. Stephanov, D. Toublan, J. J. M. Verbaarschot, and A. Zhitnitsky, "QCD-like theories at finite baryon density", *Nucl. Phys.* **B582** (2000) 477.

[37] I. Barbour *et al.*, "Problems with finite density simulations of lattice QCD", *Nucl. Phys.* **B275** (1986) 296.

[38] J. B. Kogut, M. P. Lombardo, and D. K. Sinclair, "Quenched QCD at finite density", *Phys. Rev.* **D51** (1995) 1282–1291.

[39] M.-P. Lombardo, J. B. Kogut, and D. K. Sinclair, "Pathologies of quenched lattice QCD at non–zero density and its effective potential", *Phys. Rev.* **D54** (1996) 2303–2316.

[40] **UKQCD** Collaboration, I. M. Barbour, "Problems in simulating QCD at finite density on a lattice", *Nucl. Phys.* **A642** (1998) 251.

[41] M. A. Stephanov, "Random matrix model of QCD at finite density and the nature of the quenched limit", *Phys. Rev. Lett.* **76** (1996) 4472–4475.

[42] A. Gocksch, "On lattice QCD at finite density", *Phys. Rev.* **D37** (1988) 1014.

[43] D. E. Miller and K. Redlich, "Exact implementation of baryon number conservation in lattice gauge theory", *Phys. Rev.* **D35** (1987) 2524.

[44] I. M. Barbour, S. E. Morrison, E. G. Klepfish, J. B. Kogut, and M.-P. Lombardo, "Results on finite density QCD", *Nucl. Phys. Proc. Suppl.* **60A** (1998) 220.

[45] I. Bender *et al.*, "Full QCD and QED at finite temperature and chemical potential", *Nucl. Phys. Proc. Suppl.* **26** (1992) 323–325.

[46] T. C. Blum, J. E. Hetrick, and D. Toussaint, "High density QCD with static quarks", *Phys. Rev. Lett.* **76** (1996) 1019–1022.

[47] P. E. Gibbs, "The fermion propagator matrix in lattice QCD", *Phys. Lett.* **B172** (1986) 53.

[48] G. Boyd *et al.*, "Thermodynamics of SU(3) lattice gauge theory", *Nucl. Phys.* **B469** (1996) 419–444.

[49] B. Beinlich, F. Karsch, and E. Laermann, "Improved actions for QCD thermodynamics on the lattice", *Nucl. Phys.* **B462** (1996) 415–436.

[50] B. Beinlich, F. Karsch, E. Laermann, and A. Peikert, "String tension and thermodynamics with tree level and tadpole improved actions", *Eur. Phys. J.* **C6** (1999) 133.

[51] N. Attig, F. Karsch, B. Petersson, H. Satz, and M. Wolff, "Polyakov loop correlations in Landau gauge and the heavy quark potential", *Phys. Lett.* **B209** (1988) 65.

[52] E. Eichten *et al.*, "The spectrum of charmonium", *Phys. Rev. Lett.* **34** (1975) 369–372.

[53] C. Quigg and J. L. Rosner, "Quantum mechanics with applications to quarkonium", *Phys. Rept.* **56** (1979) 167–235.

[54] E. Eichten, K. Gottfried, T. Kinoshita, K. D. Lane, and T. M. Yan, "Charmonium: Comparison with experiment", *Phys. Rev.* **D21** (1980) 203.

[55] G. S. Bali, "QCD forces and heavy quark bound states", `hep-ph/0001312`.

[56] M. Lüscher, K. Symanzik, and P. Weisz, "Anomalies of the free loop wave equation in the WKB approximation", *Nucl. Phys.* **B173** (1980) 365.

[57] C. J. Morningstar, K. J. Juge, and J. Kuti, "Where is the string limit in QCDΓ", *Nucl. Phys. Proc. Suppl.* **73** (1999) 590.

[58] M. Gao, "Heavy quark potential at finite temperature from a string picture", *Phys. Rev.* **D40** (1989) 2708.

[59] P. de Forcrand, G. Schierholz, H. Schneider, and M. Teper, "The string and its tension in SU(3) lattice gauge theory: Towards definitive results", *Phys. Lett.* **B160** (1985) 137.

[60] R. D. Pisarski and O. Alvarez, "Strings at finite temperature and deconfinement", *Phys. Rev.* **D26** (1982) 3735.

[61] J. Engels and V. K. Mitryushkin, "Mass gap and finite size effects in finite temperature SU(2) lattice gauge theory", *Phys. Lett.* **B282** (1992) 415–422.

[62] S. Nadkarni, "Nonabelian debye screening. 1. the color averaged potential", *Phys. Rev.* **D33** (1986) 3738.

[63] A. K. Rebhan, "The nonabelian debye mass at next-to-leading order", *Phys. Rev.* **D48** (1993) 3967–3970.

[64] A. K. Rebhan, "Nonabelian debye screening in one loop resummed perturbation theory", *Nucl. Phys.* **B430** (1994) 319–344.

[65] C. Gale and J. Kapusta, "Modification of debye screening in gluon plasma", *Phys. Lett.* **B198** (1987) 89.

[66] G. S. Bali, "Overview from lattice QCD", *Fizika* **B8** (1999) 229.

[67] **SESAM** Collaboration, G. S. Bali *et al.*, "Static potentials and glueball masses from QCD simulations with Wilson sea quarks", *Phys. Rev.* **D62** (2000) 054503.

[68] W. Buerger, M. Faber, H. Markum, and M. Muller, "Chiral condensates and potentials for quark - multiplet sources", *Phys. Rev.* **D47** (1993) 3034.

[69] T. Banks and A. Casher, "Chiral symmetry breaking in confining theories", *Nucl. Phys.* **B169** (1980) 103.

[70] F. Karsch and E. Laermann, "Susceptibilities, the specific heat and a cumulant in two flavor QCD", *Phys. Rev.* **D50** (1994) 6954–6962.

[71] F. Karsch, E. Laermann, M. Lütgemeier, and A. Peikert, "The QCD phase transition for two and three quark flavours". In Copenhagen 1998, Strong and electroweak matter 384- 388.

[72] J. Kogut *et al.*, "Deconfinement and chiral symmetry restoration at finite temperatures in SU(2) and SU(3) gauge theories", *Phys. Rev. Lett.* **50** (1983) 393.

[73] S. Chandrasekharan and N. Christ, "Dirac spectrum, axial anomaly and the QCD chiral phase transition", *Nucl. Phys. Proc. Suppl.* **47** (1996) 527.

[74] S. Chandrasekharan and S.-Z. Huang, "Z_3 twisted chiral condensates in QCD at finite temperatures", *Phys. Rev.* **D53** (1996) 5100–5104.

[75] M. A. Stephanov, "Chiral symmetry at finite T, the phase of the Polyakov loop and the spectrum of the dirac operator", *Phys. Lett.* **B375** (1996) 249–254.

[76] P. N. Meisinger and M. C. Ogilvie, "Chiral symmetry restoration and Z_N symmetry", *Phys. Lett.* **B379** (1996) 163–168.

[77] S. Huang and B. Schreiber, "Statistical mechanics of relativistic anyon - like systems", *Nucl. Phys.* **B426** (1994) 644.

[78] B. Berg, J. Engels, E. Kehl, B. Waltl, and H. Satz, "Critical behavior in baryonic matter", *Z. Phys.* **C31** (1986) 167.

[79] G. Münster and P. Weisz, "Estimate of the relation between scale parameters and the string tension by strong coupling methods", *Phys. Lett.* **96B** (1980) 119.

[80] P. de Forcrand and V. Laliena, "The role of the Polyakov loop in finite density QCD", *Phys. Rev.* **D61** (2000) 034502.

[81] N. Cabibbo and E. Marinari, "A new method for updating SU(N) matrices in computer simulations of gauge theories", *Phys. Lett.* **B119** (1982) 387.

[82] K. Fabricius and O. Haan, "Heat bath method for the twisted Eguchi-Kawai model", *Phys. Lett.* **B143** (1984) 459.

[83] A. D. Kennedy and B. J. Pendleton, "Improved heat bath method for Monte Carlo calculations in lattice gauge theories", *Phys. Lett.* **B156** (1985) 393.

[84] S. L. Adler, "An overrelaxation method for the Monte Carlo evaluation of the partition function for multiquadratic actions", *Phys. Rev.* **D23** (1981) 2901.

[85] R. Brower, P. Rossi, and C.-I. Tan, "The external field problem for QCD", *Nucl. Phys.* **B190** (1981) 699.

[86] G. Parisi, R. Petronzio, and F. Rapuano, "A measurement of the string tension near the continuum limit", *Phys. Lett.* **B128** (1983) 418.

[87] P. D. Forcrand and C. Roiesnel, "Refined methods for measuring large distance correlations", *Phys. Lett.* **B151** (1985) 77.

[88] A. Ukawa, "QCD phase transitions at finite temperatures", *Nucl. Phys. Proc. Suppl.* **17** (1990) 118–136.

[89] G. S. Bali and K. Schilling, "Running coupling and the lambda parameter from SU(3) lattice simulations", *Phys. Rev.* **D47** (1993) 661–672.

[90] C. Bernard *et al.*, "The $N_t = 6$ equation of state for two flavor QCD", *Nucl. Phys. Proc. Suppl.* **47** (1996) 503.

[91] **MILC** Collaboration, C. Bernard *et al.*, "The equation of state for two flavor QCD at n(t) = 6", *Phys. Rev.* **D55** (1997) 6861–6869.

[92] W. Sakuler *et al.*, "Chiral symmetry and charge density in mesons for Kogut-Susskind and Wilson fermions", *Phys. Lett.* **B276** (1992) 155–162.

[93] I. T. Drummond, "Strong coupling model for string breaking on the lattice", *Phys. Lett.* **B434** (1998) 92–98.

[94] O. Philipsen and H. Wittig, "String breaking in non-abelian gauge theories with fundamental matter fields", *Phys. Rev. Lett.* **81** (1998) 4056–4059.

[95] **ALPHA** Collaboration, F. Knechtli and R. Sommer, "String breaking in SU(2) gauge theory with scalar matter fields", *Phys. Lett.* **B440** (1998) 345–352.

[96] F. Karsch and S. Stickan, "The three-dimensional, three-state Potts model in an external field", *Phys. Lett.* **B488** (2000) 319.

[97] K. Rummukainen, M. Tsypin, K. Kajantie, M. Laine, and M. Shaposhnikov, "The universality class of the electroweak theory", *Nucl. Phys.* **B532** (1998) 283.

[98] N. Wilding and A. Bruce, "Density fluctuations and field mixing in the critical fluid", *J. Phys.: Cond.Matter* **4** (1992) 3087.

[99] N. Wilding, "Simulation studies of fluid critical behavior", *cond-mat/9610133* (1996).

Hiemit erkläre ich, dass diese Arbeit von mir persönlich angefertigt wurde und nur die angegebenen Hilfsmittel verwendet wurden.

Olaf Kaczmarek